Maximilian Lasserus, Dipl. Ing Bsc

Synthesis and kinetics of core@shell and novel metal-oxide clusters: A new route for nano vanadium oxide catalysts

DOCTORAL THESIS

to achieve the university degree of

Doktor der technischen Wissenschaften

submitted to

Graz University of Technology

Supervisor

Univ.-Prof. Dipl.-Phys. Dr.rer.nat. Wolfgang E. Ernst

Co -Supervisor
Univ.-Prof. Mag.Mag. Dr.phil. Dr.techn. Andreas Hauser

Institute of Experimental Physics

Graz, März 2020

AFFIDAVIT

I declare that I have authored this thesis independently, that I have not used other than the declared sources/resources, and that I have explicitly indicated all material which has been quoted either literally or by content from the sources used. The text document uploaded to TUGRAZonline is identical to the present doctoral thesis.

Date

Signature

Abstract

A high amount of scientific effort has been devoted to unravel the properties of nanosystems and discover possible applications. In our every day life, many applications are supported by the use of nanosized systems. When approaching this size regime, various synthesis methods are used. Most are based upon chemical synthesis or sol-gel synthesis. For these kinds of synthesis routes, contamination due to solvent or surfactants can not be neglected and calcination often needs high temperatures to clean the samples.
A completely different approach is used for the creation of nano structures within this thesis. The helium nano droplet technique provides inert "nano -labs" in which the clusters are formed. Featuring an ultra low temperature, the helium droplets enable sequential doping, which makes them an ideal tool for designing desired bimetallic clusters. The growth process of the different clusters is controlled through the droplet size and the pickup conditions during the synthesis. Here, a wide range of different adjustable parameters is accessible. The most unique property of this technique is the lack of perturbation inside the droplet. The synthesis of the clusters takes place in a chemically inert environment, because no ligands or surfactants are used.
In the volume of this thesis, the helium droplet technique is used to broaden the understanding of two different material groups: core@shell nano particles and vanadium oxide nano particles. Starting with the core@shell clusters, it was possible to observe the dynamics of nanoscale diffusion for the Ag@Au system and to develop a new method of measuring it. Additionally, experiments were performed to define the diffusion barrier needed for a nanoscale Fe-cluster to not oxidise, at ambient conditions. At the end of the thesis, the synthesis and characterisation of V_2O_5 clusters were performed.

Kurzfassung

Um die Anwendungen und die Eigenschaften von Nanosystemen zu erkunden wurde in der Vergangenheit viel Forschung betrieben. In unserem alltäglichen Leben gibt es viele Dinge welche durch die Unterstützung von Nanosystemen funktionieren. Wenn man sich auf die Ebene der Nanosysteme begibt, gibt es verschiedene Synthesetechniken. Viele dieser Methoden basieren auf chemischen oder sol-gel Verfahren. Für diese Verfahren können Kontaminationen durch Lösungsmittel nicht vernachlässigt werden und das Ausbrennen dieser benötigt oft hohe Temperaturen.
Eine komplett andere Herangehensweise für die Synthese der Nanostrukturen wurde in der vorliegenden Arbeit verwendet. Die Helium Nanotropfen Technik bietet inerte "Nano-Labore" in welchen die Cluster formiert werden. Durch ihre sehr niedrige Temperatur ermöglichen die Helium Tröpfchen eine sequentielle Dotierung, was sie zu einem idealen Werkzeug für bimetallische Synthese von Nanoclustern macht. Der Wachstumsprozess der Cluster wird über die Tropfengröße und die unterschiedlichen Aufnahmewahrscheinlichkeit während der Synthese gesteuert. Hierbei sind verschiedenste Parameter einstellbar. Die wichigste Eigenschaft der Helium Tröpfchen ist aber ihre störungsfreie und chemisch inerte Umgebung in welcher die Nanostrukturen formiert werden.

In dieser Arbeit wurde die Helium-Tröpfchen-Methode verwendet um das Verständnis von zwei Materialklassen zu erweitern: core@shell Nanopartikel und Vanadiumoxid Nanopartikel. Beginnend mit den core@shell Partikeln, war es möglich die atomare Diffusion in Ag@Au Systemen zu beobachten und eine neue Methode zu entwickeln die diese beschreibt. Weitere Experimente wurden durchgeführt um die Diffusionsbarriere zu bestimmen die ein Fe- Partikel vor der Oxidation bewahrt. Am Ende dieser Arbeit wurde die Synthese und die Charakterisierung von V_2O_5 Nanopartikel durchgeführt.

Articles related to this work

(1) "Thermally induced alloying processes in a bimetallic system at the nanoscale: AgAu sub-5 nm core-shell particles studied at atomic resolution" by **Maximilian Lasserus**, Martin Schnedlitz, Daniel Knez, Roman Messner, Alexander Schiffmann, Florian Lackner, Andreas W Hauser, Ferdinand Hofer, Wolfgang E Ernst in *Nanoscale* **10**, 2017-2024 (2018).

(2) "On the passivation of iron particles at the nanoscale" by **Maximilian Lasserus**, Daniel Knez, Martin Schnedlitz, Andreas W Hauser, Ferdinand Hofer, Wolfgang E Ernst in *Nanoscale Advances* **1**(6), 2276-2283 (2019).

(3) "Vanadium (V) oxide clusters synthesized by sublimation from bulk under fully inert conditions" by **Maximilian Lasserus**, Martin Schnedlitz, Roman Messner, Florian Lackner, Wolfgang E Ernst, Andreas W Hauser in *Chemical Science* **10**, 3473-3480 (2019).

(4) "Synthesis of nanosized vanadium (V) oxide clusters below 10 nm" by **Maximilian Lasserus**, Daniel Knez, Florian Lackner, Martin Schnedlitz, Roman Messner, Daniel Schennach, Gerald Kothleitner, Ferdinand Hofer, Andreas Wolfgang Hauser, Wolfgang E Ernst in *Physical Chemistry Chemical Physics* **21**(37), 21104-21108 (2019).

(5) "Stability of core-shell nanoparticles for catalysis at elevated temperatures: Structural inversion in the Ni-Au system observed at atomic resolution" by Martin Schnedlitz, **Maximilian Lasserus**, Ralf Meyer, Daniel Knez, Ferdinand Hofer, Wolfgang E Ernst and Andreas W Hauser in *Chemistry of Materials* **30 (3)**, 1113-1120 (2018)

(6) "Spectroscopy of gold atoms and gold oligomers in helium nanodroplets" by Roman Messner, Alexander Schiffmann, Johann V Pototschnig, **Maximilian Lasserus**, Martin Schnedlitz, Florian Lackner and Wolfgang E Ernst in *The Journal of chemical physics*, **149 (2)**, 024305 (2018)

(7) "Modelling electron beam induced dynamics in metallic nanoclusters" by Daniel Knez, Martin Schnedlitz, **Maximilian Lasserus**, Alexander Schiffmann, Wolfgang E Ernst and Ferdinand Hofer in *Ultramicroscopy*, **192**, 69-79 (2018)

(8) "Ultra-thin h-BN substrates for nanoscale plasmon spectroscopy" by Alexander Schiffmann, Daniel Knez, Florian Lackner, **Maximilian Lasserus**, Roman Messner, Martin Schnedlitz, Gerald Kothleitner, Ferdinand Hofer and Wolfgang E Ernst in *Journal of Applied Physics* **125 (2)**, 023104 (2019)

(9) "Helium nanodroplet assisted synthesis of bimetallic Ag@ Au nanoparticles with tunable localized surface plasmon resonance" by Florian Lackner, Alexander Schiffmann, **Maximillian Lasserus**, Roman Messner, Martin Schnedlitz, Harald Fitzek, Peter Pölt, Daniel Knez, Gerald Kothleitner and Wolfgang E Ernst in *The European Physical Journal D* **73 (5)**, 104 (2019)

(10) "Effects of the Core Location on the Structural Stability of Ni-Au Core-Shell Nanoparticles" by Martin Schnedlitz, Ricardo Fernandez-Perea, Daniel Knez, **Maximilian Lasserus**, Alexander Schiffmann, Ferdinand Hofer, Andreas W Hauser, Maria Pilar de Lara-Castells and Wolfgang E Ernst in *The Journal of Physical Chemistry C* **123 (32)**, 20037-20043 (2019)

(11) "The impact of swift electrons on the segregation of Ni-Au nanoalloys" by Daniel Knez, Martin Schnedlitz, **Maximilian Lasserus**, Andreas W Hauser, Wolfgang E Ernst, Ferdinand Hofer and Gerald Kothleitner in *Applied Physics Letters*, **115 (12)**, 123103 (2019)

Notes: The articles (1)-(4) are reprinted as part of this work in chapters 4-7.

Contents

List of Figures

List of Tables

1 Introduction

Nanotechnology has been utilized by humankind longer than we think. In Europe for example, the use of very fine dispersed metal particles on church windows, produces strong and bright colours. The well-known rose window of the Notre Dame is a prominent example.[13] This effect stems from quantum mechanical dynamics of small metal clusters, in this case, it would be surface plasmons of the particles. A principle much more accessible for today's life is the high storage capability of computer chips. But also bio-systems are using nanotechnology for functioning: the self-cleaning of the Lotus flower is a very prominent example for nanotechnology used by nature.[14] When approaching the nanometre size regime, the classical physics can no longer be applied in all aspects therefore quantum mechanical approaches get more and more important. Theoretical physics have used different approaches to broaden the understanding of the nano world. Up to date, experiments, as a clear validation of any theoretical observation are essential.

Within this thesis, helium droplets were utilized as synthesis vessels for core@shell clusters and new vanadium oxide clusters. The usage of this technique for the creation and the deposition of newly synthesised nano structures has been proposed in 2007.[15] In the last years, the creation of structures with a few nanometres in size has been a fundamental part of the research performed at our institute. The principle underlying this technique is quite simple: the helium droplet picks up every molecule or atom it collides with. Therefore, if a sequence of pick up zones is established, several different materials can be doped into the droplet, where they agglomerate. No solvents or any other chemicals are used in the synthesis approach, thereby the produced nano particles are clean. The clusters formed by this technique are therefore especially suited for the study of diffusion on the nanoscale or catalytic experiments. This thesis shows the possibility to synthesise clusters consisting of special metal oxides. Vanadium pentoxide evaporates in a chemically unchanged form, as is also shown in this thesis. For the measurement of the catalytic properties, a chamber was assembled in which the oxidation of CO on small synthesised Au clusters was measured.

1.1 Organisation of this Thesis

This thesis is written in a commultative manner, which means that some scientific results are presented as they were published in peer-reviewed journals. The publications are separated in chapters (chapter 4-7). To elaborate on the specific work each author has performed during publication, a list at the beginning of each article is given. The Supporting Material for each paper can be found in chapter 10.
The basic concept of the synthesis of the nano particles by the use of a liquid helium beam is presented in chapter 2. In this chapter a basic overview of the dynamics behind the supersonic expansion of the helium beam will be discussed. The used experimental setups for the publication will be visualized and also explained.
Additional to the introduction of the scientific publications, the scope of this thesis was the construction and characterisation of a vacuum chamber for catalytic measurements. The the basic concepts and first results are presented in chapter 3.
The published articles during this thesis are introduced chronologically. The first article in chapter 4 covers observation of heated Ag@Au core@shell clusters. *In-situ* heating during Scanning Tunneling Electron Microscopy (STEM) measurements was used to analyse nanoscale diffusion. With this experiment it was possible to link bulk properties of the Ag/Au system to nanoscale diffusion.
In chapter 5 an article is presented, which is an extension of the first article. Here the necessary diffusion barrier for Fe-clusters was determined for which no oxidation of an iron core could be detected. As shell material, Au was used. A shell of three atomic layers of Au was determined to be necessary to passivate the Fe-core. After the first two articles, the topic of the thesis changed from nanoscale diffusion to the synthesis of vanadium oxide clusters. In chapter 6 Time-of-Flight mass spectrometry was used to analyse the evaporation of V_2O_5 powder in high vacuum. Here the molecule mass of $(V_2O_5)_2$ appeared as dominant in the mass spectra. Any fragmentation of the molecule within the helium droplets was suppressed according to our observation.
After taking the first steps to the synthesis of V_2O_5 molecules, the next step was to create clusters with much higher masses than before. The article in chapter 7 shows the synthesis results for different measurements. Here, the identification of the oxide state was possible due to combining different measurement techniques as STEM and Uv/Vis spectroscopy.
In chapter 8 a summary of the presented results is given. Here also the results of the primary catalytic measurements can be found.

1.2 Helium Droplets

Within this thesis, all nano particles are synthesised by using superfluid He droplets. Therefore, a short introduction should be given in this chapter.
He is the second most common element in the universe. The name can be translated from the old greek name for the sun:"*helios*". This element has two stable isotopes ^{3}He and ^{4}He. ^{4}He atoms make up 5 ppm in the atmosphere, in comparison ^{3}He is much rarer and only one in a million He-atoms is ^{3}He.[16] Therefore, experiments with ^{3}He are very expensive, and the presented work has been restricted to ^{4}He. Hence from this point on when writing He, the ^{4}He is deemed. Properties of He include the highest ionisation energy for any element with 24.6 eV and the lowest boiling point, at ambient pressure, of 4.2 K. When cooling down He below its boiling point, an additional phase transition at 2.17 K will appear. At this point (lambda point) He enters the superfluid phase. Within this phase, the de-Broglie wavelength of the He atoms becomes wider than the interatomic distance. Therefore, the atom's bosonic characteristic comes into play and the atoms condensate into a quantum-mechanical state, in which the atoms lose their "identity" and can be described by a macroscopic wave function. Within this state He also exhibits additional effects such as superfluidity, unlimited thermal conductivity and other phenomena.

When the helium droplets experience vacuum conditions their temperature decreases by evaporation cooling of He atoms and reach a temperature of ≈ 0.4 K. The droplets can adsorb any molecule they hit. The foreign molecule/atoms are either adsorbed at the surfaces or are immersed into the droplet.[17] The final state for each species can be determined by the Ancilotto-parameter. A typical species of elements which adsorbs on the surface of the droplets are the alkali or earth alkali elements.[18] For the experiments performed during this thesis, the droplets were sent through one to two pick up regions, in which the desired elements were present in a gaseous form. During this doping process, different size regimes can be accessed, from simple molecule uptake (see chapter 6) to the synthesis of nanometre sized nano structure (see chapter 7). When agglomerating, the molecules/atoms dissipate their respective binding energy onto the helium droplets. Due to evaporation cooling, the helium droplets keep their temperature. However, doping He droplets with foreign species leads to an interesting and unique possibility of synthesising nano structures.

During the synthesis, the desired elements are heated within an evaporation cell to achieve a sufficient vapour pressure to dope the helium droplets. When combining two of these evaporation cells, it is possible to encapsulate the first doped element with a second element. Here one of the advantages of this method comes into play, due to the very low temperature of the droplets, the first element has already clustered, when the

second pickup region is reached by the droplet. This core@shell structure for clusters enables us to observe different dynamics on the nanoscale.

1.3 Nano Particles

The properties of bulk materials differ greatly from their respective nano sized counterparts. Within this thesis, we try to bridge the gap between molecule and bulk by using a bottom-up approach to synthesise nano particles. By using the helium droplet technique, particles of just one molecule up to several thousand can be synthesized. The balance, between makro and microscopic properties is strongly size-dependent. Therefore, many strange effects can be observed at this size level. Reasons for this can be the high amount of surface atoms or quantum-mechanical effects.[19]

In the past, nano materials have been studied very intensively. Due to the special properties in optics, magnetics and catalysis; these materials hold great potential for future applications.[20–22] However, attributes on the nanoscale are also strongly dependent on possible mixing of structural changes of the materials.[23] Therefore, clusters have to be prepared with utmost care and cleanliness. On the other side, changing or enhancing the properties by mixing specific clusters is therefore also possible. Within this work, core@shell clusters have been prepared by the helium droplet technique under fully inert conditions to determine basic properties of these materials. Understanding and reproducibly mixing of these kinds of nano-"cocktails" is an aim of ongoing scientific work.

1.4 Basics of Catalysis

One of the fundamental principles of feeding seven billion people is related to the application of catalysis, but is mostly unknown. The usage of fertilizer for agricultural products is essential to gain enough harvest for feeding all people and that is were catalysis is very important. For nearly one hundred years the Haber-Bosch and the Oswald method enable to produce a huge amount of fertilizer for agricultural use. This type of application is also important for many everyday-life products. From cleaning of car exhausts to the synthesis of sugar, the applications are numerous.
In principle, there are two different types of catalysts: heterogeneous and homogeneous. While heterogeneous catalysts have a different phase than the reactants (often solid catalyst and gaseous reactants), homogeneous catalyst have the same phase (often liquid) as the reactants. The principle of catalytic activity of materials is that they lower the energetic barrier for chemical reactions. This effect can be seen in the well-known schematic Figure 1.1, where a potential curve for a chemical reaction without a catalyst is shown in blue and the potential curve with a catalyst is shown in red. The lowering of the activation energy due to the catalyst is important, because it enables and enhances chemical reactions. This lowering often takes place due to the offering of adsorption sites on which the reactants may adsorb.

Especially small structures offer interesting adsorption sites for catalytic effects. Due to the small coordination number even noble metals become catalytically active at sizes below 100 nm.[24] For the clusters produced within this thesis a new vacuum chamber was built and first experiments on noble metal clusters were performed. Here the oxidation of carbon monoxide was performed at very low pressures on Au clusters for different size regimes.

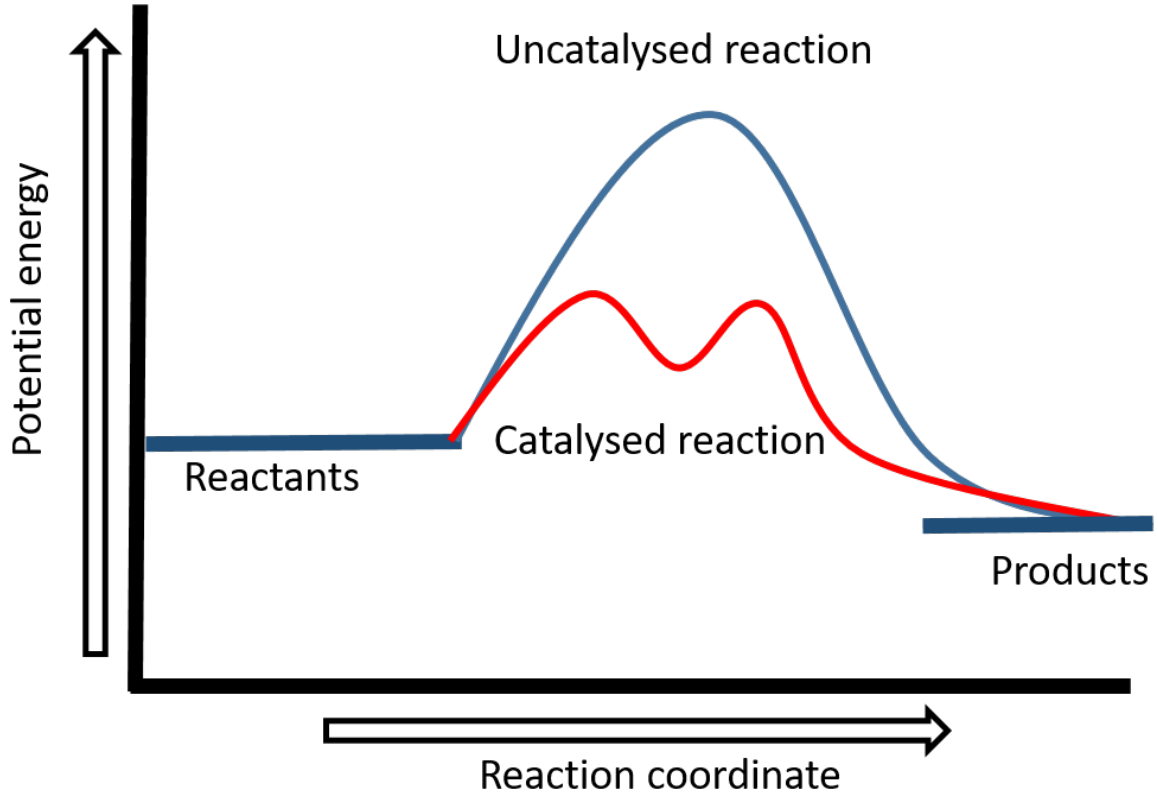

Figure 1.1: The effect of an sample chemical reaction with (red) and without of a catalyst(blue) can be seen here. The reduction of the needed energy by downsizing the potential barrier is shown.

2 Experimental Setup

Within this chapter, a fundamental overview of the performed measurement techniques, used within this thesis, should be given. Here the experimental setups are reviewed:

- Helium droplet apparatus,
- UV-vis spectrometer,
- Electron Microscope,
- separated UHV-chamber for catalytic measurements.

Each of these tools will be discussed and their characteristics will be given. During the characterisation of the nano structures in chapter 7 several different measurements techniques were performed to analyse the oxidation state.

2.1 Helium Droplet Set-up

Within this section, the apparatus for the synthesis of all nano structures, presented in this thesis, will be discussed. It should give an overview of the usage and the features of this setup, which was used for the publications (see chapter 4 - chapter 7).
In principle, three vacuum chambers with different base pressures are aligned. Starting in the first vacuum chamber, in which the He beam is created, through the pick up chamber, in which the He droplets are doped with foreign atoms/molecules, into the main chamber in which several diagnostic tools are mounted to monitor the He beam. A schematic overview of the chamber is given in Figure 2.1.

2.1.1 Theoretical Basics of Helium Droplets

For the basic characterisation of the superfluid He droplets, one has to look at the condition before and after the expansion. In the present setup, He is supersonically expanded through a small nozzle yielding an almost monochromatic beam with very narrow velocity distribution. An effusive beam, in contrast, would have the velocity distribution corresponding to the temperature of the gas reservoir (Maxwell-Bolzman distribution). In Figure 2.2 the difference in the velocity between the two beams is shown. This displayed velocity profiles were taken from reference 26. It should be

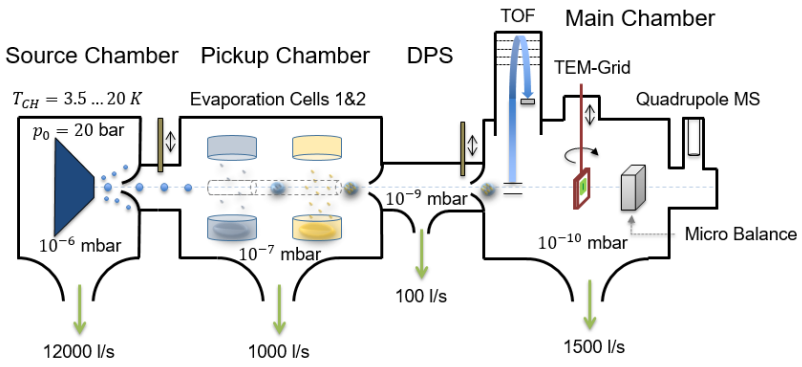

Figure 2.1: A schematic sketch of the used helium droplet machine. The setup can be divided into three chambers. In this image, the different analytic hardware is included, which will be discussed in the corresponding section. The vacuum system is described below for every chamber separately, here the effective pump volumes are displayed. This Figure was taken from 25.

noted, that the actual velocity distribution of a supersonic beam is even smaller, but that due to measurement effects the distribution is broadened. For the measurement, He with a purity of 99.9999% was used. The nozzle diameter used for the experiments presented in this thesis was 5 μm. If the ratio of the pressure from the expanding gas to the vacuum it expands into is sufficient high, the gas flow may reach sonic speed at the nozzle. For this kind of experiments typical settings for the stagnation pressure of the He are $p_0 = 20$ bar up to 60 bar and a vacuum pressure p_a of $\approx 10^{-4}$ mbar.

This process of expansion happens very fast, therefore it can be considered adiabatic. This kind of thermodynamic process gives rise to adiabatic cooling of the expanding gas. Here the internal energy of the gas is transformed to translation energy. At the start, the gas flow is continuous, but during the expansion the interaction between the He atoms increases. Therefore the He flow turns into a molecular current. After the expansion, the He current is cropped by a skimmer to obtain a laminar He flow.

In the theoretical description of the supersonic expansion one treats He as an ideal gas which is a good assumption, because it does not show any dipole moment and has a spherical shape. For ideal gases following expression can be written:

$$C_p - C_v = \mathrm{R}. \tag{2.1}$$

Here C_v and C_p are the heat capacity for constant volume and constant pressure and R is the gas constant respectively. Due to the adiabatic character of this expansion, this process is isentropic. The adiabatic exponent $\gamma = C_p/C_v$ is constant for an ideal gas, therefore the pressure and temperature before (P_1, T_1) and after (P_2, T_2) the expansion

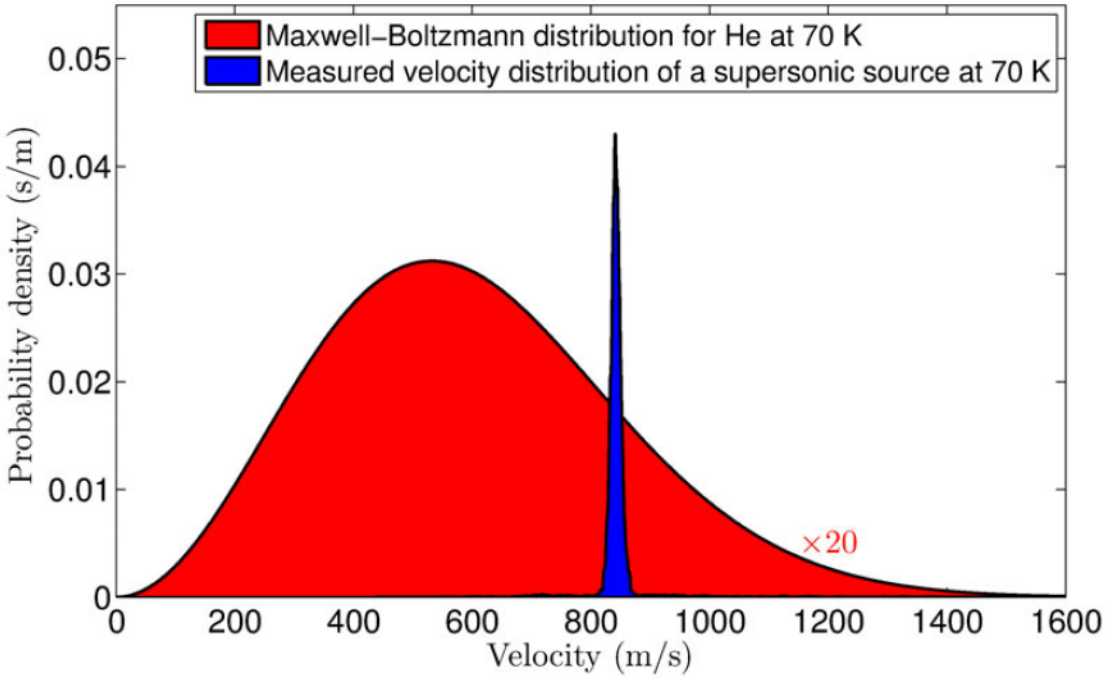

Figure 2.2: In this Figure a comparison between the velocity of He stemming from a supersonic expansion and effusive source is visible. Note that the spectra of the effusive beam was multiplied by a factor of 20 to enhance visibility and enable easy comparison. This graph was taken from 26.

are related:

$$\frac{P_2}{P_1} = \left(\frac{T_2}{T_1}\right)^{\frac{\gamma}{\gamma-1}} . \tag{2.2}$$

Using this Equation and performing some transformations one reads an expression for the velocity of the He beam:[26]

$$v \approx \sqrt{2 \cdot C_p \cdot T_0 \left(1 - \left(\frac{P_{vacuum}}{P_{nozzle}}\right)^{\frac{\gamma}{\gamma-1}}\right)}. \tag{2.3}$$

Due to the monoatomic character of He we can transform $C_p = \frac{5}{2}\frac{k_B}{m_{He}}$ and $\gamma = 5/3$. As previously mentioned, the pressure within the vacuum chamber is $\approx 10^{-4}$ mbar and the pressure at the nozzle is of minimum 20 bar so $\frac{P_{vacuum}}{P_{nozzle}}$ is $<< 1$ therefore 2.3 can be further simplified to:

$$v \approx \sqrt{\frac{5 \cdot k_B \cdot T_0}{m_{He}}} \tag{2.4}$$

This is the maximal velocity within the He beam. We can therefore now estimate the velocity of the He beam within the vacuum chamber. For the most experiments the temperature of the He beam was adjusted within a range of 5.4 K to 16 K.

2.1.2 Source Chamber

We start with the chamber in which the He droplets are created, the source chamber. Here a temperature of only a few Kelvin is used to gain small He droplets. The machine we use for this purpose is a Sumitomo RDK-408D2 cold head. The cooling takes place with two different cooling levels. The He is forced through a 5μm nozzle made out of platin and iridium alloy. These nozzles have a diameter of 2 mm and are 0.6 mm thick and were purchased at Günther Frey Gmbh. The He is pushed through the nozzle at the stagnation pressure p_{nz} with approximately 20 bar. This nozzle plate is held to the second cooling stage of the cold head. The whole apparatus is surrounded by cooling shields made of copper and an additional foil to enable sufficient cooling. After the nozzle, the He beam is directed to a 400 μm skimmer. This conically formed metal cylinder is used to crop the beam to achieve a very collimated He current. The whole apparatus is several meters long, therefore to align the He beam is always difficult. For the aiming of the He current, three screws are mounted on top of the cold head. With this three-pod simple alignments are possible. When adjusting the He beam through the chamber, one can always look at the pressure gauges. If the pressure rises spontaneously there is a high chance, that the He current is terminated within this chamber.
During the measurements, the whole chamber has to maintain high vacuum conditions. Due to the continuous flow of He, this requires special vacuum pumps with high pumping volume, otherwise the pressure would be insufficient. In our case, we use an oil diffusion pump with a pumping volume of 12000 $\frac{l}{s}$. With this pump a maximal pressure of 10^{-4} mbar is reached during the measurements.
Using an oil diffusion pump also has a downside, due to the character of the pump small oil droplets can clog the nozzle. To minimize the chance of this, a continuous flow of He is applied to the nozzle at all times. After passing the source chamber the droplet beam enters the pick-up chamber.

2.1.3 Pickup Chamber

Within this chamber, the evaporation of the desired material takes place, which is used to dope the He droplets.[27] The He droplet fly through this chamber passing two pick-up regions. Here the desired material is located within a heating basket. For the experiments presented, two different heating baskets were used, both were heated by applying a current which was provided by an external power source. The types were:

- For metals: Ted Pella Style 6, Alumina Coated Tungsten Wire Baskets, ID 0.900", 768 Watts, were used. Here a tungsten wire is coated with aluminium oxide forming a small crucible. Temperatures of $\approx$ 2000 K can be achieved.

- For vanadium oxide: Kurt Lesker EVC2Q crucibles were used. This type of crucible

is made of silicon oxide and placed within a tungsten wire basket. With this combination, temperatures of up to 1200 K can be achieved.

Within this thesis, it was the first time for us to evaporate V_2O_5. Therefore we had to test different ovens. For all experiments in the past, using higher temperatures the Ted Pella evaporation cell was sufficient. When using this evaporation cell for the V_2O_5 powder, no signal of vanadium could be detected, and when opening the chamber, it seemed like the vanadium oxide was spilt around the heating basket. The second type of evaporation cells was successfully used to analyse the vanadium oxide. To protect the vacuum chamber from too high temperature of the heating cells, water-cooled shields made of copper surround the heating baskets.
Over the crucibles a region with a significantly higher partial pressure of the desired material is formed, through which the He beam is guided. The particles are picked up by the He droplets. The foreign particles get adsorbed by the droplet and due to the temperature of the He droplets of 0.37 K, agglomerate to structures within nanometre size.[28] By varying the temperature of the crucibles, one also varies the numbers of evaporated molecules/atoms. So the amount of molecules picked up by the He droplet can be varied. In this way, different size regimes can be accessed.
During dotation of the He droplets the foreign particles would hit the droplets with an angle of 90°. Although the droplets have a higher mass, the momentum transfer is sufficient to alter the direction of the droplets, so that the He beam is terminated inside the pickup chamber. To prevent this one-sided momentum transfer, a second crucible is mounted on top the first one (leaving approximately one cm space in between), therefore the foreign atoms get reflected on the top crucible and the direction of the droplet is therefore not altered. Both crucibles are parallel connected to the external current, so that both have the same temperature.
The vacuum system used for this chamber consists of one turbo molecular pump (TMP) with a rotary vane fore pump. During the experiments a pressure of $\approx 5 \cdot 10^{-7}$ mbar is measured in this chamber. When the He droplets pass the pick up chamber they go through an additional skimmer with a 2 mm aperture at the end.

2.1.4 Differential Pumping Stage

Between the pickup chamber and the main chamber an additional chamber is mounted in which optical measurements can be performed. For the experiments presented in this thesis, this chamber only served as differential pumping stage. The pressure in this chamber is in the range of 10^{-8} mbar during measurements.

2.1.5 Main Chamber

The last chamber of the setup served for most of the characterisation of the He beam. The pressure within the main chamber is $\approx 5 \cdot 10^{-10}$ mbar. It is very important to achieve pressures this low, because otherwise, measurements like mass spectroscopy would be very inefficient. During mass deposition with the He beam the pressure rises up to $\approx 1 \cdot 10^{-8}$ mbar. For the incoming He droplets the first measurement possible is the Time-of-Flight mass spectrometer.

Time-of-Flight Mass Spectrometer

For the measurements presented in chapter 6 we used a Time-of-Flight mass spectrometer RFT50 with electron impact ionisation, a post acceleration of 20 kV and a reflectron. An overview of this tool should be given in this chapter. As the name clearly states, the mass of the ions is measured by the time of their flight through a tube to hit a multi channel plate (the detector). For the ionisation, electrons from a heated filament are used. The electrons are accelerated by a known potential U_{tof}, which defines the energy the electrons have at impact. In principle, when the electron hits an atom/molecule whose ionisations energy is below U_{tof}, it will ionise the atom. This atom is therefore positively charged. To enhance the probability of an ionisation event, magnets are used to force the electron onto a spiral trajectory. Due to this elongation of the electron path, the density of ions is higher. After the ionisation event, the ion is extracted into the flight tube. For which is achieved by two electrodes, an extractor and a repeller. The repeller is positively charged and the extractor is negatively charged. When now assuming, that every ion has one positive charge, each particle gains the same kinetic energy, because of the used electric field. Now the ions can have different masses, therefore the velocity also is different. This results in different times for each mass in the flight tube until the detector is hit.[29]
Within the He droplet the ionisation of the submerged dopant mostly happens due to charge transfer from an ionized He atom. During this process the electron hole jumps to He atoms close by.[30] For big He droplets, this dynamic can be described by a random walk. For smaller droplets, the movement of the hole can not be described as a random walk anymore, because the direction is pointed towards the dopant. This orientation stems from long range induced dipole interaction.[30] An additional ionisation process within the He droplet also can be Penning ionisation. An electronically excited He atom can be formed by inelastic collision with an electron. The electron energy has to be above 19.82 eV.[31] Electronically excited He atom now can interact with the dopant due to Penning ionisation,

$$He^* + D \rightarrow He + D^{+(*)} + e^-. \tag{2.5}$$

In Equation 2.5 the process of Penning ionisation of an arbitrary molecule is shown, which leads to the formation of an ion inside the He droplet. One could argue, that this only happens if the dopant ionisation energy is below the excitation energy of He, but this is universally applicable, because there is no known molecule for which it would not be sufficient.[31] Important to mention is, that also double ionisations of the dopant may occur, when the excitation energy of He is higher than the second ionisation energy.[32] Hence, it is possible to see double ionised masses within the TOF spectra and one has to be careful when analysing them. The detector used was a 3 stage Multi Channel Plate (MCP). In principle, this kind of detector consists of an array of small parallel adjusted electron multipliers. The amplification of these devices is in the range of 10^4 to 10^7.[33] Important for the measurement is that all ions hitting the detector are measured. To improve the signal of incoming ions, the MCP is slightly tilted to the flight path of the ions.

Quadrupole Mass Spectrometer

Within the main chamber, a Quadrupole Mass Spectrometer (QMS) is mounted for several reasons. One reason is to analyse the residual gas inside the chamber and look for leaks. In our case, the QMS has an additional task to fulfil. It is mounted off beam axis, to monitor the He partial pressure inside the chamber. When doping the He droplet with foreign species, they agglomerate inside the droplet and binding energy is released. This energy is dissipated by evaporation of He atoms. Per He atom one can assume 0.62 meV (5 $cm^{-}1$) of transferred energy.[34] For the binding of two metal atoms several (e.g. for Au 3.81 eV)[35] eV of binding energy are released. This can be measured by the QMS during experiments. This parameter of attenuation of the beam is very important for experiments, because if not monitoring the He beam, one could totally "destroy" the beam by evaporating too much material, so that no He droplets would enter the main chamber. Common attenuations during cluster synthesis are in the range of 25 % to 75 %.

Quartz Crystal Microbalance

When depositing clusters on surfaces the coverage is an important parameter. We use a quartz microbalance to estimate it. With this tool it is possible to measure very small depositions. Due to the small size of the clusters also the mass depositions of these structures is very small and is in the range of 10^{-3} $\frac{\mu g}{cm^2 s}$ to 10^{-6} $\frac{\mu g}{cm^2 s}$. The working principle of these microbalances is very simple. When a piezoelectric quartz oscillates resonantly, the frequency changes due to deposited mass on the crystal. A voltage is applied with a high frequency between 4 MHz and 6 MHz to stimulate the quartz. The change of the resonance frequency due to deposited mass can be described as (Sauerbrey-

equation)[36]:

$$\Delta f \approx -\frac{2f^2}{Z}m. \tag{2.6}$$

f is the resonance frequency of the quartz, Δf is the shift in frequency, Z is a constant and m is the deposited mass. An additional parameter, for the measurement of the deposition of the He beam, is a constant temperature of the quartz crystal. Here a setup was used to keep the microbalance at a constant temperature and to inhibit temperature influence from outside.
Note, that for the deposition of the V_2O_5 always very low deposition rates were measured.

2.2 Scanning Transmission Electron Microscope Analysis

One of the most important diagnostic tools for the nano structures, has been the Scanning Transmission Electron Microscope (STEM). Especially the high resolution of the measurements was a key factor for successful analysis of the nano structures with sizes $\leq 10\,\text{nm}$.
The whole subject of STEM measurements would exceed the volume of this thesis, therefore only a small overview of principles should be given in this chapter. A very detailed overview of the principle of STEM is found in reference 37.

In principle, electrons are emitted from a cathode by heat or by field emission and are accelerated towards a system of lenses. These lenses focus the electron beam onto the specimen. In contrast to a Scanning Electron Microscope (SEM) the electrons have to penetrate through the sample to be detected on the other side. For focusing the electron beam electromagnetic lenses are used. It is possible to penetrate up to 100 nm of sample thickness. The resulting picture is then projected onto a fluorescent screen or a CCD chip. The interaction from the electron with the sample can be roughly divided into two types. The elastically scattered which are important for the creation of the picture and the inelastically scattered electrons which are used for analytic measurements. All measurements presented in this thesis were measured on a probe-corrected FEI Titan3 G2 60-300. Especially the High Angular Annular Dark Field (HAADF) recording technique was utilized. Here the material contrast is very high, so that different elements can be distinguished. Also an acceleration voltage of 300 kV was used for all experiments. Qualitative measurements were performed inside the STEM. Here a Gatan Quantum energy filter for Electron Energy Loss Spectrometry (EELS) and four-quadrant Energy Dispersive X-ray spectroscopy (EDX) detectors (FEI Super-X) supported the STEM measurements. An additional technique for *in-situ* heating was used: Small STEM grids with a tungsten heating coil purchased from DENSsolution (rid Nano-chip XT

Carbon) were used. These chips can be heated to a temperature of 1300 °C with heating ramps of $200\frac{°C}{ms}$.
With this setup atomic resolution was achieved. Especially, the lattices of the crystal forming the clusters are visible in the HAADF images. An example picture can be seen in Figure 2.3. Hence, by analysing the lattice distances also some analytic determinations can be performed regarding the clusters. Within this thesis, this technique was used to aid the determination of the vanadium oxidation state of clusters.

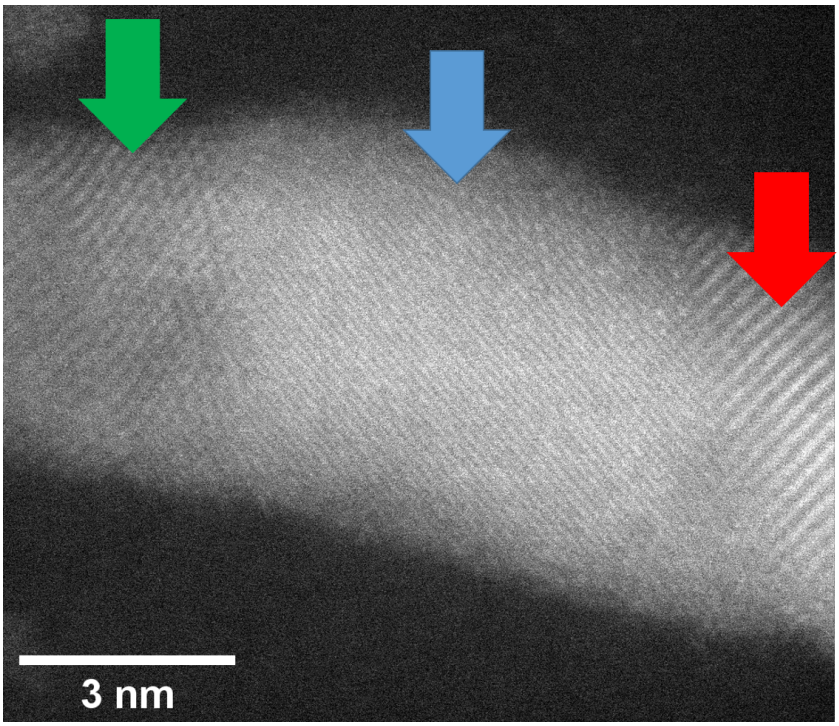

Figure 2.3: Image of an Au cluster in which the lattices are visible. Three different regions are visible: (red) a lattice distance of 0.24 nm was measured indicating the (111) surface (0.234 nm), (blue) lattice distance of 0.12 nm was measured which indicate (222) (0.117 nm) lattice and (green) a lattice distance of 0.20 nm was measured indicating the (200) (0.2035 nm) lattice.[38] Note that for the blue region also different lattices assignments would be possible. The error of this measurement is ≈ 0.01 nm.

2.3 UV Spectrometer

As another measurement method presented in this thesis UV/Vis spectroscopy was used. Therefore different nano structures were deposited onto a fused quartz plate (Corning 7980). Due to the setup of the spectrometer, a UV-1800 Shimadzu, an additional slide

was inserted as a reference to the first one. It was important that plate holding the sample clusters and the reference one were totally clean. Even the slightest dirt would destroy the measured signal. Although totally clean and from the same patch, often a rudimental offset was determined during the measurements. The measured spectra started at 190 nm and ended at 1100 nm.[39] The fused quartz has a ≈ 0 % absorbance over a wide spectral range. However, at wavelength below 300 nm the absorbance of the quartz starts, resulting in a strong shift in the absorption.[40] The results of these measurements were a fundamental part of chapter 7 because here the identification of the vanadium oxide was performed based on to the UV/Vis absorption.

2.4 UHV Chamber for Catalytic Measurements

To measure catalytic activity at low pressures a test vacuum chamber was built. The rudiment principle behind these experiments was to place synthesised nano structures inside this chamber and to introduce gas into this chamber via leak valves and see the resulting catalysed molecules. The chamber volume was designed such as to minimize interactions with the walls. As analysing tool a QMS with a secondary electron multiplier was used. An image of the chamber can be seen in Figure 2.4. The chamber is a small stainless-steel container with eight CF-40 flanges. The desired catalytic reaction was the

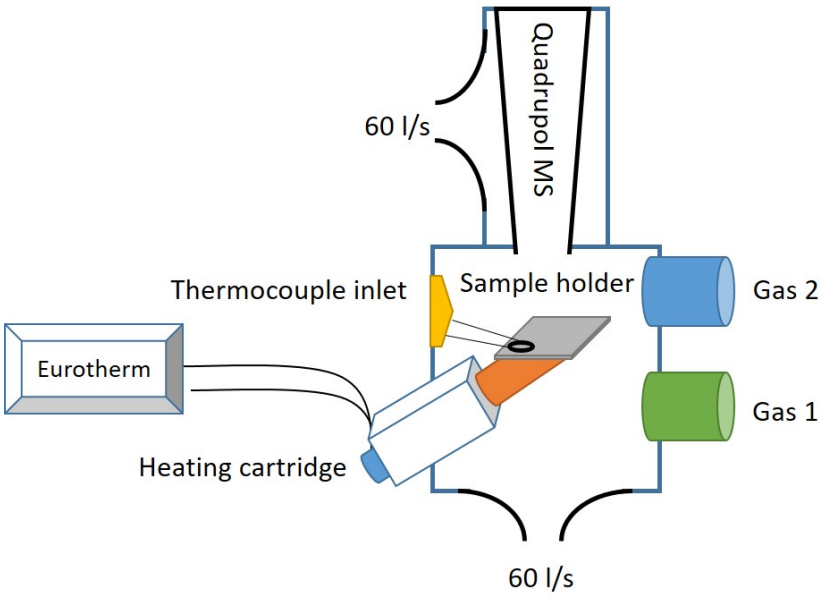

Figure 2.4: Schematic overview of the chamber built to measure catalytic activity of nano structures. Two leaking valves were used to vent small amounts of the desired gases into the chamber up to pressures of $\approx 10^{-6}$ mbar.

oxidation of carbon monoxide with oxygen to carbon dioxide:

$$2 \cdot CO + O_2 \rightarrow 2 \cdot CO_2. \tag{2.7}$$

A flange was needed for a thermoelement inlet, which was mounted onto the sample holder. Note, that the QMS was separately pumped by a turbo molecular pump. Within this chamber a pressure of $1{\cdot}10^{-9}$ was achieved after bake out. Note that, the pressure during all these procedures was measured by a Leybold ITR 90(I).
The gas inlets of the CO gas was built by using stainless steel pipes with a diameter of 6 mm. The gas was ordered at Linde with a purity of 99.9%. To ensure minimal contamination due to residual gas, the pipes used for CO were pumped to a vacuum of ≤ 1 mbar before the CO was let into these pipes. The signal in the chamber measured by the QMS indicates a sufficient purity. The same procedure was performed for the O_2 inlet, which also resulted in sufficient purity in the QMS signal of the chamber.
For controlling the temperature of the sample, a setup containing a heating cartridge was used. A small cylinder of copper was welded to the flange pointing into the vacuum. The copper had a drilling on the non-vacuum side to slide the heating cartridge in. Onto the copper cylinder a stainless steel cube was mounted on which the sample was placed. Also, a K-type thermoelement was mounted next to the sample. All copper parts were surrounded by a layer of stainless steel to inhibit any surface reaction on the copper.
For controlled heating, an Eurotherm modulator (EPC 3004) was used to operate a solid-state switch. This switch limited the time in which a power supply heated the cartridge. With this device it was possible to apply a very continuous heating ramp for the measurement.
The QMS was turned to the Multi Concentration Detection (MCD) mode. The intensity of the counts of each mass is multiplied by a calibration factor to represent the total concentration inside the vacuum. In table 2.1 the used parameters are shown. This enabled us to better analyse the composition inside the chamber, because not only each ion current for the masses, but also the composition inside the vacuum chamber, was logged.

Table 2.1: Here the factors are shown, for which the MCD measurement yields the composition of the molecules inside the vacuum. These factors were taken from the quadrupole software.[12]

	Ion Mass (amu)							
Molecule	2	12	16	18	28	32	40	44
CO	0	0	0	0	1	0	0	0
CO2	0	0.01	0.1	0	0.2	0	0	1.5
H2O	0	0	0.01	1	0	0	0	0
O2	0	0	0.1	0	0	0.8	0	0
Ar	0	0	0	0	0	0	1	0
H2	1	0	0	0	0	0	0	0

3 Preliminary Catalytic Results

The first experiments within the home-built catalytic chamber are presented here. Measurements on different Au clusters are presented. The reader should keep in mind that only a short period of time was used for the measurement, because after the first six months of building and measuring the aim of the project was changed. Nonetheless, the results of this setup will be presented in a compact way and improvements will be discussed to enhance the coming results measured with this chamber.

3.1 Measurement Procedure

Before each measurement different procedures were performed to assure the reproducibility of the measurements. The first step was to turn on the QMS and to measure a spectrum of the residual gas before the reactants were inserted into the chambers. The next step was to prepare both gases within their respective supply pipe and then slowly increase the partial pressure of both. Here a typically pressure of $2{\cdot}10^{-7}$ mbar was used for the CO and a pressure of $3{\cdot}10^{-7}$ mbar for the O_2. After adjusting both pressures by the dosing valves, a short period of time (≈ 5 min) was taken till the pressure at the pressure gauge was constant. Then the pressure gauge was turned off. Afterwards, the heating program of the sample started. Here a temperature of 350° C was used as maximum temperature. A heating ramp of 2° C per minute was chosen. The aim was to find or detect the temperature for which the samples would raise the CO_2 pressure in the chamber by transforming the CO and O_2.
During the duration of the measurement the QMS measured the partial pressure of each gas. The flow of the gases into the chamber was kept constant until the maximum temperature was achieved. On reaching this temperature, after some time, the ratio of CO to O_2 was changed and the CO_2 signal was observed. This variation was performed by changing the CO pressure from a factor of ≈ 10 $\frac{CO}{O_2}$ to a factor of ≤ 1. After this pressure variation was performed the partial pressure of the CO is regulated to the same amount as before, and the cooling is initiated. Here the power to the heating cartridge is turned off. Also for this step, partial pressures are logged.
This measurement cycle would normally be performed several times for one sample. The samples measured within this chamber were nano structures synthesized by the helium droplet technique. As support fused silica slides (SiO_2) were used, because in this first

step of catalytic measurements, a support with no strong interactions with the catalyst was desired. Also, the handling of these slides was undemanding, because there have been previous measurements performed using this kind of substrate.[41]

3.2 Results

3.2.1 Reference Empty Chamber

Within this section, a few selected experimental results will be presented and discussed. As mentioned in the previous section, the typical measurements were separated in three different regions. In Figure 3.1 one can see the measurement for the empty chamber with a clean SiO_2 chip, after bake out. The three regions marked in the Figure represent the following parts in the measurement:

1. The gas inlet is adjusted to the desired pressure and the heating is started from room temperature to 350° C. During heating, the inability of the leaking valves to provide a constant pressure is seen. Especially for the O_2 valve the signal is constantly shifting.

2. Here the sample temperature reached 350° C. After several minutes the CO pressure is varied to achieve different CO to O_2 ratios.

3. During this time span, the heating voltage was cut to zero and the sample was cooled down to room temperature. The two distinct peaks around 15:36 are the turning on of the pressure gauge.

3.2.2 Au Nanostructures

As one test the catalytic activity of different Au structures was measured. Therefore two samples were synthesized at different cold head temperatures and were deposited onto SiO_2 plates. These plates were subsequently transferred into the reaction chamber. The same measurements as seen in Figure 3.1 were performed. For a better visibility, the different region will be marked by black lines. The first presented sample was synthesized at 6 K and 60 bar stagnation pressure and a deposition time of 30 minutes was chosen. The results of this sample are shown in Figure 3.2.
The same experiment was performed with a different size regime of Au clusters. The synthesis parameters for the second patch of clusters were 8 K, 60 bar and 1 hour deposition time. The measurement was performed very similarly and the ion currents are visible in Figure 3.3.

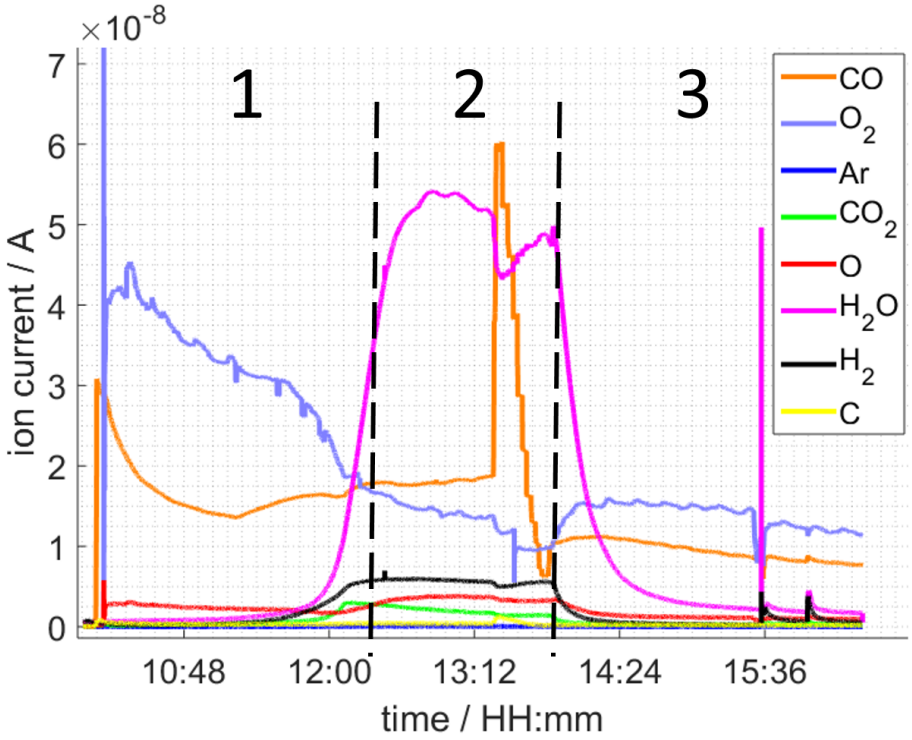

Figure 3.1: Here the measured ion currents for the different masses are shown for a cleaned chamber with a SiO_2 chip similar to the ones used for the nano structure deposition. Also, the measurement can be separated in three different sections which are discussed in the text. The legends depicts the most common molecule for the specific mass.

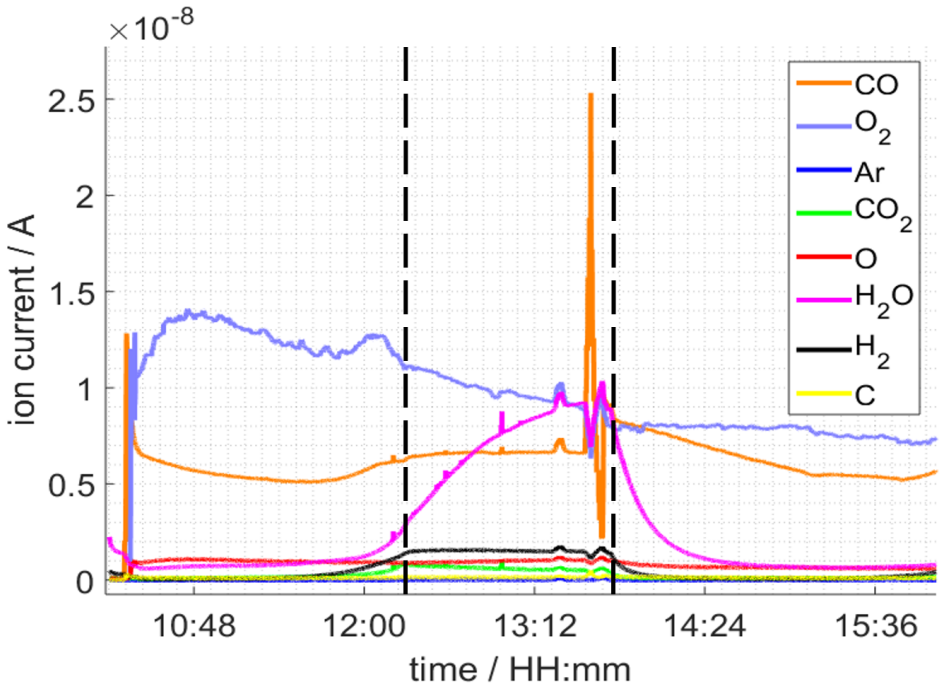

Figure 3.2: The measured ion currents for the different masses are shown for Au clusters on a SiO_2 plate. The Au clusters were synthesized at a stagnation pressure of 60 bar and 6 K cold head temperature. The legends depicts the most common molecule for the specific mass.

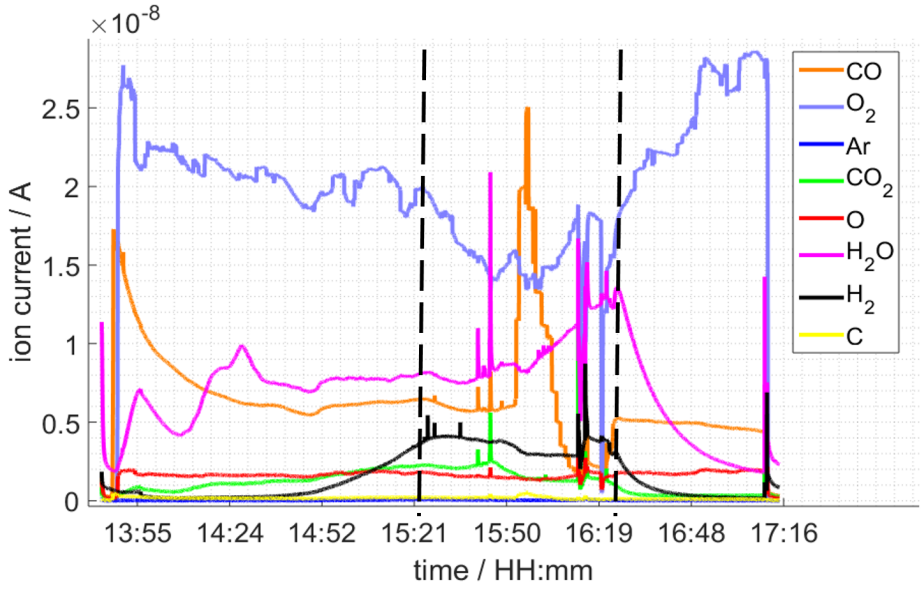

Figure 3.3: The measured ion currents for the different masses are shown for Au clusters on a SiO_2 plate. The Au clusters were synthesized at a stagnation pressure of 60 bar and 8 K cold head temperature. The legends depicts the most common molecule for the specific mass.

There have been several reports in the past that published the oxidation effect of Au clusters.[42] The temperature of many measurements was below the maximum temperature here used. But when passing the temperature suitable for the Au clusters activity one should see a change in the CO_2 signal.

3.3 Results

The results presented in the previous section will now be discussed. When comparing the results of the empty chamber and the one with a sample, plotting the CO_2 signal is essential, because if there would be any oxidation of CO it would change the slope of this signal. The reader should keep in mind that the experimental process is very similar for both measurements, therefore both results are plotted in one graph, which can be seen in Figure 3.4. Here the similarity of both measurements is clearly visible. The only small difference notable is the different behaviour of the CO_2 signal during the pressure variations on around 7000 for the sample and 7000 and 8000 for the empty chamber. Due to the similarity of the signals, it must be concluded that for measurements with this amount of deposited mass the present chamber is too insensible. Several additional measurements had been performed with similar results. Possible factors to improve future measurements may include:

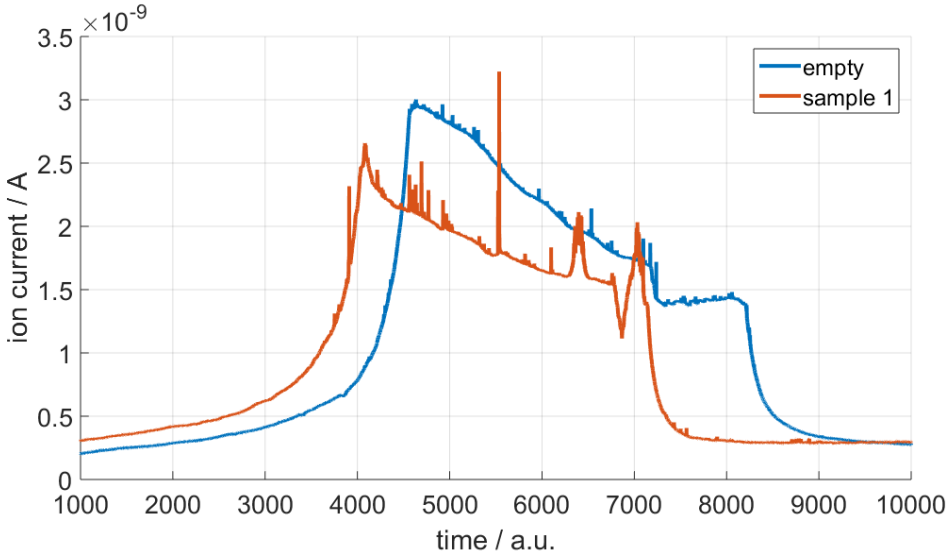

Figure 3.4: The CO_2 signal of the empty chamber, with the signal of the Au clusters (synthesized at 6 K) during one experimental cycle is plotted. To enable simple comparison the time on the x axis was turned to an arbitrary time. The legends depicts the most common molecule for the specific mass.

1. using a QMS with a better sensitivity
2. building a heating stage, with which the surrounding chamber would not be heated
3. using chemical reaction for which the resulting products are now residual vacuum gas

4 Thermally Induced Alloying Processes in a Bimetallic System at the Nanoscale: AgAu sub-5 nm core-shell Particles Studied at Atomic Resolution

The following corresponds to the publication
"Thermally induced alloying processes in a bimetallic system at the nanoscale: AgAu sub-5 nm core-shell particles studied at atomic resolution" by **Maximilian Lasserus**, Martin Schnedlitz, Daniel Knez, Roman Messner, Alexander Schiffmann, Florian Lackner, Andreas W Hauser, Ferdinand Hofer, Wolfgang E Ernst in *Nanoscale* **10** (4), 2017-2024 (2019).

This publication can be found online:
`https://pubs.rsc.org/en/content/articlehtml/2018/nr/c7nr07286d`

The author of this thesis was responsible for

- the design and execution of the experiments,
- the evaluation of the obtained electron microscopy images,
- the literature research and interpretation of the obtained data,
- and the authorship of the manuscript.

The contributions of the co-authors are listed below:

- Daniel Knez: recording of electron micrographs
- Martin Schnedlitz: assisting in creation of the theoretical principle, development of the code, manuscript editing

- Roman Messner: Fruitfull discussions of the diffusion, manuscript editing
- Alexander Schiffman: Fruitfull discussions of the diffusion, manuscript editing
- Florian Lackner: Fruitfull discussions of the diffusion, manuscript editing
- Ferdinand Hofer: supervision and funding (electron microscopy)
- Andreas W. Hauser: Assisting in creation of the theoretical principle, manuscript editing
- Wolfgang E. Ernst: supervision, manuscript editing, funding

Reprinted with permission from "Thermally induced alloying processes in a bimetallic system at the nanoscale: AgAu sub-5 nm core-shell particles studied at atomic resolution" by **Maximilian Lasserus**, Martin Schnedlitz, Daniel Knez, Roman Messner, Alexander Schiffmann, Florian Lackner, Andreas W Hauser, Ferdinand Hofer, Wolfgang E Ernst in *Nanoscale* **10** (4), 2017-2024 (2019).

Abstract

Alloying processes in nanometer-sized Ag@Au and Au@Ag core@shell particles with average radii of 2 nm are studied via high resolution Transmission Electron Microscopy (TEM) imaging on *in situ* heatable carbon substrates. The bimetallic clusters are synthesized in small droplets of superfluid helium under fully inert conditions. After deposition, they are monitored during a heating cycle to 600 K and subsequent cooling.The core-shell structure, a sharply defined feature of the TEM High-Angle Annular Dark-Field images taken at room temperature, begins to blur with increasing temperature and transforms into a fully mixed alloy around 573 K. This transition is studied at atomic resolution, giving insights into the alloying process with unprecedented precision. A new image-processing method is presented, which allows a measurement of the temperature-dependent diffusion constant at the nanoscale. The first quantification of this property for a bimetallic structure < 5 nm sheds light on the thermodynamics of finite systems and provides new input for current theoretical models derived from bulk data.

4.1 Introduction

Core@shell nanoparticles represent a class of materials with unique physical properties and various fine-tuning possibilities with respect to size, morphology and the variety of composition. Due to this extreme flexibility, a wide range of potential applications has been suggested for these materials.[20–22]

Among the elements used for nanoparticle synthesis noble metals play a major role.[43–45] The increase in occupation number of the d-orbital and the rise of cohesive energy for elements with higher atomic charge Z inside a group in the periodic table, determine silver and gold as the noblest metals within the transition metals.[46] At the nanoscale the ratio of surface to volume increases dramatically. A higher fraction of atoms at the edges and corners effectively reduces the mean coordination number and is therefore boosting the chemical reactivity.[47] Under the influence of an electric field, the electrons of these nanostructures show coherent collective oscillations known as plasmon resonances. The combination of gold and silver has highly desirable functionality with possible applications in catalysis and medicine.[48,49] Furthermore, both elements are highly resistant to oxidation under ambient conditions as well as during TEM measurements, and their

phase diagram does not show a miscibility gap. Their inertness completely removes any oxidation or contamination issues during the synthesis of the core@shell structure. This set of properties makes the AgAu system ideal for a detailed study of alloying at the nanoscale.

Theoretical approaches such as the CALPHAD (Calculation of Phase Diagrams) have been developed in the past to describe the alloying process in nanosystems.[50,51] These calculations rely entirely on assumptions based on thermodynamic data of the bulk.[52] However, in the sub 5 nm regime, the surface to volume ratio dramatically increases and quantum effects become important. Thus, nanoscopic thermodynamic properties deviate significantly from their macroscopic counterparts. Related phenomena such as diffusion and alloying are completely unexplored in this size regime. Only for larger AgAu clusters, with radii of several tens of nm, attempts have been made to measure the diffusion via laser-induced heating.[53,54]

In this article, we introduce a new approach in order to describe the alloying of nanometre-sized bimetallic particles based on thermodynamic data obtained in TEM studies, with unprecedented atomic resolution maintained during the entire heating process. The bimetallic particles are grown under fully inert conditions, and deposited on amorphous carbon substrates for TEM imaging during controlled heating. We show how the diffusion constant can be extracted from TEM images and used to quantify the alloying progress as a function of temperature and time.

For the nanoparticle synthesis we exploit superfluid He nanodroplets (He_N) as nanolabs for the production of mixed-metallic structures in the nanometre range. The dotation of He_N with particles is well established in spectroscopy,[55–57] and has recently been adapted for the controlled production and structure preserving soft deposition of metal clusters.[27,58–66]

Within this method, a beam of He nanodroplets, created via a supersonic, adiabatic expansion of pressurized helium through a cooled nozzle, collects metal atoms from vapor when passing a series of pickup zones. Due to the extremely low droplet temperature of 0.37 K[28] the metal atoms start to coagulate and form clusters inside the droplets, which act as cryostats and fully inert synthesis chambers at the same time. This offers not only the possibility of a sequential doping with different metals in any order but also allows us to study metastable structures which are not accessible with conventional techniques. The low temperature of the droplets and their ability to effectively dissipate the binding energies released during the formation of metallic bonds enables the synthesis of cluster geometries far from the global thermodynamic minimum. Another large advantage is the ability to grow clusters without any solvent- or template-induced effects. Also, typical problems of the solution-based synthesis such as large differences in the reduction potentials and a reduced miscibility at lower temperatures[67,68] are avoided.

Our article is structured as follows. Details of the experimental setup are presented in Section 6.4. In Section 4.3, we provide the theoretical background for the proposed

relation between two-dimensional scans over TEM image intensities and the diffusion constant. This quantity is then used to evaluate the alloying behaviour for the investigated systems as a function of the temperature. Section 4.4 is dedicated to an overall comparison of the observed diffusion processes in the AgAu system to predictions of Lee *et al.*,[2] who suggested a method to derive particle-size dependent phase diagrams from known values of the bulk.

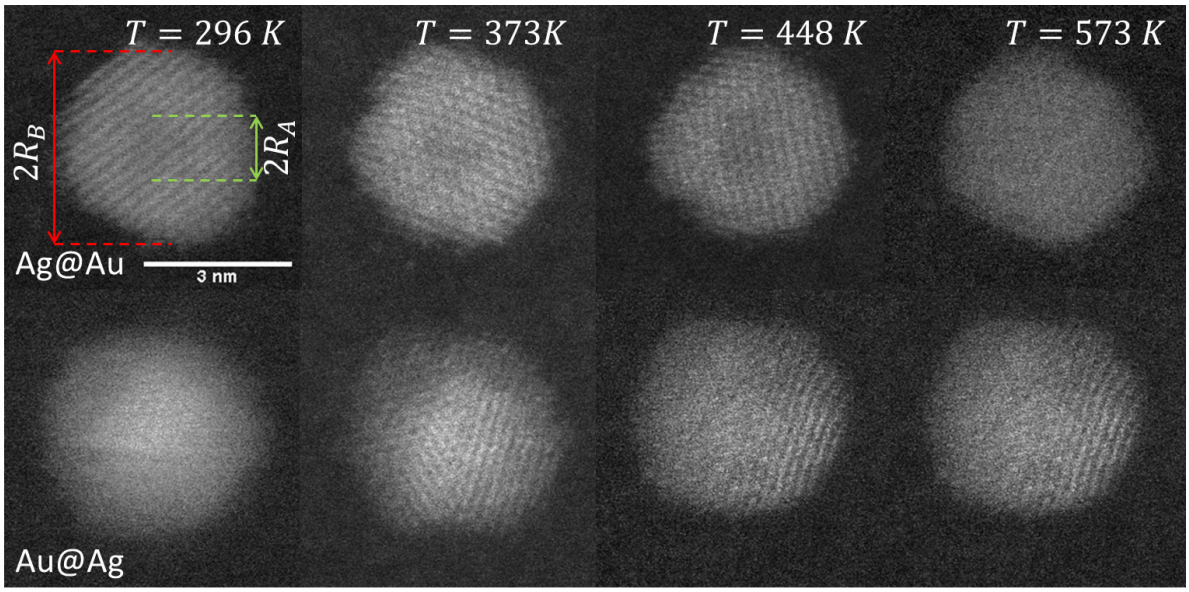

Figure 4.1: Transmission electron microscopy HAADF scans of a single Ag@Au core@shell cluster as a function of temperature (upper images) and a Au@Ag core@shell cluster scanned at the same temperatures (lower images). With increasing temperature, a softening of the contrast borders between Ag and Au is detected.

4.2 Experimental Setup

For details of the experimental setup we refer to Ref. 60. In short, He gas with a purity of 99,9999% and a constant pressure of 20 bar is expanded through a 5 μm nozzle, which is kept at temperatures below 8 K, into a vacuum of $\sim 10^{-5}$ mbar. Depending on the nozzle temperature different mean droplet sizes can be produced.[55] After croping with a 400 μm skimmer, the resulting He beam passes the pickup chamber (base pressures of $\sim 10^{-7}$ mbar). Here, the helium droplets are doped with the desired metals while crossing through two separate pickup cells. Inside these cells, the desired metal species are heated to generate enough vapour pressure for pickup. The probability for particle pickup, the mixing ratio as well as the total amount of metal in each droplet can

be controlled via separate adjustments of the individual cell temperature. Metal atoms captured by the helium droplets start to agglomerate and form cluster or wire-like structures during the flight through the vacuum chamber. Wire-like structures are created if the superfluid helium droplets exhibit quantum vortices,[69,70] a phenomenon which has been observed in the size regime beyond $3{\cdot}10^8$ helium atoms per droplet.[62] The energy which is released during metal bond formation causes a partial evaporation of helium atoms from the droplets. This is monitored by a quadrupole mass spectrometer. After pickup, the helium beam is again collimated with a 2 mm skimmer and enters the measurement chamber with a base pressure of $\sim 5 \cdot 10^{-10}$ mbar. The bimetallic clusters are deposited onto heatable TEM grids (DENSsolutions Nano-Chip XT carbon) in a soft-landing process where any remaining He is vaporized.[61,65,71]

4.2.1 Nanoparticle Synthesis

The cold He environment allows for a controlled synthesis of core@shell structures in any desired ordering via sequential doping. Depending on the original He droplet size before the pickup of metal atoms and the vapour pressure in the pickup cells it is possible to create either core@shell cluster particles or core@shell nanowires. Details of the latter procedure can be found in Refs. 72 and 73, where the phenomenon of quantum vortices was exploited to obtain enhanced one-dimensional growth. First observed in bulk superfluid helium (He II),[74–76] vortices can attract dopants which are immersed in the helium due to a pressure gradient around the vortex core,[77,78] which causes a preference for wire-like structures.[79–81]

In the current manuscript, we focus on the regime of core@shell nanoparticles produced at a nozzle temperature of 6.7 K and a pressure of 20 bar. This corresponds to an average size of $\bar{N} \sim 10^7$ helium atoms per helium droplet.[55] At these conditions, metal clusters with diameters ≤ 5 nm are produced inside the He droplets. Their shape is best described as spherical.[64] For the synthesis of nanometre-sized core@shell clusters we have chosen a helium droplet dotation ratio of 20 at.% core and 80 at.% shell material. On average, clusters with a radius of 2 nm are produced, which corresponds to approximately 2500 metal atoms per cluster.

4.2.2 Data Acquisition

After deposition on a heatable amorphous carbon TEM grid the particles are studied via a High-Angular Annular Dark-Field (HAADF) imagine detector using a FEI Titan^3 G2 60-300. A Gatan quantum energy filter attached to the microscope is employed for Electron Energy Loss Spectroscopy (EELS). Complementary, a four-quadrant Energy-Dispersive X-ray spectroscopy (EDX) detector (FEI Super-X) is utilized. The temperature of the heatable carbon grid can be varied between room temperature and 1500 K

with heating rates of up to 200 K/ms. In the presented experiments the temperature is increased from room temperature to 573 K in steps of 25 K.

4.3 Results

Our approach enables us to perform *in situ* observations of the nanoscale alloying of Au and Ag core@shell nanoparticles with atomic site resolution. Fig.4.1 shows an example of a Ag@Au (top panel) and Au@Ag (bottom panel) core@shell nanoparticle at different substrate temperatures. With the recorded HAADF intensity being proportional to Z^2 (with Z as the atomic number of the corresponding element),[82] it is easily possible to distinguish between the bright gold atoms and the darker silver atoms. With increasing temperature, the initially separated elements diffuse into each other. In particular, when comparing images taken at 448 K to those taken at 573 K, an intact core can still be seen at the former temperature but disappears completely at the latter.

4.3.1 From Density Profiles to a Diffusion Constant $D(T)$

We present a convenient technique for the extraction of the temperature-dependent diffusion constant of a given metal combination directly from HAADF observations. As described in section 5.2.1, our synthesis method allows the full encapsulation of any metallic core material A by a metal of type B or vice versa. Assuming a spherically symmetric cluster, the initial, radial density profiles $\rho_{\mathrm{A}}(r, t = 0)$ and $\rho_{\mathrm{B}}(r, t = 0)$ of the core and the shell, respectively, can be approximated by an analytical expression $d(r, R)$ built from error functions,

$$d(r, R) = \frac{1}{2}\left(\mathrm{erf}\left(\frac{r+R}{\sqrt{2}\sigma}\right) - \mathrm{erf}\left(\frac{r-R}{\sqrt{2}\sigma}\right)\right), \tag{4.1}$$

with the definitions

$$\rho_{\mathrm{A}}(r, 0) = d(r, R_{\mathrm{A}}), \tag{4.2}$$

$$\rho_{\mathrm{B}}(r, 0) = d(r, R_{\mathrm{B}}) - d(r, R_{\mathrm{A}}), \tag{4.3}$$

with R_{A} denoting the core radius and R_{B} the outer radius of the bimetallic cluster, as indicated in the upper left image of Figure 4.1. The slope of the density profile is described by the parameter σ which controls the smoothness of the density progression at the transition zone from metal A to B. These initial profiles $\rho_i(r, t)$ (for $i = \mathrm{A}, B$) are then numerically evolved in time as described by the spherical Einstein diffusion equation,[83]

$$\frac{\partial \rho_i}{\partial t} = \frac{\partial D}{\partial r}\frac{\partial \rho_i}{\partial r} + \frac{2D}{r}\frac{\partial \rho_i}{\partial r} + D\frac{\partial^2 \rho_i}{\partial r^2}, \tag{4.4}$$

with the diffusion constant D entering the equation on the right hand side. Note that our model considers metal diffusion processes of a finite spherical object, which is reflected in

the choice of setting $D = 0$ for $r > R_B$. With this assumption and the initial condition $\rho_i(r, 0)$=$\rho_{i,0}$ Equation 4.4 can be solved numerically via a finite differences approach. The choice of Gauss error functions for the initial shell density keeps the derivative of the first term on the right hand side of Equation 4.4 finite. Note that this term vanishes in the standard form of the diffusion equation for a constant D; its presence here is a consequence of the finite cluster size and prevents the system from an unphysical diffluence. The solution $\rho_i(r, t)$ is then used to obtain a simulated intensity profile of the cluster as a function of the diffusion progress. For a direct comparison to the two-dimensional, experimentally accessible observable, the radial density distribution has to be converted into an intensity profile. With the intensity being proportional to the projected density, such a profile is obtained by the integration of $\rho_i(\vec{r}, t)$, the corresponding spatial density distribution, over one cartesian coordinate, and plotting the result as a function of one of the remaining coordinates. A comparison of the simulated profiles to the angularly averaged TEM data for Ag@Au and Au@Ag clusters can be found in Figure 4.2.

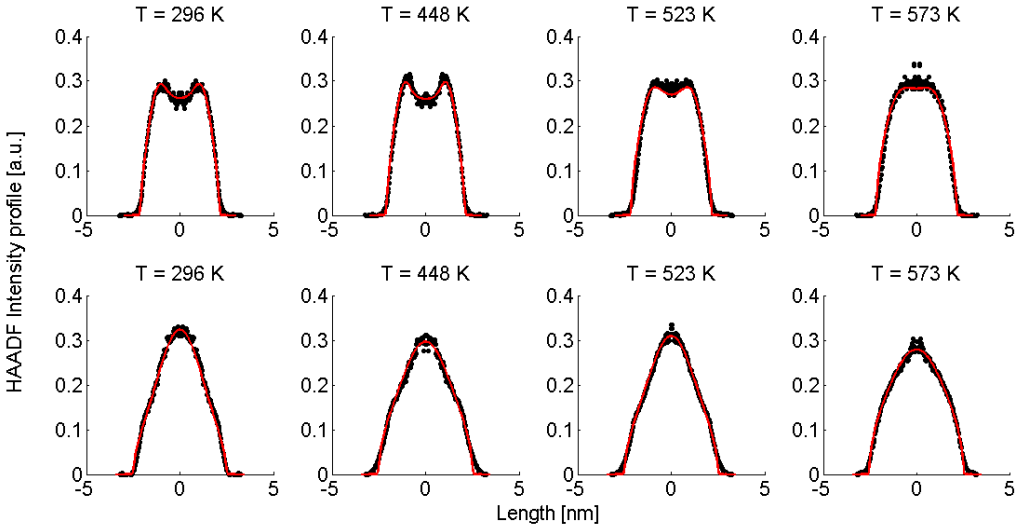

Figure 4.2: Linear HAADF intensity profiles of a Ag@Au (upper row) and Au@Ag (lower row) cluster as a function of the observation temperature. For each temperature a fit of the calculated intensity profile and the measurements is performed. Each measured, temperature-dependent intensity profile is plotted and compared to the calculated fit obtained from Equation 4.4.

Note that this figure already contains a series of comparisons for different temperatures, which is, to the knowledge of the authors, the first detailed documentation of a diffusion process over temperature in bimetallic nanoparticles with atomic resolution. It can be seen that the border between the core and shell element flattens out with increasing temperature. For Ag@Au clusters (upper panel), the initial form has a local

intensity minimum in the centre of the cluster and a maximum at the radius of the core. This is due to the projection of a sphere when performing two-dimensional scans, with the intensity profile being obtained by the integration over elements in z-direction. In the case of Au@Ag, the intensity profile shows a global maximum in the centre, where the amount of projected Au atoms is at a maximum, and an inflection point at the core radius. The shape of the profile for the Ag@Au cluster changes significantly with temperature, but only slightly for the Au@Ag cluster, which results in larger uncertainties for the diffusion progress in the latter case. Therefore, only Ag@Au clusters are used to determine the temperature-dependent diffusion constant $D(T)$ for the Ag@Au system in the next step.

First, note that the temperature dependence enters Equation 4.4 only via the diffusion constant $D = f(T)$. Neglecting the first term on the right hand side of Equation 4.4, a mathematical necessity to keep the system size finite over time, it becomes obvious that the solution of the differential equation can be written as $\rho_i(r, D(T) \cdot t)$, a function of the radius and the product of the time-dependent diffusion constant and the time. Therefore, information for D can be derived by solving Equation 4.4 within a given time interval k between two TEM-profile measurements: Since the temperature is increased in discrete steps and kept constant between two measurements, the diffusion constant of each interval k is determined by the current temperature T_k and by the change of the density profiles between the beginning and the end of the interval. The diffusion constant for interval k is obtained via least-square fits of the time-evolved profiles to the measured, angular-averaged TEM results. From these point-wise evaluations we can determine the approximate temperature dependence of D within the experimentally accessible heating range.

4.3.2 $D(T)$ for Finite Systems

The evaluated dependence of the diffusion constant on the temperature is plotted in Figure 4.3 as determined from the HAADF images via the method discussed above. The uncertainty in these measured points is dominated by fluctuations in image contrast due to minimal changes in the electron current. Other factors such as the limited resolution and deviations of the clusters from the assumed spherical shape are comparably small. An exponential fit of the data (red dashed line) has been added to the graph, inspired by the temperature dependence which is typically observed for bulk,

$$D(T) = D_0 \exp\left(-\alpha/T\right), \tag{4.5}$$

with a literature value of $D_0 = 7.2 \cdot 10^{-6}$ m^{2}s for silver in gold[84] and α as the only fitting parameter. This approximation of the diffusion constant, which is, according to Ref. 84 also depending on the actual Ag/Au mixing ratio, is justified by the small size of the silver core, where a large fraction of Ag atoms is sitting directly at the contact surface

to the pure Au shell. We obtain a value of $\alpha = 7.325 \cdot 10^5$ K^{-1}. The fitted curve suggests the occurrence of fully mixed nanoalloys at temperatures of approximately 500 K and above. We further compare the results of our TEM-based ansatz to a theoretical model based on the extrapolation from well-known bulk parameters.[1]

Giving a brief outline of this approach to approximate the size-dependent diffusion constant $D(r)$, we start from Equation 4.5 to obtain the temperature- and size-dependent diffusion constant by writing α as $-E(r)/R$, with $E(r)$ as the thermal activation energy and R as the ideal gas constant. The thermal activation energy can be related to the melting temperature $T_m(\infty)$ of the bulk via a constant C,

$$E(\infty) = CT_m(\infty). \tag{4.6}$$

Note that the constant C depends on the material and on the type of diffusion, but not on the particle size. We further assume that any size dependence of the activation energy only enters via a dependence of the melting temperature,[85]

$$E(r) = CT_m(r), \tag{4.7}$$

with r denoting the radius of the spherical cluster. Combining Equations 4.6 and 4.7, the thermal activation energy $E(r)$ for a finite system can be expressed as

$$E(r) = \frac{T_m(r)}{T_m(\infty)} E(\infty). \tag{4.8}$$

The size-dependent diffusion coefficient can be rewritten as

$$D(r,T) = D_0 \exp\left(\frac{E(\infty)}{RT}\frac{T_m(r)}{T_m(\infty)}\right). \tag{4.9}$$

Several experimental and theoretical studies have shown that the activation energy decreases with decreasing size.[86,87] In an attempt to obtain a direct functional dependence of D on the particle size r, we employ Lindemann's empirical melting criteria to rewrite the factor $T_m(r)/T_m(\infty)$ in Equation 4.9 by a geometrically motivated expression. In this crude approximation, melting is assumed to take place if the average amplitude of thermal vibrations exceeds a critical value.[88] For the given case, the following expression can be deduced,[89]

$$\frac{T_m(r)}{T_m(\infty)} = \exp\left(\frac{-2S_{vib}(\infty)}{(3R(\frac{r}{r_0}-1))}\right), \tag{4.10}$$

with S_{vib} as the melting entropy of the bulk and r_0 as a geometry dependent factor defined as $r_0 = h(3-d)$, with $d = 0$ for spherical clusters and $h = 0.2889$ nm as the atomic diameter. Combining Equations 4.5, 4.9 and 4.10, the diffusion constant can be written as

$$D(r,T) = D_0 \exp\left(\frac{-E(\infty)}{RT}\exp\left[\frac{-2S_{vib}(\infty)}{(3R(\frac{r}{r_0}-1))}\right]\right). \tag{4.11}$$

The size-dependence of all relevant parameters in Equation 4.11 can be extracted from the literature: The melting entropy S_{vib} of nanoparticles with $r = 2\,\text{nm}$ increases approximately by 9 % in comparison to the bulk,[90] for which a reference value of S_{vib}= 9.157 $\text{J}\,\text{mol}^{-1}\,\text{K}^{-1}$) is used.[1] The size dependence of D_0, on the other hand, can be fully neglected.[87] We use a value of $D_0 = 7.2 \cdot 10^{-6}$ m^2s (Ag in Au).[84] The activation energy of the bulk is assumed to have a value of $E(\infty) = 169800$ J/mol.[1] The resulting curve is shown as blue line in Figure 4.3. Note that our ansatz is indeed capable to estimate the onset temperature for full diffusion as it is observed in the experiment. Furthermore, the slope of the curve deviates only minimally from the exponential fit (red dashed line) of the data points. Note that the model is purely based on literature values and physically motivated extrapolations thereof. The excellent match of experiment and model supports our claim to have found a useful, novel experimental technique for the exploration of metal diffusion and mixing at the nanoscale. This is nicely illustrated by a direct comparison of the activation energy $E(r)$ for the given particle size $r = 1.95$ nm derived from the fit ($-8.9573 \cdot 10^4$ J/mol) to the value obtained from the model ($-8.8098 \cdot 10^4$ J/mol), which deviates from the former by less than 2 percent.

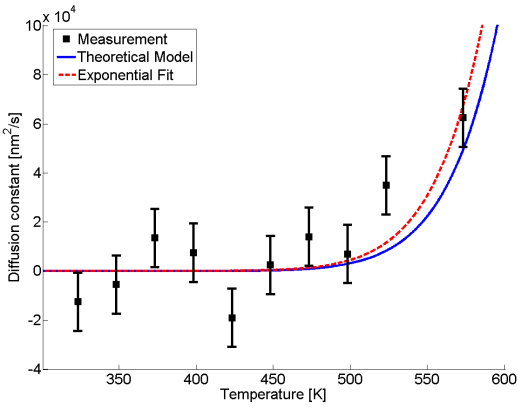

Figure 4.3: Diffusion constant as a function of temperature. Black squares are derived from HAADF measurements, the red dashed line is a fit based on Equation 4.5, the blue line is based on a revised model from Ref. 1, derived from bulk values with a mean radius of the cluster of $\bar{r} = 1.95\,\text{nm}$ and atomic binding length of $h = 0.2889\,\text{nm}$.

4.4 Phase Diagrams at the Nanoscale

In this last section we look at our experimental results in the light of ongoing discussions about the impact of particle size on fundamental qualities of bimetallic phase diagrams. The correct description and even the definition of phase transitions becomes

highly problematic at the nanoscale. This is indicated in Figure 4.4, which contains a direct comparison of selected recent measurements of our group on pure Ag and Au nanostructures,[27] the mixed-metallic AgAu cluster data of the current study, and a reference phase diagram based on a numerical model describing the impact of the particle radius on the solidus and liquidus curves of the AgAu phase diagram (see the Supporting Information for details).[2]

The graph documents the dependence of the liquid-to-solid transition on the temperature T and the relative content $X_{\mathrm{A}u}$ of gold in the binary mixture. The AgAu system forms a binary solution with unlimited solubility in both phases and shows the typical lenticular shape for the two-phase region. However, this area of phase coexistence is barely visible at the chosen temperature scale in the figure, although its average width increases slightly with decreasing particle radius.

For particles with a radius of 2.5 nm the onset of melting is predicted to occur at 400 K for pure Ag clusters and at 1000 K for pure Au clusters, with a monotonic increase of the melting temperature with increasing amount of gold. This theoretical prediction can be related to measured quantities as follows. In the case of the pure metal structures, the onset temperature of Rayleigh breakup, a well-understood process of diffusion on a metal surface driven by the minimisation of surface energy,[27,64,91] can be interpreted as a lower limit for the solidus curve since breakup becomes visible before the total melting of the structures upon heating. These results are plotted as circular data points at $X_{\mathrm{A}u}$=0 and $X_{\mathrm{A}u}$=1.[92] In the case of the mixed-metallic particles we refer to Figure 4.1 presented above, which clearly shows an ordered structure even for a temperature of 573 K where complete intermixing is observed. The corresponding data points are plotted as diamonds in Figure 4.4. These findings confirm two things: First, as stated above, alloying at the nanoscale is a temperature-driven diffusion process and clearly distinguishable from a first-order phase transition such as melting. Second, in comparison to predictions for the phase diagram in this size regime, our experimental data suggests a concave form of the solidus-liquidus curve, i.e. an increased temperature-stability of bimetallic, alloyed particles with melting temperatures which lie above that of the more stable element.

This unexpected property of the phase diagram at the nanoscale can not be derived from bulk data via the suggested scaling of model parameters with respect to particle diameter. We note that the authors of Ref. 2 give a lower limit of 5 nm for the applicability of their numerical model, but it can be extrapolated down to radii of about 2.5 nm before getting ill defined. In this size regime, a large fraction of atoms is located at the surface or at interfaces, and it is no longer possible to derive the correct behaviour from bulk data as the surface diffusion becomes the main driving mechanism for the alloying process. As a result, the 1/r extension of certain parameters in the numerical model, a core feature of this ansatz, is no longer justified and needs readjustment.

However, besides showing that current models need to be revised before application

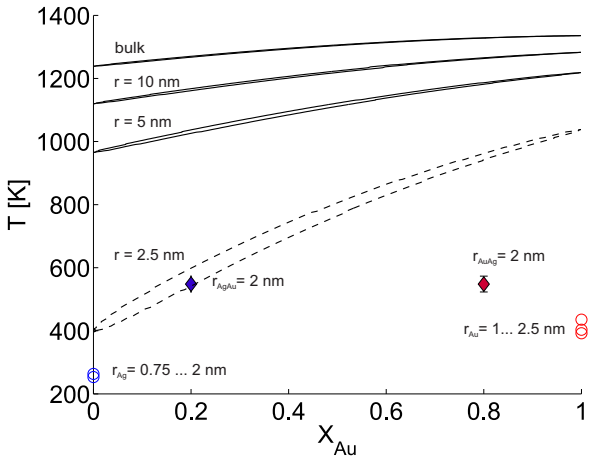

Figure 4.4: Phase diagram for the AgAu system as a function of the particle radius as suggested in Ref 2, compared to selected measurements of crucial temperatures in pure and mixed-metallic systems, see text for details.

to the studied size regime, our experimental findings also indicate new opportunities for the design of temperature-stable structures at the nanoscale.

4.5 Conclusion

In this article we reported on *in situ* nanoscale diffusion of core@shell gold and silver clusters under subsequential heating. The nature of the alloying process was studied via atomic resolution TEM imaging.

Using HAADF images we developed a method for the determination of the diffusion constant D as a function of temperature. This technique is generally applicable to any metal combination with sufficiently large differences in the atomic number of the elements involved, as HAADF contrast is proportional to Z^2. The method is based on a time evolution of the actual particle density according to Einstein's diffusion equation, and correlates the density at each step with its corresponding TEM intensity profile along radial scans of the metal particles.

We observe that the diffusion on this length scale (≤ 5 nm) is initiated at lower temperatures than in the corresponding bulk material, which is a consequence of dominant surface size effects in this regime. For both systems (Ag@Au and Au@Ag), alloying takes place between 500 and 550 K.

The results of our novel TEM-based ansatz for the derivation of $D(T)$ are compared to a theoretical model based on extrapolation of bulk parameters. We find an excellent agreement between theory and experiment in terms of absolute values as well as overall functional dependence on T, which renders our experimental technique a useful tool for

future studies of metal diffusion and alloying processes at the nanoscale. We note that the nanoparticles remain solid upon complete mixing. This shows that alloying at this size regime is a temperature-driven diffusion process and clearly distinguishable from a first-order phase transition.

A final comparison of experimental data to theoretical phase diagrams for the AgAu system at the nanoscale suggests a revision of current models. The experiment indicates a concave form of the solidus-liquidus curve, or, in other words, an increased temperature-stability of bimetallic, alloyed particles with melting temperatures above those of the pure elements at the given cluster size. This novel, unexpected feature can not be derived from known models based on a size-dependent rescaling of bulk parameters.

4.6 Acknowledgements

Maximilian Lasserus and Martin Schnedlitz thank Pascal Heim and Philipp Thaler for advice and fruitful discussions. This research has been supported by the Austrian Science Fund (FWF) under Grant No. PIR 8-N34. Further support by NAWI Graz is gratefully acknowledged. Florian Lackner acknowledges support by the Austrian Science Fund (FWF) under Grant No. J 3580-N20.

5 On the Passivation of Iron Particles at the Nanoscale

The following corresponds to the publication
"On the passivation of iron particles at the nanoscale" by **Maximilian Lasserus**, Daniel Knez, Martin Schnedlitz, Andreas W Hauser, Ferdinand Hofer, Wolfgang E Ernst in *Nanoscale Advances* **1**, 22276-2283 (2019).

This publication can be found online:
`https://pubs.rsc.org/en/content/articlehtml/2019/na/c9na00161a`

The author of this thesis was responsible for

- the design and execution of the experiments,
- the evaluation of the obtained electron microscopy images,
- the literature research and interpretation of the obtained data,
- and the authorship of the manuscript.

The contributions of the co-authors are listed below:

- Daniel Knez: recording of electron micrographs
- Martin Schnedlitz: assistance in the experiment, manuscript editing
- Andreas W. Hauser: performing and realising the theoretical calculation, manuscript editing
- Ferdinand Hofer: supervision and funding (electron microscopy)
- Wolfgang E. Ernst: supervision, manuscript editing, funding

On the passivation of iron particles at the nanoscale" by **Maximilian Lasserus**, Daniel Knez, Martin Schnedlitz, Andreas W Hauser, Ferdinand Hofer, Wolfgang E Ernst in *Nanoscale Advances* **1**, 22276-2283 (2019)

Abstract

The oxidation of Fe@Au core@shell clusters with sizes below 5 nm is studied via high resolution scanning transmission electron microscopy. The bimetallic nanoparticles are grown in superfluid helium droplets under fully inert conditions, avoiding any effect of solvents or template structures, and deposited on amorphous carbon. Oxidation resistivity is tested by exposure to oxygen at ambient conditions. The passivating effect of Au-shells is studied in detail and a critical Au shell thickness is determined which keeps the Fe core completely unharmed. Additionally, we present the first synthesis of Fe@Au@Fe-oxide onion-type structures.

5.1 Introduction

Core@shell nanoparticles represent a class of materials with unique physical properties and various fine-tuning possibilities via an adjustment with respect to size, morphology and composition. Due to this extreme flexibility, a wide range of potential applications has been suggested for these materials.[20–22,93,94] In medical sciences, nanostructures with magnetic properties have become particularly interesting for potential application in diagnosis, drug delivery, cell separation, thrombolysis and cancer treatment.[95–100] Preferred are particles below 20 nm diameter due to enhanced tissular diffusion in this size regime.[101]

Iron-based nanostructures have been studied thoroughly for applications as magnetic agents.[102,103] Qiang *et al.* could prove that iron clusters with a non-oxidized Fe core, passivated by a shell of iron oxide, have a much higher magnetic moment than fully oxidized clusters.[104] The latter type could be synthesized by exposure to oxygen during particle synthesis. Fe clusters which are exposed to oxygen after synthesis show characteristic cavities,[105] a result of Kirkendall dynamics, an effect observed for several metals:[106] Metal atoms inside the cluster are dragged towards the surface where oxidation takes place.

In this context, a passivation with a layer of gold seems reasonable in order to retain a highly magnetic core. Besides, the combination of a magnetic material and a heavy element providing a high X-ray contrast offers the opportunity to design dual agents suitable for both X-ray and MRI diagnostics. Among other passivation choices, Au stands out because of its high bio-compatibility[107], optical properties[108,109], inertness and the ability to adsorb molecules to its surface.[110] Additionally, Au nanoparticles have been

suggested as dual agents suitable for X-ray and optical detection,[111] due to their plasmonic properties.[112,113] With regards to medical applicability, combinations of Fe and Au hold a high potential for future use,[114] and several attempts have been made to synthesize various combinations of Fe and Au structures, including dumbbells[115], core@shell[116] and yolk-shell clusters.[117] For the purpose of passivation, core@shell structures are obviously most feasible. Recently, we could show that inter-metallic diffusion in core@shell nanoparticles is not only dependent on the temperature but also on the surrounding gas: the mere presence of molecular oxygen can enhance the mobility of the reactive core metal.[118]

In this article, we extend our investigation towards the passivation of the oxygen-sensitive Fe core by an additional coating with several layers of Au atoms. Helium-droplet based synthesis is particularly convenient for unbiased studies of reactivities as it provides a solvent-free and fully inert particle growth.Its underlying principle is the controlled pickup of metal atoms from vapor via a beam of superfluid helium droplets. The latter have been extensively utilized in the past as superfluid, inert and extremely cold environments for the spectroscopy of atoms, molecules and small clusters.[55,57,119] In our current setup, we perform a sequential doping with Fe followed by Au in order to synthesize mixed-metallic Fe@Au core-shell nanoparticles at fully inert conditions inside the helium droplets, fully protected from any gas phase reactions and without templates or solvents affecting their growth. The synthesis is followed by a deposition under soft landing conditions[61] onto amorphous carbon TEM grids, allowing us a controlled creation[62,120] and deposition of Fe@Au clusters with a mean diameter of $\leq 5\,\mathrm{nm}$. The clusters are first exposed to air for 120 minutes and then examined with high resolution Scanning Transmission Electron Microscopy (STEM)to evaluate their resistivity to oxidation. Since oxidation effects for nanoparticles below 10 nm at ambient conditions take place at timescales of a few minutes,[121] exposition times in the hour range are expected to enforce a full oxidation of any unprotected reactive metal. We determine a critical minimum thickness of the gold shell necessary to protect the iron core and give an explanation of our findings based on density functional theory.

5.2 Experimental Setup

For a comprehensive overview of the experimental setup we refer to Ref. 60. He gas with a purity of 99.9999 % and a pressure of 20 bar is expanded through a 5 μm nozzle which is cooled to cryogenic temperatures, resulting in the formation of a beam of helium nanodroplets. For the chosen nozzle temperature of 8 K the droplets have a mean diameter of $\approx 50\,\mathrm{nm}$.[55] After expansion and further collimation with a 400 μm skimmer the resulting He droplet beam enters the pickup chamber ($\approx 10^{-7}$ mbar). Here, the helium droplets collect Fe and Au atoms sequentially while crossing two separate

resistively-heated pickup cells. The probability for a particle pickup in each of these cells is controlled by the cell temperature, which allows us to adjust the total amount of atoms collected by the helium droplet beam as well as their mixing ratio. Atoms captured by the helium droplet beam start to agglomerate to clusters within the droplet during the flight through the vacuum chambers. The release of binding and kinetic energy of the captured atoms leads to the evaporation of helium. This attenuation of the beam is monitored by a residual gas analyzer (Balzer QMA 200/QME 200). At the end of the pickup chamber, the beam of helium droplets is again collimated by a 2 mm aperture before entering the measurement chamber with a base pressure of $\approx 5 \cdot 10^{-9}$ mbar. In this chamber, the helium droplet beam hits the TEM grid in a soft-landing process damped by the evaporation of He during impact.[61,65,71] Additional information on the surface coverage is obtained by mass deposition measurements with a microbalance.

5.2.1 Nanoparticle Synthesis

The ultracold He environment allows for a controlled synthesis of core@shell structures via sequential doping.[122] Depending on the original He droplet size before the pickup of metal atoms and the vapour pressure in the pickup cells, it is possible to create either spherical or elongated nanostructures. In the current manuscript, the parameters of 8 K nozzle temperature and 20 bar pressure are used, which corresponds to an average size of $\bar{N} \approx 10^7$ helium atoms per helium droplet.[55] For this choice of He containers, metal clusters of approximately spherical shape are produced with diameters in the nanometer range.[64] The core@shell structure arises from the sequential doping of the droplet and the coagulation of the first element before enclosure by the second element. The size of the clusters follows a log-normal distribution.[72] We choose three different doping ratios of 25 at.%, 50 at.% and 70 at.% core (Fe), corresponding to 75 at.%, 50 at.% and 30 at.% of shell material (Au). On average, clusters with diameter of 3.5 nm are produced, consisting of approximately 2500 atoms per cluster. Further information on the average thickness of the Au layer for the various doping ratios can be found in the Supporting Information, which also gives an overview of the overall distribution of particles sizes obtained in the experiment.

After deposition on an amorphous carbon TEM grid (Ted Pella 01824G), the particles remained under UHV conditions for 48 h before being removed from the chamber and left under ambient conditions for 120 minutes in order to examine the process of oxidation.

5.2.2 Data Acquisition

The particles are studied via a scanning transmission electron microscope (STEM, FEI Titan^3 G2 60-300, operating at 300 kV) using a high-angular annular dark-field (HAADF) imaging detector (Fischione Model 3000). A Gatan quantum energy filter

attached to the microscope is employed for electron energy loss spectroscopy (EELS). Complementary, a four-quadrant energy-dispersive X-ray spectroscopy (EDX) detector (FEI Super-X) is used. Note that the intensity of the elements in the HAADF images is proportional to approximately Z^2 (with Z denoting the atomic number), leading to highest intensities for the Au atoms.[82]

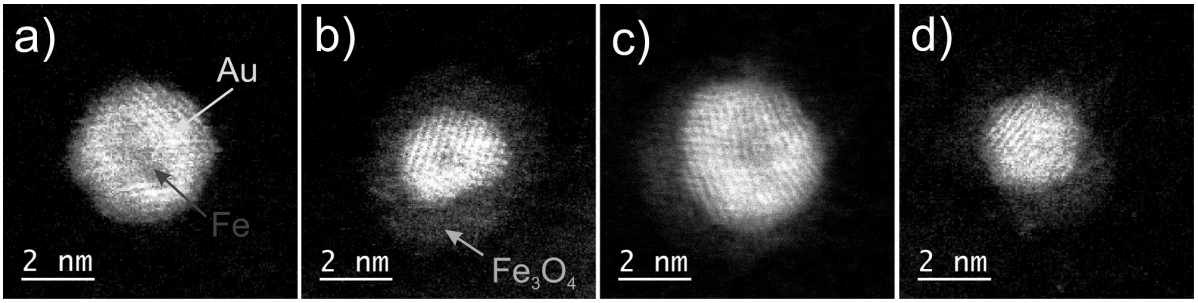

Figure 5.1: STEM HAADF images of various types of core@shell clusters. From left to right: a.)Fe@Au core@shell (fully passivated), b.) Fe@Au@Fe-oxide core@shell@shell , c.)Fe@Au with an incomplete additional shell of iron oxide, d.) Au cluster adjacent to a Fe_3O_4 cluster. The first three configurations are all related to a Fe@Au core@shell structure, see text for details. The Janus-type structure in the fourth picture is an example of incomplete coating due to a lack of Au atoms. A full passivation of the Fe-core via a Au-shell is only seen in a.).

5.3 Results

Following the synthesis described above, a variety of more or less oxidized FeAu cluster structures is obtained after exposure to air. Four different species are depicted in Figure 7.2. Their chemical structure can be clearly identified based on the contrast in the HAADF images, which is lower for metal oxides than for pure metals: Picture (a) shows a pristine Fe@Au cluster, while image (b) depicts a partially oxidized particle which is best described as an onion-like structure denoted as Fe@Au@Fe-oxide. It contains a small intact iron core, covered by a first shell with enhanced contrast, identified as Au, and a second shell of lowest contrast, corresponding to iron oxide. It can be safely assumed that the Fe must stem from the core due to the order of element pickup in the process of cluster synthesis described above. Therefore, the onion structure is a clear indication of a partial leaking of iron from the core towards the surface, despite the Au coating, which renders the encapsulation as either ineffective or incomplete in these cases. For some clusters, also the oxide shells themselves appear as not completely closed, as can be seen in picture (c) of Figure 7.2. Other particles, e.g. the cluster in

picture (d), are fully oxidized and do not show a layered structure anymore. Instead, they resemble a Janus-type configuration, a structural feature which has attracted much interest in the last decade due to its potential for applications as catalysts or biosensors.[123,124] Their occurrence is explained by the log-norm distribution of cluster sizes, which allows for situations where the amount of Au collected in the pickup process is insufficient to cover the Fe core entirely. A larger percentage of Janus particles can be enforced by a higher ratio of Fe to Au during pickup.

An interesting finding concerns the oxidation process itself and its consequence for the nanoparticle structure. Typically, when the Fe atoms diffuse to the surface, vacancies are accumulating inside the bare Fe clusters which leads to hollow structures eventually.[121] However, no evidence of such cavities is found in our TEM studies. We therefore assume that the whole Fe@Au cluster undergoes restructuring during the oxidation process. Metallic nanoparticles tend to establish a spherical shape via self-diffusion along the particle surface in order to reduce the surface energy,[64] but it is up to now uncertain why a relaxation seems to take place in the FeAu system, whereas it does not occur in pure Fe clusters where oxidation is typically described by the Kirkendall effect.[106] Since the oxide layer itself acts as a barrier for further oxidation the growth process is self-limiting. The minimum thickness for a sufficient passivation of the iron core has been measured to be 3-5 nm of iron oxide.[104]

However, most relevant in this context is the ability to prevent any oxidation at all and keep the Fe core fully intact. Apparently, the amount of Au coating has a hindering effect on the oxidation process, but the effectiveness of this additional diffusion barrier depends on the thickness of the layer. Note that incomplete oxidation of Au-coated Fe leads to onion structures of the type Fe@Au@Fe_xO_y. This suggests that it is not the diffusion of molecular oxygen through the Au layer, but the diffusion of Fe through the Au layer which enables oxidation. We therefore perform a statistical analysis of the distributions of bimetallic particles with oxidized and intact Fe cores as a function of the Au layer thickness. 52 clusters are classified as either oxidized or not by structural inspection and the thickness of their corresponding Au shell which is measured at its thinnest position visible in the TEM projection.

We note that it is likely to miss positions of minimum thickness due to the two-dimensionality which is intrinsic to a measurement in projection. Even a particle appearing as coated might have flaws which are not visible in the image. It is not possible to determine the shell thickness at the top or the bottom of a given cluster, resulting in a possible overestimation of the critical thickness. Nevertheless, every particle can be clearly characterized as having n layers of Au or less somewhere on its surface. As can be seen in Figure 5.2, there is practically not a single not-oxidized particle to be found in cases with a minimum thickness of approximately 8 Å or below. From this finding we conclude that a thickness of three layers represents the minimum for an effective passivation of the Fe core.[125] As an example, a cluster with a minimum thickness of

three Au layers in projection is shown in Figure 5.3, featuring a fully intact iron core.

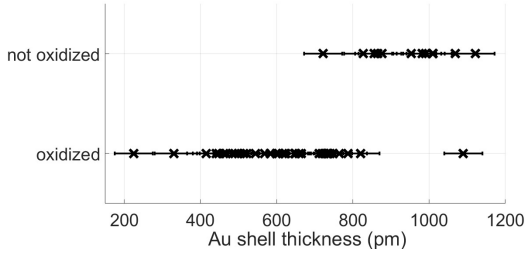

Figure 5.2: Classification results of nanoparticles as oxidized or not, plotted as a function of approximative minimum Au layer thickness.

Additional proof of the multi-layered structure is provided by a series of EELS and EDX measurements. For the sake of a direct comparison, the same type of particle as shown in the HAADF picture c.) of Figure 7.2 is chosen. Results are presented in Figure 5.4. Note the reduced EELS intensity for O around the center of the particle, which clearly suggests an iron oxide distribution in the form of a spherical shell. This supports the assumption of a non-oxidized Fe core; otherwise, the oxygen signal would show a local maximum also somewhere near the center of the particle. The barely noticeable 'halo' in the HAADF image can be identified as a mixture of Fe and O, which also confirms the assumption of an iron oxide shell (see Figures 7.2b to d).

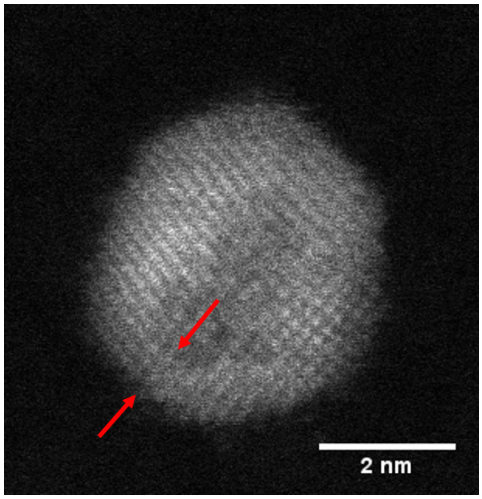

Figure 5.3: HAADF image of an Fe@Au cluster without signs of oxidation. The lattice structure of the Au-coating is clearly visible; in the lower left corner its thickness is approximately three atomic layers (marked by red arrows).

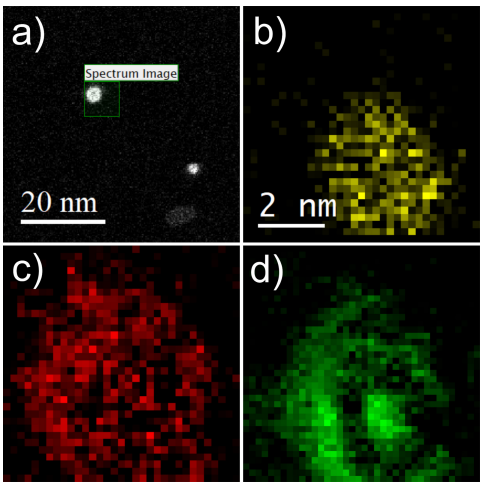

Figure 5.4: Spatially resolved EELS and EDX measurements of a three-layered system in the form of a core@shell@shell cluster. a) Overview picture, showing some clusters after deposition, indicating the region of the elemental analysis. b) EDX signal attributed to Au, c) EELS map for O, and d) the EELS map for Fe.

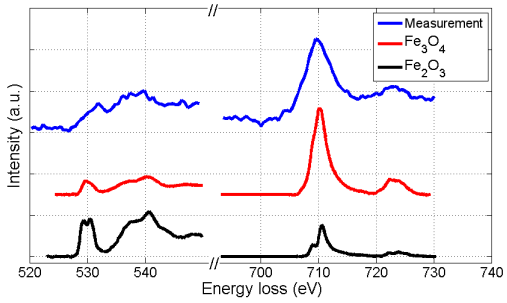

Figure 5.5: EELS spectra of the iron oxide shell of a Fe@Au@Fe_xO_y cluster after background subtraction, compared to reference EELS spectra[3,4] obtained for two different types of iron oxide. The O-K edge and the Fe-$L_{2,3}$ edge are presented. Coinciding details of the Fe-$L_{2,3}$ edge curvatures indicates that the main part of the oxide-shell is Fe_3O_4.

5.3.1 Chemical Analysis of the Oxide

We further attempt to identify the type of iron oxide present in the outmost layer after oxidation by EELS spectra analysis based on the O-K and Fe-$L_{2,3}$ binding edges. Our spectra are presented in Figure 7.1 together with two reference spectra obtained for two different types of iron oxide.[3,4] By direct comparison of the curvature, the measured spectra (blue) shows more similarity to Fe_3O_4 than Fe_2O_3. Slight deviations of the O-k edge spectra are due to the lower resolution in our measurements, which is a consequence

of the low count number. Therefore, the actual characterisation of the iron oxide is rather based on the Fe-L2,3 edge (right spectra in Figure 7.1), which allows an estimation of the oxide present. The EELS signal clearly indicates a distinct ratio of Fe_3O_4 within the oxide, but due to the possibility of signal overlapping, also a mixture of both oxides can not be excluded.

We note that Wang *et.al.* observed a similar EELS signal[126] for the O-K edge of iron oxide clusters as measured in our experiment and assigned it to Fe_3O_4, confirming the findings of Ref. 127. Studying the oxidation of small iron clusters, Peng *et.al.* also found Fe_3O_4 as the prevailing product.[128] Signorini *et.al.* show that the composition rate of Fe_2O_3 and Fe_3O_4 depends on the size and structure of the original Fe cluster before oxidation.[129] Ref. 121 reports on a preeminence of Fe_2O_3, but notes a strong dependence on the oxidation conditions. Therefore, the choice of synthesis as well as oxidation method clearly affect the final outcome. Note that the structures presented here and in Ref. 126 are studied via particle deposition, whereas Ref. 121 employs a standard synthesis method in solution. Regarding a possible impact of the TEM electron beam on the oxidation process, we consider the amount of deposited energy as too small to cause such large changes in the structure. The total dosage was kept at a minimum to avoid structural effects due to electron impact.[130,131]

We further did not observe any effects of melting upon electron beam exposure. All images provided in the manuscript show a fully intact lattice structure, from which we conclude the presence of a solid phase. Additionally, our group published several in-situ temperature transmission electron microscopy studies on comparable systems,[118,122] where lattice structures remained clearly visible even at temperatures up to 400 °C.

5.3.2 Theoretical Results

In a first attempt to study the passivating effect of Au on the Fe core via a computational approach we investigate the energy costs for the swapping of a single Fe atom with a Au atom near the interface of gold-coated bulk iron in the presence of molecular oxygen adsorbed to the bulk surface. This is done via periodic DFT calculations on a surface slab consisting of three atomic layers of iron and $n = 1, 2, 3$ layers of gold, treated with the PBE functional[132] in combination with projected-augmented-wave (PAW) pseudopotentials[133,134] as implemented in the Quantum Espresso suite of programs.[135] We note that a similar approach had been undertaken by us in a previous study on the stability of NiAu clusters in the presence of oxygen,[118] where we used at finite, icosahedral system consisting of a single Ni atom and 54 Au atoms to model smallest bimetallic clusters. In the current work, we aim for a more general discussion of the diffusion process with a better representation of the typical metallic interface of larger clusters. The supercell contains 9 metal atoms per layer. The box dimension in x and y is 8.598 Å, according to the experimental lattice constant of bcc iron. For the z or (001) direction, a length of

20 Å has been chosen to fully decouple the surface images, leaving approximately 10 Å of vacuum above after O_2 adsorption on the surface. The gold layers can be interpreted as approximately fcc-structured, with the (001) Au plane interfacing the (001) plane of Fe at an angle of 45°. Energy cutoffs (130 Ryd for the energy, 1300 Ryd for the density) and z-distances have been tested in order to provide an accuracy of 0.05 eV or 1 kcal/mol, which lies within the systematic error expected for the chosen functional. Energies are obtained via BFGS optimizations of the slab geometry after each interatomic swap. The lowest Fe layer is kept frozen to account for the bulk Fe structure. Converged slab structures consisting of 3 layers of Fe, three layers of Au and a single oxygen molecule attached to the surface are shown in Figure 5.6. The left image shows the original structure, the right one the relaxed structure after a swapping of an Fe atom with an Au atom of lowest gold layer.

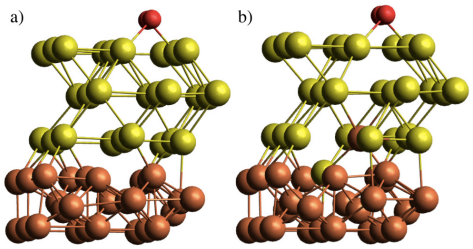

Figure 5.6: Slab models of Fe@Au core@shell clusters, comprising three layers of bcc Fe and three layers of fcc Au, with a single oxygen molecule adsorbed to the Au surface. a) pristine structure, b) structure after swapping of a single Fe and a Au atom at the interface.

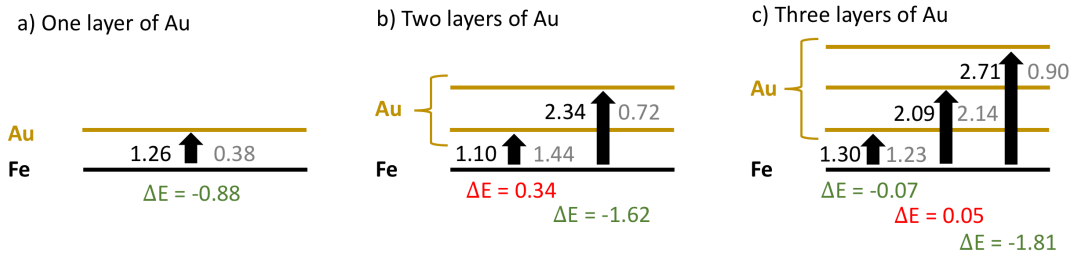

Figure 5.7: Comparison of energy costs for the swapping of a single Fe atom taken at the interface with Au atoms taken from various Au layers, calculated for gold coatings comprising a) one, b) two or c) three Au layers, in units of eV. Values obtained without oxygen are printed in black, values obtained for geometries with a single oxygen molecule attached to the corresponding surface Au layer are printed in gray. For convenience, energy differences due to oxygen presence are printed below each arrow.

The energy differences obtained for the intermediate steps of Fe migration through the Au layers by interatomic swapping are presented in Figure 5.7. In the following, we refer to the Au layer closest to the metallic interface as the first layer. The Fe atom involved in the commutation is always taken from the Fe layer closest to the interface. Energies are also compared between scenarios without (values printed in black) and with an O_2 molecule physisorbed onto the gold surface (values printed in gray).

From the sequence of black values in each scenario it is clearly visible that a swapping is less feasible the further it takes place from the Fe-Au interface. Energy costs increase from 1.26 eV in the first to 2.71 eV in the third layer. However, swapping energies for a certain layer are practically independent of the total number of surface Au layers present in the model. For example, the energy costs for a swap in the first layer are only varying between 1.10 and 1.30 eV in all three models; a variation which we consider insignificant given the estimated accuracy of the functional used. The gray values printed in Figure 5.7 reveal the impact of the oxygen molecule adsorbed to the upmost Au layer. In this case, a significant reduction of the Au/Fe swapping energy can be observed in all three models. This effect gets more pronounced with increasing layer index, producing energy differences of 0.88, 1.62 and 1.81 eV for the three models, respectively. It is also visible that a subsurface layer, if existent, is barely affected by the presence of O_2: Energies for a swapping in the first Au layer for the 2-layered system and in the second Au layer for the 3-layered system are only minimally affected. This finding is crucial for the overall interpretation of our experimental results: Since swapping in the second Au layer is less feasible by more than 1 eV, this suggests that an intact subsurface layer of Au, i.e. a layer neither at the particle surface nor at the metal interface, is acting as the most effective barrier for Fe diffusion in the models under investigation. It can be realized only if at least three layers of Au are present, which agrees well with the experimental outcome.

We note that this simple, first approach towards the diffusion behavior between the metallic interface and the particle surface is only providing a qualitative interpretation for a series of reasons. First, it assumes a direct swapping of Au and Fe atoms at main lattice sites, which is energetically less feasible than e.g. diffusion along lattice defects. Second, it is restricted to this one type of diffusion, while several mechanisms and many alternative pathways though the lattice are possible. Third, and most importantly, our argument is built on intermediate state energies, while diffusion rates can only be related to transition states between these local minima. However, the aim of this theoretical investigation is to judge the impact of the O_2 molecule on diffusion in general, and it can be expected that the presence of a subsurface layer of gold is critical as it represents a significantly high barrier for any type of Fe diffusion. Even if the actual mechanism of diffusion, most likely a complex interplay of lattice defects and possible diffusion pathways, is not yet revealed, it must involve intermediates as covered by this DFT study, and the trend of transition state energies must follow the trend of the calculated

intermediate energies.

5.4 Conclusion

Fe@Au core@shell structures, synthesized via a sequential pickup of metal atoms by liquid helium nanodroplets, are deposited on TEM grids for HAADF imaging. After exposure to ambient air for 120 minutes, structural changes of the nanoparticles due to oxidation are studied. Various types of nanostructures are observed, including unaffected core-shell nanoparticles as well as clusters showing a partial or full oxidation of the Fe core, ranging from three-layered onion structures to Janus-particles. To the knowledge of the authors, this is the first time that Fe@Au@Fe-oxide clusters have been synthesized. Spatially resolved EDX and EELS measurements have been performed to confirm their chemical composition. A statistical analysis of the observed structures shows that a critical Au shell thickness of three atomic layers of Au seems a necessary condition for effective passivation of the sensitive Fe core. Density functional theory calculations on model systems comprising one, two or three protective Au layers on top of three layers of Fe indicate that an undisturbed monolayer of Au represents the largest barrier for Fe diffusion through the Au coating, while diffusion through the interface layer (directly above the Fe layer) or the surface layer (in the presence of molecular oxygen) is much less hindered. This explains the necessity for at least three Au layers, as it is observed in the experiment.

5.5 Acknowledgements

This research has been supported by the Austrian Science Fund (FWF) under Grant PIR8-N34. The authors would like to acknowledge the use of HPC resources provided by the ZID of Graz University of Technology and by the Vienna Scientific Cluster (VSC). Further support by NAWI Graz is gratefully acknowledged. ML thanks Alexander Schiffmann for assistance during parts of the experiment and is grateful to Alexandre Gloter for helpful correspondence on EELS data.

6 Vanadium (V) Oxide Clusters Synthesized by Sublimation from Bulk under fully Inert Conditions

The following corresponds to the publication
"Vanadium (V) oxide clusters synthesized by sublimation from bulk under fully inert conditions" by **Maximilian Lasserus**, Martin Schnedlitz, Roman Messner, Florian Lackner, Wolfgang E Ernst, Andreas W Hauser, in *Chemical Science* **10**, 3473-3480 (2019).

This publication can be found online:
`https://pubs.rsc.org/en/content/articlehtml/2019/sc/c8sc05699d`

The author of this thesis was responsible for

- the design and execution of the experiments,
- the evaluation of the obtained Time-of-Flight mass spectra,
- the literature research and interpretation of the obtained data,
- and the authorship of the manuscript.

The contributions of the co-authors are listed below:

- Martin Schnedlitz: assistance in the experiment, manuscript editing
- Roman Messner:assistance in the experiment, manuscript editing
- Florian Lackner: assistance in the experiment, manuscript editing
- Wolfgang E. Ernst: supervision, manuscript editing, funding
- Andreas W. Hauser: performing and realising the theoretical calculation, manuscript editing

Reprinted with permission from "Vanadium (V) oxide clusters synthesized by sublimation from bulk under fully inert conditions" by Maximilian Lasserus, Martin Schnedlitz, Roman Messner, Florian Lackner, Wolfgang Ernst, Andreas Hauser, (2019). *Chemical science*, **10(12)**, 3473-3480. Copyright 2019,

Abstract

Oxide nanoparticles in a size range of a few nanometers are typically synthesized in solution or via laser ablation techniques, which opens numerous channels for structural change via chemical reactions or fragmentation processes. In this work, neutral vanadium oxide nanoparticles are instead synthesized by sublimation from bulk in combination with a follow-up pickup by superfluid helium droplets. Mass spectroscopy measurements clearly demonstrate the preservation of the bulk stoichiometric ratio of vanadium to oxygen in He-grown nanoparticles, indicating a tendency to tetrahedral coordination of the vanadium centers in finite geometries. This unexpected finding opens new possibilities for a combined on-the-fly synthesis of nanoparticles consisting of metal and metal-oxide layers. In comparison to mass spectra obtained via direct ionization of vanadium oxide in an effusive beam, where strong fragmentation occurred, we observe a clear preference of $(V_2O_5)_n$ oligomers with even n inside the He nanodroplets, which is further investigated and explained by electronic structure theory.

6.1 Introduction

Vanadium oxides, a prominent class of the early 3d transition metal compounds, have been objects of great interest in the last decades due to their very broad range of oxidation states. This feature, together with the comparably high abundance of vanadium, makes this group of oxides highly valuable for catalysis applications such as NO_x reduction by NH_3[136] or the oxidation of hydrocarbons,[137,138] and suggests new possibilities for the design of optical switching devices, waveguides,[136,139] and cathodes for Li-ion battery cells.[140]

This diversity of possible oxidation states also implies a large variety of geometric and electronic structures. Following the discovery of vanadium oxide nanotubes in 1998,[141,142] this particularly broad field of research has been extended by yet another facet: At the nanoscale, effects such as structural finiteness, large surface to volume ratio, and strong substrate or solvent interactions add substantially to the complexity of these materials. From the perspective of future applications, the fabrication of vanadium oxides in a nanostructured form is a highly attractive objective. Crucial for the development of such nanomaterials at an industrial level is a better understanding of the underlying formation processes, which has triggered several review articles on the

subject, focusing on techniques such as physical vapor deposition [143] or the hydrothermal treatment of aqueous solutions. [144] In general, oxide nanoparticles are typically synthesized in solution, e.g. via sol-gel techniques, microemulsions, micelle / reverse micelle methods or precipitation. [145–153] For the production of smallest clusters, laser vaporization is often the method of choice. [154] In order to allow studies in the condensed phase, the latter may be combined with a flow reactor setup. [155]

A problem common to all these approaches is the strong impact of the chosen technique on the structural outcome in the nanometer range. In the case of synthesis in solution, the nanoparticles are typically coated by ligands, which affects not only final geometries and actual properties, but also limits their usability for follow-up-treatments of other materials to some extent, in particular if high purity is desired. Laser vaporization, on the other hand, comes at the cost of undesired byproducts and often highly reactive fragments. In the case of vanadium oxide, given its high flexibility of possible oxidation states, this implies the simultaneous synthesis of a large variety of stable neutral and charged clusters with various stoichiometries. [156–167] Currently, large efforts are undertaken to understand how certain gas phase stoichiometries translate into the desired ratios in the liquid for follow-up coating processes. [155]

An alternative synthesis is presented in this article. It can be considered as an offspring of helium nanodroplet isolation spectroscopy, [55,57,119] where helium nanodroplets (He_N) have been extensively utilized as superfluid, inert containers for the spectroscopy of atoms, molecules and small clusters. Typically, this is achieved via a pickup of the target molecules by a beam of helium droplets, created in the process of a supersonic expansion of helium through a cooled nozzle. Due to the extremely low helium cluster temperature of 0.37 K [28] and the practically inert environment provided by the droplets, it is even possible to synthesize very weakly bound or highly reactive species, which can then be studied on-the-fly via optical methods such as laser-induced fluorescence or mass spectrometry. Alternatively, the structures can also be deposited on substrates for follow-up studies via electron microscopy, [27,118,168] electron energy loss spectroscopy, [169] energy-dispersive X-ray spectroscopy [170] or surface diffraction methods. [171]

In this article, we apply the helium droplet technique to the problematic but highly interesting case of vanadium oxide. We will show that a pickup of pure, neutral vanadium(V) oxide particles from vapour over the heated bulk material is possible, and demonstrate that a follow-up ionization of these particles inside the He droplets is less destructive than direct ionization in an effusive beam. This is highly advantageous, as it allows us to distinguish fragments, undesired byproducts of the ionization process, from the actual particle distribution of vanadium oxide vapour over heated bulk, and helps to clarify previous discussions on stability and abundance of certain oligomers. The correct stoichiometry for all oligomers $(V_2O_5)_n$ for n up to 25 is confirmed via time-of-flight (TOF) mass spectra, which is a particularly important result for ongoing research on the synthesis of mixed-metallic core-shell nanoparticles with the same technique, [66,118,122]

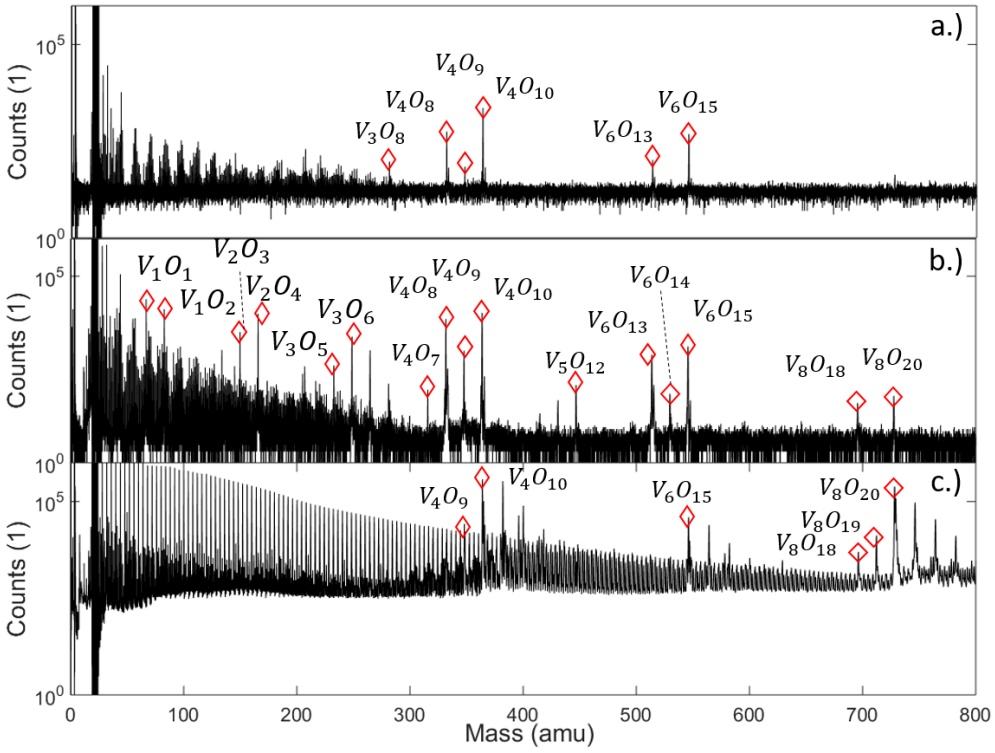

Figure 6.1: Mass spectra of vanadium oxide sublimating from V_2O_5 powder, ionized at various conditions: a) effusive source, direct ionization via electron impact with 20 eV, b) effusive source, direct ionization via electron impact with 89 eV, and c) via helium droplet beam (stagnation pressure 20 bar, nozzle temperature 9.2 K), indirect ionization of the He-immersed particles at 89 eV. Destructive effects of the electron beam at higher voltage are clearly visible (b), leading to numerous fragments scattered around the peaks of the $(V_2O_5)_n$ series, while the helium-droplet-mediated ionization (c) appears to be the least invasive method of detection. The latter also shows a regular sequence with a spacing of 4 amu in the left half of the spectrum due to the He_N cluster fragmentation, and adsorption peaks of H_2O are visible after each peak of the $(V_2O_5)_n$ series. Note the lack of a pronounced peak at the mass of V_2O_5 in all spectra. A full description of the spectra with labels for all peaks can be found in Figure S3 of the ESI.

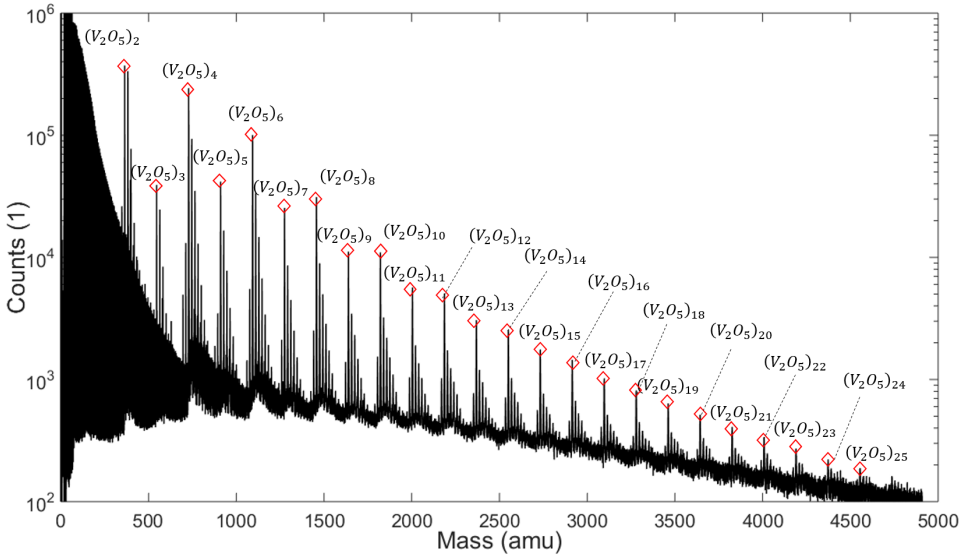

Figure 6.2: Mass spectra measured at a stagnation pressure of 20 bar and a nozzle temperature of 9.2 K. Peaks assigned to $(V_2O_5)_n$ oligomers are marked by red diamonds. Additional peaks appear due to adsorption of water molecules. An oscillation between even and odd n is visible.

as it opens the possibility of an additional coating with metal-oxide catalysts in future experiments.

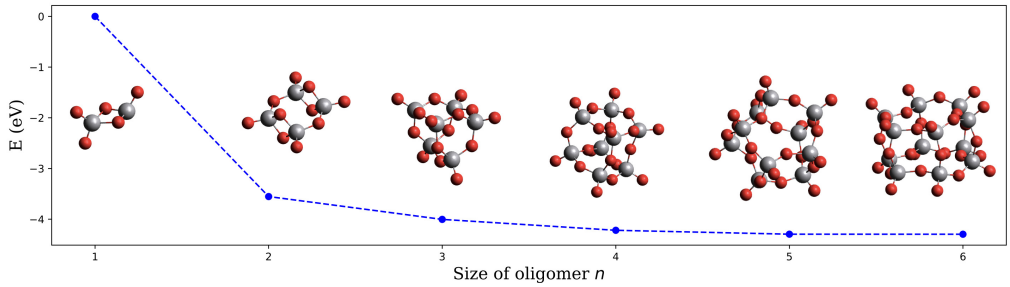

Figure 6.3: Electronic energy of the neutral $(V_2O_5)_n$ clusters per building unit, plotted as a function of the oligomer size n.

6.2 Results and Discussion

We begin our discussion with a direct comparison of three time-of-flight mass spectra obtained in different experimental scenarios as presented in Figure 6.1. The first graph, Figure 6.1a, is obtained after direct ionization of an effusive vanadium oxide beam by

electron impact at 20 eV. Two groups of peaks appear, which can be assigned to the structures $(V_2O_5)_2$, $(V_2O_5)_3$, and to fragments of both, with one or two oxygen atoms removed. In Figure 6.1b, the same effusive beam is ionized by electron impact with an energy of 89 eV, an energy commonly applied in commercial mass spectrometer. It shows a similar mass distribution in the range between about 300 and 600 amu, but also the onset of the next multiple of the V_2O_5 unit, in this case $(V_2O_5)_4$. From now on, we will refer to the clusters built from this unit as $(V_2O_5)_n$ oligomers. In contrast, the spectra below 364 amu look entirely different for both choices of electron impact voltage. The appearance of numerous fragments for ionization at 89 eV, while none of these peaks is visible at 20 eV, renders direct ionization at larger energies as a highly invasive method of detection, altering the actual distribution of cluster sizes significantly. However, the spectra obtained by indirect ionization within the helium droplets, as illustrated in Figure 6.1c, suggests an even less destructive effect despite using the same electron impact voltage of 89 eV, as it shows very regular and nicely grouped patterns of peaks which can be assigned to oligomers with $n = 2$, 3 and 4. This experimentally well-documented[31,172,173] and beneficial side-effect of He-droplet immersion is still not fully understood. For a tentative explanation, we refer to a recent review article[31] on the matter, stating that chances for a He-immersed molecule to survive ionization without fragmentation is increasing with droplet size, most likely due to a more efficient, rapid cooling of the vibrationally hot molecular ions.

Note the lack of a clearly distinguishable V_2O_5 signal in all spectra of Figure 6.1. This interesting detail will become highly relevant for the interpretation of the extended mass spectra presented in Figure 6.2, which continues the He-droplet-mediated spectra towards higher masses up to 5000 amu. On the left side of the spectrum in Figure 6.2 the helium droplet distribution is visible again, with peaks separated by exactly 4 amu (see Figure S1 of the ESI for details), but in the relevant region above 330 amu the clearly distinct series of $(V_2O_5)_n$ oligomer peaks is dominating the spectra. Each of these main peaks is followed by a characteristic series of smaller signals with a mass difference of 18 amu. They stem from the inevitable pickup of water molecules as adsorbants, a typical contaminant in He droplet experiments.[174] During heating, also the desorption of molecular oxygen from bulk V_2O_5 can be observed,[175] giving rise to a higher background pressure of O_2 (peak at 32 amu), and, as a direct consequence, the occurrence of molecular oxygen as a second yet barely noticeable contaminant of the V_2O_5 oligomeres (see Figure S1 of the ESI).

Two very interesting features become evident on the larger scale: First, the smallest oligomer is the $(V_2O_5)_2$ dimer, which also exhibits the highest abundance. Second, the oligomers themselves show a preference for even numbers of n. Mass peaks of oligomers with even n are significantly higher than those for odd n. This oscillating pattern is very pronounced for smaller oligomers but gets weaker at higher masses. However, a difference of one to two orders of magnitude can be observed even up to $n = 8$. The first

observation is in good agreement with previous studies on the evaporation of V_2O_5.[176] The observed even-odd oscillations in n will be explained later in the text.

Two explanations are conceivable for the experimental results. The first is to assume the existence of magic numbers for the oligomers due to electronic or structural advantages in finite geometries, a well-known phenomenon which is typical and well documented e.g. for clusters formed by rare gas atoms (for geometrical reasons) or metal atoms (for electronic reasons). This hypothesis is easily tested by density functional theory (DFT) calculations on the free $(V_2O_5)_2$ oligomers in gas phase. Previous studies on neutral clusters,[177] negatively[178–181] or positively charged fragments,[167,181] coordinated clusters or clusters in solution,[155] indicate a larger number of more or less stable stoichiometries, mostly with slight deviations from the stoichiometry found in the bulk material. In particular, the Sauer group provided a deep and systematic structural and vibrational analysis of vanadium oxide cluster cations to support gas phase infrared spectroscopy measurements.[182] In this context, also peroxo and superoxo species were of special interest due to their role in re-oxidation processes during catalytic reactions.[183] However, to the knowledge of the authors, no study has set a special focus yet on the formation process and the resulting size distribution of pristine vanadium oxide nanostructures with exact bulk stoichiometry, as one would expect to find them in a chemically unperturbed phase transition from solid to gas phase under fully inert conditions as they are provided in helium droplet experiments. Closest to our current interest is a theoretical study of Vyboishchikov and Sauer,[177] which compares the bulk structure and the neutral $(V_2O_5)_n$ oligomers up to $n = 12$, but is not concerned with sublimation energies.

The structures obtained in fully unconstrained energy minimizations with the ωB97X-V functional[184] and their corresponding energies for oligomers with $n = 1$ to 6 are presented in Figure 6.3, where we have divided the total electronic energy obtained for each oligomer by its corresponding number of building units. Structural comparison identifies ring closure of $(V_2O_5)_n$ chains as the underlying formation principle. The neutral structures are very similar to those reported earlier except for $(V_2O_5)_2$, where a ring-like structure, originally termed as '4-square D_{2h}', is also slightly preferred over the tetragonal, Jahn-Teller-distorted D_{2d} arrangement named '4-Tetra'.[177,180] However, the curve in Figure 6.3, binding energy per unit as a function of n, is monotonically decreasing, which refutes the assumption of magic numbers in neutral cluster formation. This test has been repeated for the cations with a similar outcome (see Figure S4 in the ESI for details), which further excludes a varying stability of the oligomers after ionization as a valid argument.

This leaves us with the second hypothesis only, which assumes a direct impact of the actual sublimation process on the size distribution of the free gas oligomers. Vanadium(V) oxide crystalizes in an orthorhombic layer-type structure (*Pmmm*). In a first attempt to study the solid to gas phase transition we perform now periodic DFT calculations on a pristine single layer of bulk vanadium(V) oxide with the PBE functional.

Next, we perform a stepwise removal of V_2O_5 building units and repeat the optimization of the layer in order to obtain reconstruction energies after sublimation. Together with energy calculations for the fully relaxed free gas oligomers within the same computational approach we can estimate the electronic energies for the sublimation of n units via

$$E(n) = (E_{\text{surf}-n\cdot\text{u}} + E^n_{cluster}) - E_{surf}, \tag{6.1}$$

with E_{surf} and $E_{\text{surf}-n\cdot\text{u}}$ as the total electronic energy of the surface before and after the removal of n units, and $E^n_{cluster}$ denoting the electronic energy of a free gas cluster built from n units. Structures of the pristine as well as the distorted layers are depicted in Figure 6.4. Our choice of which V_2O_5 unit to remove follows minimum energy criteria. To keep the inevitable bias, introduced by a supercell of finite size, at a minimum, we limit our study to a removal of not more than four units from the bulk surface. In the next step, these energy differences are corrected for thermochemistry. Assuming the same entropy contributions for the pristine and the distorted bulk surface layer, such a correction reduces to the evaluation of entropy and enthalpy contributions for the free gas oligomers. For higher accuracy, we use the values obtained via frequency calculations obtained with the ωB97X-V functional,[184] calculated at T=1000-1400 K and a pressure of 10^{-3} mbar, and add them to the electronic energies obtained in the periodic calculations. Entropy values have been corrected according to Ref. 185 for improved estimates of contributions from low-lying vibrational frequencies.

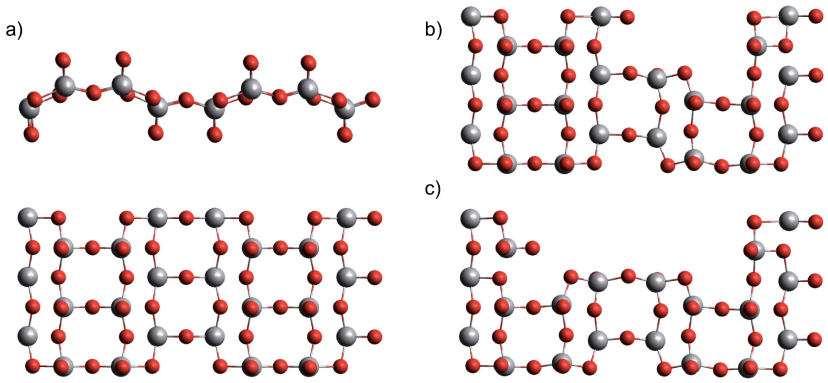

Figure 6.4: Single layer of bulk vanadium(V) oxide in two views (a), after removal of one (b) or two (c) V_2O_5 units.

The resulting Gibbs energy differences are plotted in Figure 6.5, together with the electronic energy differences at 0 K, and scaled to energies per detached V_2O_5 unit. We find a clear preference for the sublimation of pairs over the detachment of single units. With increasing temperature, the sublimation of dimers becomes most feasible (followed by tetramers and trimers), which immediately explains the abundance of the $(V_2O_5)_2$ dimer in the spectrum. Obviously, forming dimers upon sublimation is a compromise

between minimizing the reconfiguration costs of the detachment and maximizing the entropy by releasing as many particles as possible. The lower cost for the sublimation of pairs overcompensates the bisection of the number of free gas particles.

With this information the last piece of the puzzle is placed easily: The preference for even oligomers must be a direct consequence of this high abundance of dimers. The pickup probability can be estimated based on vapour pressure, average size of the helium droplets, and the length of the pickup zone (15 mm). For the chosen conditions, the occasional pickup of several dimers by the same droplet is very likely. We therefore conclude that larger oligomers are formed by typical coagulation processes inside the helium droplets[186] after a series of pickup events of mostly $(V_2O_5)_2$ dimers. Further evidence for the growth of larger oligomers from these dimers via coagulation is given in the SI, where mass spectra obtained at different nozzle temperatures are compared to each other. With decreasing nozzle temperature the He droplets increase in size and collect larger amounts of $(V_2O_5)_2$ units, which in turn allows for the synthesis of larger vanadium oxide structures and therefore extends the characteristic pattern of peaks in the spectra towards higher masses.

6.3 Conclusions

In summary, we have demonstrated that pure vanadium(V) oxide oligomers with correct stoichiometry can be produced by sublimation and follow-up pickup by superfluid helium droplets. Ionization, a necessary step for follow-up mass spectroscopy, is proven to be less destructive to the sublimated particles if the latter are immersed in He nanodroplets. Although the charge hopping process during ionization inside the droplets should deliver about the same excess energy as direct 20 eV electron bombardment, fragmentation seems to play a much smaller role. In agreement with other groups, we attribute this observation to the high cooling rate of the surrounding helium. The smallest building unit for the vanadium oxide oligomers observed in the mass spectra is $(V_2O_5)_2$, which is also the most abundant species in the helium droplet beam by far. We further observe a clear preference for $(V_2O_5)_n$ oligomers with even n inside the He nanodroplets. This is explained by a computational study on a single layer of bulk vanadium(V) oxide, which suggests a preferred sublimation of $(V_2O_5)_2$ dimers. The latter serve as building blocks for the coagulation of larger structures inside the droplets. Experimentally, these novel findings indicate the dawn of a new method for the in-situ coating of metallic nanoparticles with a metal oxide of high industrial relevance, as metal clusters can be synthesized simultaneously with the same experimental technique via a sequential pickup. Follow-up experiments on vanadium oxide-coated metal clusters are currently under way.

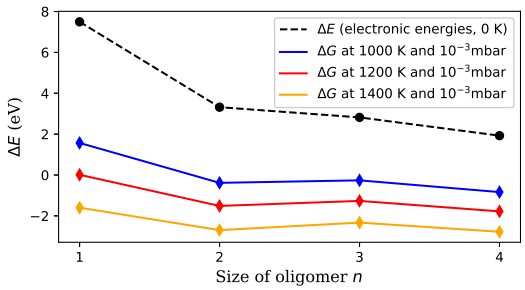

Figure 6.5: Sublimation energy per V_2O_5 unit, calculated at zero K and at experimental conditions. Sublimation starts around 1000 K, but is still not feasible for single units at this temperature. $(V_2O_5)_2$ detachment becomes preferred at higher temperatures, which explains the much higher abundance of $(V_2O_5)_n$ clusters with even n in Figure 6.2.

6.4 Methods

Experimental Setup

Highly purified He gas (99.9999 %, 20 bar) is expanded through a 5 μm nozzle into high vacuum with a base pressure of $\approx 10^{-5}$ mbar. The nozzle temperature is set around 9.2 K in order to produce helium droplets consisting of about 10^6 He atoms, formed in the process of the supersonic expansion.[187] The resulting droplet beam is cropped by a 400 μm skimmer before entering a separately pumped vacuum chamber for particle pickup. Details on the He droplet size distribution are given in Figure S2 of the ESI. A schematic of the whole apparatus is presented in Figure 6.6. The setup consists of three vacuum chambers, one for the helium droplet production (Source Chamber), one for the pickup of vanadia fragments from the gas phase (Pickup Chamber) and one for cluster analysis (Main Chamber).

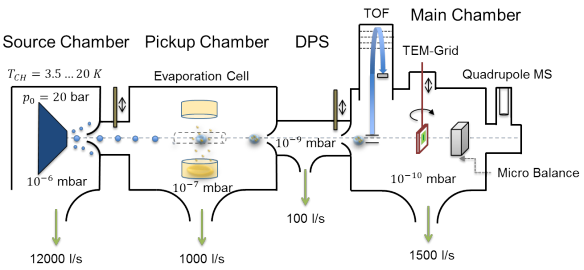

Figure 6.6: Schematic of the experimental setup used for the synthesis of $(V_2O_5)_n$ clusters inside liquid He droplets; see text for details.

By resistive heating of V_2O_5 oxide powder with a purity of 99.9 %, kept in a small quartz crucible (Kurt Lesker EVC2Q), to temperatures between 1000 to 1200 K, a vapour

pressure of $\approx 10^{-3}$ mbar is achieved.[188] The latter determines, together with the He droplet size and the length of the cell, the probability for a particle pickup from the gas phase, which offers a convenient handle for the amount of material brought into the He droplet beam. Each pickup event causes an evaporation of helium atoms from the droplet. This attenuation of the helium beam is measured with a quadrupole mass spectrometer (Balzers QMA 200/QME 200). After particle pickup, the He beam is again collimated by a 2 mm skimmer before entering the measurement chamber at a base pressure of approximately 10^{-10} mbar. The beam crosses the ionization region of a time-of-flight mass spectrometer (Stefan Kaesdorf RFT 50) designed for measurements of heavy compounds. ionization is achieved via electron impact, using electron energies of 89 eV, an average electron emission current of $\approx$10 μA and a repetition rate of 10 kHz. However, note that the short mean free path of electrons in liquid helium prevents a direct ionization of impurities inside of helium droplets consisting of about 10^5 He atoms or larger.[189] Typically, the ionization of an impurity inside the droplet takes place via secondary processes such as charge hopping[30] or Penning ionization[31], which impedes undesired fragmentation through electron impact. For measurements without He beam we close a valve between the source and pickup chamber, which leaves us with an effusive beam of vanadium oxide particles only. The detection chamber further contains a quartz crystal micro balance, which allows us to measure the total mass transported by the helium beam and acts as an additional analysis tool. For further details on the experimental setup we recommend reading of Ref. 72.

Computational Details

Our computational approach for the free-gas oligomers is based on the combination of a less expensive method for pre-optimization and structural search, in our case the GFN-xTB method of Grimme,[190] with the application of ωB97X-V,[184] a range-separated hybrid GGA density functional with VV10 nonlocal correlation,[191] as it is implemented in the Q-Chem program package.[192] For O we use the polarized triple-zeta basis set of Weigend and Ahlrichs,[193] for V the effective core potential and basis set of the LANL family.[194]

The vanadium(V) oxide surface is described via periodic DFT calculations, where the PBE functional[132] is used in combination with projected-augmented-wave (PAW) pseudopotentials[133,134] as implemented in the Quantum Espresso suite of programs.[195] A supercell containing 12 V_2O_5 building units has been chosen, with an initial geometry taken from Ref. 196. The geometry is allowed to fully relax, and the box dimensions in x and z directions are optimized. We obtain 22.741 and 10.710 Å, respectively. For the y or (010) direction a box length of 10 Å has been chosen to decouple the minimally interacting layers in our attempt to simulate the bulk surface. Energy cutoffs (90 Ryd for the energy, 1080 Ryd for the density) and y-distances have been tested in order to

provide an accuracy of 0.05 eV or 1 kcal/mol, which lies within the systematic error expected for the chosen functional.

Acknowledgements

This research has been supported by the Austrian Science Fund (FWF) under Grant PIR8-N34. Further support by NAWI Graz is gratefully acknowledged. The authors would like to acknowledge the use of HPC resources provided by the ZID of Graz University of Technology and by the Vienna Scientific Cluster (VSC).

7 Synthesis of Nanosized Vanadium(V) Oxide Clusters below 10 nm

The following corresponds to the publication
"Synthesis of nanosized vanadium (V) oxide clusters below 10 nm" by **Maximilian Lasserus**, Daniel Knez, Florian Lackner, Martin Schnedlitz, Roman Messner, Daniel Schennach, Gerald Kothleitner, Ferdinand Hofer, Andreas Wolfgang Hauser, Wolfgang E Ernst in *Physical Chemistry Chemical Physics* **21**, 121104-21108 (2019).

This publication can be found online:
`https://pubs.rsc.org/en/content/articlehtml/2019/cp/c9cp04357h`

The author of this thesis was responsible for

- the design and execution of the experiments,
- the evaluation of the obtained electron microscopy images,
- the evaluation of the obtained UV-vis spectra,
- the literature research and interpretation of the obtained data,
- and the authorship of the manuscript.

The contributions of the co-authors are listed below:

- Daniel Knez: recording of electron micrographs
- Florian Lackner: assistance in the experiment, manuscript editing
- Martin Schnedlitz: assistance in the experiment, manuscript editing
- Roman Messner: assistance in the experiment, manuscript editing
- Daniel Schennach: coding a new software for analysing the transmission electron images

- Gerald Kothleitner: supervision and funding (electron microscopy)
- Ferdinand Hofer: supervision and funding (electron microscopy)
- Andreas W. Hauser: supervision, manuscript editing
- Wolfgang E. Ernst: supervision, manuscript editing, funding

Reprinted with permission from "Synthesis of nanosized vanadium (V) oxide clusters below 10 nm" by **Maximilian Lasserus**, Daniel Knez, Florian Lackner, Martin Schnedlitz, Roman Messner, Daniel Schennach, Gerald Kothleitner, Ferdinand Hofer, Andreas Wolfgang Hauser, Wolfgang E Ernst in *Physical Chemistry Chemical Physics* **21**, 121104-21108 (2019).

Abstract

Vanadium oxide clusters with a mean diameter below 10 nm are investigated by high resolution Scanning Transmission Electron Microscopy (STEM), Electron Energy Loss Spectroscopy (EELS) and UV-Vis absorption spectroscopy. The clusters are synthesised by sublimation from bulk vanadium(V) oxide, in combination with a pick up by superfluid helium droplets. The latter act as reaction chambers which enable cluster growth under fully inert and solvent-free conditions. High-resolution STEM images of deposited vanadium oxide particles allowing for the determination of lattice constants, clearly indicate a dominating presence of V_2O_5. This finding is further supported by UV-Vis absorption spectra of nanoparticles after deposition on fused silica substrates, which indicates that the oxidation state of the material is preserved over the entire process. From the results of the UV-Vis measurement, the band gap of the nanosized V_2O_5 could be determined to be 3.3 eV. The synthesis approach provides a route to clean V_2O_5 clusters as it does not involve any surfactant or solvents, which is crucial for an unbiased measurement of intrinsic catalyst properties

7.1 Introduction

Interest in nanometer-sized metal oxide particles has been increasing in the last decades due to their numerous applications in catalysis, medicine, energy storage, electronics and optics.[11,197] When the diameters of such particles approach the sub 10 nm regime, the surface-to-volume ratio increases dramatically. The higher fraction of atoms at edges and corners reduces the mean coordination number, which enhances their chemical reactivity.[47]

Transition metal oxides have unique properties originating from the characteristics of the outer d-band electrons. Vanadium oxide is a prominent representative of this group of materials, and clusters consisting of it have been object of active research due to their numerous oxidation states and the relatively high abundance of the material. Theoretical and experimental studies of the structure and stability of small clusters of V_2O_5 have been performed by Sauer *et al.*[167,198–200]. Regarding strategies for a controlled synthesis of nanostructures, Limberg *et al.* showed that thin films of V_2O_5 can be obtained by vapour deposition of heated V_2O_5 powder.[201] However, to the knowledge of the authors,

none of the current techniques allows for a controlled coating with V_2O_5 nanoparticles. Among the possible applications, heterogeneous catalysis is probably the most important field,[202–206] but recent research efforts have also been dedicated to energy storage.[207]

For the synthesis of small ($\leq$10 nm) transition metal oxide clusters, solution based methods are often used, such as sol-gel techniques, microemulsions, micelle / reverse micelle methods or precipitation.[145–153] A disadvantage of all these techniques is the inevitable impact onto the product shape, structure and purity. An alternative approach is based on the evaporation of vanadium oxide with lasers, but has undesired side effects such as the production of highly reactive fragments, charged complexes and other unwanted by-products.[156,208]

In this paper we employ a different strategy to synthesise nanoparticles which is based on the accumulation of V_2O_5 oligomers in helium nanodroplets. The present work expands our previous experiments from the *in situ* characterisation of V_2O_5 oligomers in a helium droplet beam,[209] towards the formation of nanoparticle films comprising of individually deposited particles with diameters below 10 nm. After deposition, several *ex situ* measurement techniques can be applied to the particles in order to reveal their characteristics on different supports.

The synthesis method has its origin in spectroscopy,[55] where helium droplets have been used to assemble and investigate elusive molecules,[119] and has evolved into a versatile method for the production and subsequent deposition of metal clusters.[72,210] Using the helium droplet method for the synthesis of transition metal oxide clusters is a novel exertion of this well known synthesis technique and is a new step into understanding of these highly interesting materials.

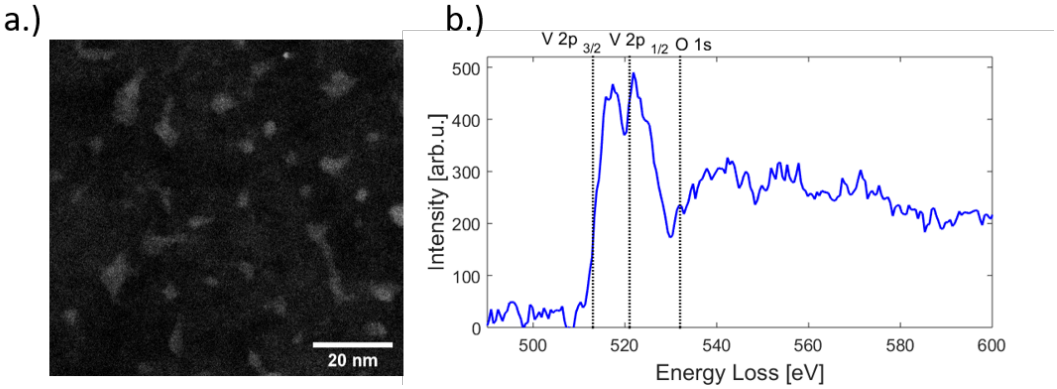

Figure 7.1: (a) HAADF image of V_2O_5 structures as seen in STEM, for cold head temperatures of 8, 6.7 and 5.4 K and deposited on one substrate. (b) EELS spectrum of a selected nanoparticle. The characteristic V-L_2, V-L_3 and the O-K edges are indicated by vertical dashed lines.[5]

7.2 Experimental Section

The experimental setup used for the synthesis of V_2O_5 clusters is described in detail in Ref. 72. A short overview is given in the following. High purity helium gas (99.9999 %) is expanded through a cooled 5 μm nozzle under a constant pressure of 20 bar into high vacuum ($\approx 5 \cdot 10^{-5}$ mbar), whereby helium droplets are formed. Depending on the nozzle temperature, different size distributions of droplets are accessible. In our experiment the nozzle temperature has been set to 5.4, 6.7 and 8 K, which corresponds to average sizes of $1.68 \cdot 10^{10}$, 1 to 6 $\cdot 10^7$ and $5.31 \cdot 10^6$ helium atoms per droplet, respectively.[211] For each temperature, a deposition time of $\approx$ 20 minutes was chosen. After the expansion the helium beam is cropped by a 400 μm skimmer before entering the next vacuum chamber with a pressure of $\approx 5 \cdot 10^{-6}$ mbar during deposition. Here, vanadium(V) oxide (V_2O_5, Matek Prod. Nr. 008133) with a purity of 99.9 % is placed in a quartz crucible (Kurt Lesker EVC2Q), surrounded by a tungsten heating basket (Kurt Lesker EVB8B3030W), and is resistively heated to temperatures between 1100 K and 1200 K. When heated, the vapour pressure of the desired material rises, creating a pick up zone above the basket. As documented in Ref. 209, small oligomers of vanadium pentoxide, preferably units of V_4O_{10}, tend to evaporate from the V_2O_5 powder upon heating. After collision with a helium droplet, these units of sublimated V_2O_5 remain attached and agglomerate to V_2O_5 clusters inside the droplet. The energy released in the process of bond formation during cluster aggregation is dissipated by the evaporation of helium atoms (approximately 5 cm^{-1} per He atom).[212] This evaporation is monitoredby a residual gas analyser (Balzer QMA 200/QME 200), by comparing the He signal before and during evaporation, providing a convenient way to monitor the doping level. After the pick up chamber the helium droplet beam is again cropped by a 2 mm skimmer before it enters the measurement chamber, with a pressure of $\approx 1 \cdot 10^{-8}$ mbar, during deposition. In this last chamber the clusters are deposited onto TEM grids. Additional diagnostic tools are installed to characterise the doped droplet beam.[72]

7.2.1 Scanning Transmission Electron Microscopy

After deposition on amorphous carbon grids under soft landing conditions,[72] the sample is exposed to ambient air during transport ($\approx$ 10 min) and insertion into a Scanning Transmission Electron Microscope (STEM), where the V_2O_5 particles are studied via a high-angular annular dark-field (HAADF) imaging detector at atomic resolution using a probe-corrected FEI Titan^3 G2 60-300 TEM. The microscope was operated at 300 keV achieving a resolution of $\approx$ 70 pm. A Gatan quantum energy filter, attached to the microscope, is employed for electron energy loss spectroscopy (EELS).

Vanadium has several stable oxides and a transition between them can be easily induced e.g. by temperature increase or by electron irridation. The reducing effect of the

electron beam during STEM measurements, in particular for nanostructured objects, is well known and also documented for the case of vanadium oxides.[213] In order to avoid any undesired reduction under the electron beam, the dose is kept as low as possible by using an electron current of 100 pA and short exposure times for each particle.[130]

7.2.2 UV-Vis Absorption Spectroscopy

UV-Vis absorption spectra were measured using a Shimadzu UV-1800 spectrophotometer. The V_2O_5 nanoparticles were deposited on a fused silica microscope slide (Corning 7980, fused silica, 1 mm thickness). After deposition the slide was taken out of vacuum and placed into the spectrometer to acquire the shown spectra. A second fused silica slide from the same patch was used as reference.

7.3 Results

7.3.1 STEM

A High Angle Annular Dark Field (HAADF) overview image of clusters is shown in Figure 7.1. Several bright nanostructures are distinguishable. Note that some elongated shapes are also visible (see in Fig.7.1 in the right lower corner), which is a typical side effect of our synthesis method. In larger helium droplets, created at nozzle temperatures below 8 K, metal clusters become elongated due to the presence of one-dimensional vortices inside the superfluid helium droplets along which the dopants preferentially agglomerate.[27,63,214]

The shape and size of the deposited nanostructures is revealed directly by the STEM images and can be explained by the He synthesis given certain helium droplet source conditions. However, a more challenging task is the determination of the oxidation state, i.e. the actual structural composition of the vanadium oxide after deposition. Electron energy loss spectroscopy (EELS) is an element-sensitive technique that can provide insights into the oxidation states of a material and is routinely employed for this purpose in transmission electron microscopy. The approach relies on the fact that near edge features as observed in EELS spectra are highly sensitive to the local valence electronic structure, which depends on the nature of chemical bonds in the material, in our case, the various types of V-O bonds in the nanoparticles. However, although EELS has been successfully employed in previous experiments on bulk vanadium oxide as well as thin films,[215–217] in this particular case the approach turned out to be futile due to the close proximity of the V L- and O K-edges. The low electron beam dosage mentioned above, a necessity to avoid particle damage and to prevent electron-beam induced reduction,[169] provides a rather weak EELS signal and a relatively low resolution compared to other published spectra. An EELS spectrum obtained from a nanoparticle

is presented in Figure 7.1, showing the L2 (V $2p_{1/2}$) and L3 (V $2p_{3/2}$) main features peaking at 517.1 and 522.7 eV, respectively. The V 2p L-edges as well as the O 1s K-edge are indicated by a vertical dashed line. However, due to the large number of possible oxidation states and the similarity in the EELS signal a distinct characterisation is not possible. A more detailed discussion of the EELS signal is provided in the SI.

As an alternative method to reveal the oxidation state, the lattice constants of the clusters were measured directly from HAADF images and comparedto bulk values. In order to do that, TEM images have been selected where suitable vanadium oxide particles with multiple grains were visually accessible at the same time.

In these cases, different lattice reflexes could be determined within the same particle, and the lattice constants could be derived as indicated in Figure 7.2, where regions of sufficient lattice contrast are highlighted. The black lines mark a group of lattice planes with a distance of 2.7 Å which can be assigned to the (011) plane of V_2O_5, while the blue lines mark a region in which the lattice reflexes have a spacing of 2.2 Å, which can be assigned to the (020) plane of V_2O_5. Another structure is presented in Figure 7.3, where a lattice spacing of 5.7 Å could be measured, which we assign to the (200) plane of V_2O_5.[218] For the sake of a direct comparison we plotted the known lattice constants of the vanadium oxides in Figure 7.4 together with the measured distances from Figure 7.3 and Figure 7.2.[6–10] The displayed reflexes are simulated from the published lattice parameters using the software Vesta.[219] The coloured area mimics the uncertainty of the microscope and therefore indicates the possible reflexes of each oxide. Hereby, the only oxide offering significant lattice reflexes in all marked regions is V_2O_5. Within the recorded images, we did not find a lattice distance between 4 and 4.5 Å. The lack of these reflexes may be due to the limited number of clusters with respective lattice orientations observable during the experiment. However, together with our spectral observation (see below) we consider the result as strong evidence for that the oxidation state of the nanoparticles is preserved, starting from their growth in the He droplets from sublimated V_2O_5 fragments, up to their final deposition on the support.

The size distribution of the V_2O_5 clusters was determined by analysing the HAADF images. A total of 523 clusters has been investigated to produce a typical log-norm distribution as shown in Figure 7.5. The larger part of the synthesised clusters has a size below 10 nm.

7.3.2 UV-Vis Absorption Spectroscopy

To determine the dominant oxidation state of the deposited clusters, UV-Vis absorption spectroscopy serves as an additional method for the investigation of the chemical composition of the V_2O_5 particles. In Figure 7.6 a) the clusters show a strong absorption in the UV region, but are transparent in the visible and IR regime. The recorded spectrum agrees well with the absorption spectrum of V_2O_5, which, among all the previously stud-

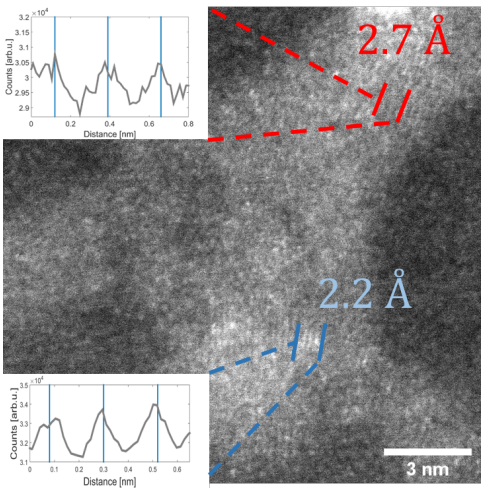

Figure 7.2: STEM HAADF image of a V_2O_5 particle (synthesised at 5.4 K cold head temperature). Two regions are marked where lattice constants could be extracted from the image. The respective intensity profile between the lines is shown in the inset. The black lines indicate a group of planes with a spacing of 2.7 Å the blue lines mark a group of planes with a spacing of 2.2 Å.

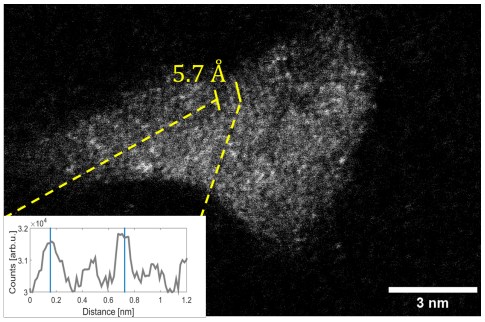

Figure 7.3: STEM HAADF image of a V_2O_5 structure (synthesised at 5.4 K cold head temperature). The intensity profile of the local structure between the yellow lines is shown in the left corner. The distance of the peaks is marked by blue lines indicating the lattice distance of 5.7 Å.

ied vanadium oxides, is the only species that exhibits no absorption in the visible.[11] This can be seen clearly from Figure 7.6 b) which contains a direct comparison to spectra taken from Ref. 11. The band gap of the prepared samples has been determined as 375 nm (3.3 eV) from a line-fit to the decreasing absorption in the UV, indicated in Figure 7.6 (dashed line). The value is higher than the reported value of bulk (2.3 eV, see Ref. 220) but smaller than the HOMO-LUMO gap known for the molecular $(V_2O_5)_2$ dimer (4.4 eV, see Ref. 221). As clusters in the sub 10 nm regime are bridging the gap between bulk and molecules, it appears reasonable that the obtained value resides between these

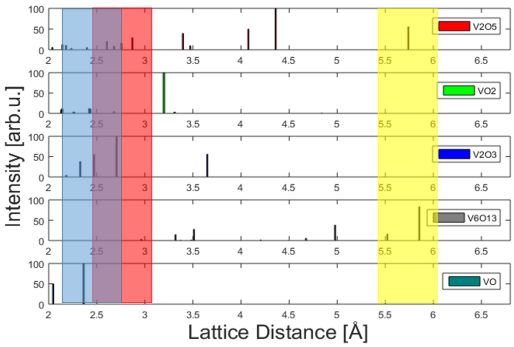

Figure 7.4: A comparison of lattice constants for various vanadium oxides. The measured lattice constants derived from Figures 7.2 and 7.3 and their uncertainty due to the limited resolution are represented by the coloured areas. The colours represent the respective marking in each Figure. By comparison to known, much better resolved peak positions taken from powder diffraction measurements, V_2O_5 is identified as the most likely oxide.[6–10]

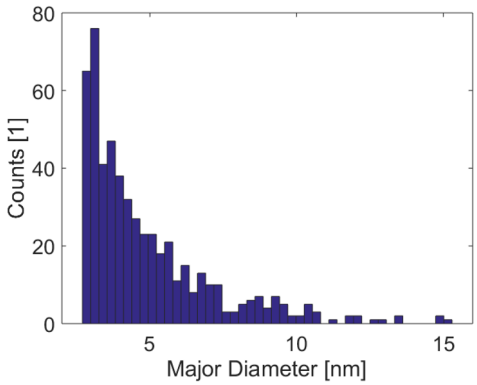

Figure 7.5: Size distribution of V_2O_5 clusters derived from HAADF images providing a total cluster count of 523. 'Major diameter' refers to the longest distance within a cluster. A cutoff below 2 nm was used to exclude noise. This is the total size distribution from the deposition at nozzle temperatures of 8, 6.7 and 5.4 K on one substrate.

two cases.

7.4 Conclusion

V_2O_5 clusters with a size distribution ≤ 10 nm have been synthesised through sublimation from bulk, helium-assisted growth and follow-up deposition. EELS measurements confirm the presence of vanadium, but did not provide further information on oxidation

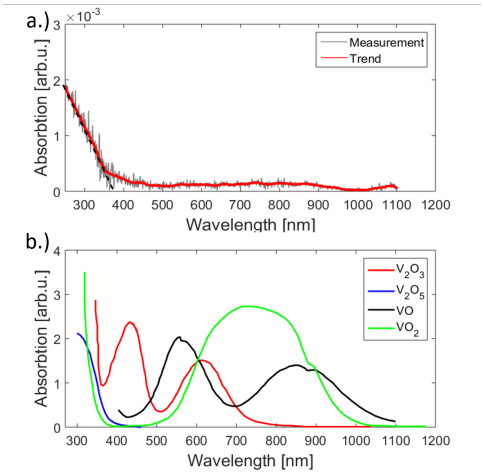

Figure 7.6: UV-vis absorption spectra of the synthesised V_2O_5 clusters on fused silica (a) and reference spectra taken from Ref. 11 (b). An absorption near the ultraviolet region is evident for the measured signal. The spectrum was acquired by subtracting the signal of a plane spot at the support and the spot of cluster deposition. When comparing the reference spectra to the measurement, the similarity to the V_2O_5 is visible.

states. Therefore, the chemical stoichiometry of the synthesised clusters was determined based on lattice distances as measured from HAADF images. We find best agreement with reflexes of vanadium(V) oxide, a suggestion which is further confirmed by UV-Vis absorption measurements. In the course of the latter also a band gap of 3.3 eV could be determined for nanostructured V_2O_5 clusters with average sizes below 10 nm. This confirms that the chosen way of particle synthesis through helium droplets does not affect the chemical composition of V_2O_5, which suggests future combinations with other metal impurities during synthesis in order to produce application-tuned nanostructured catalyst materials.

Acknowledgements

This research has been supported by the Austrian Science Fund (FWF) under Grant FWF PIR8-N34. Further support by NAWI Graz is gratefully acknowledged. F.L. and R.M. acknowledge support by the Austrian Science Fund (FWF) under Grant FWF P30940-N36. We thank the Institute of Solid State Physics at Graz University of Technology for providing helpful discussion and access to the UV-Vis spectrophotometer.

8 Conclusion

Within this thesis, two main scientific topics are presented. First, the diffusion on the nanoscale and second the synthesis of vanadium oxide clusters. All nano structures were synthesized in superfluid helium droplets, therefore solvent-free conditions could be assured.
This circumstance was important for the examination of Ag@Au clusters with a mean size below 10 nm. The determination of the diffusion characteristics has been achieved with a promising precision. A new method was established, which uses the change in intensity of a core@shell cluster in HAADF images during temperature induced alloying. During this process, 2-dimensional intensity profiles of the clusters were taken. Due to the change in each temperature step, the diffusion could be monitored until total alloying occurred.
Bimetallic clusters in a core@shell configuration of Fe@Au were also synthesized. Here the minimal covering layers of Au were determined, to inhibit the oxidation of the Fe core. The sample was kept under ambient conditions for a short period of time to enable oxidation of the Fe cores. With the use of STEM measurements, a total of 3 atomic layers of Au was found to be sufficient to prevent the Fe from oxidation. This result was strengthened by theoretical studies of the Au and Fe interface layer. For this system, a strong rise in energy was determined if the Fe atom would transit three layers of Au in comparison to two. During the measurement also the first core@shell@shell structure, synthesised by helium droplets, was found, namely Fe@Au@Fe_3O_4.
After the diffusion measurements were performed the aim of the work changed. The new orientation was caused by external input. We changed the aim to the creation of V_2O_5 clusters and studied their formation in the helium droplet. Here an unusual phenomenon was observed within the Time-of-flight mass spectrum. The vanadium oxide evaporated in units bigger than the molecular unit at temperatures between 1000 and 1200 K. The sublimation of V_4O_{10}, V_6O_{15} and V_8O_{20} could be identified within the mass spectra. Additional fragmentation of these molecules appeared in the mass spectra due to the electron impact ionisation. Theoretical calculations for the desorption behaviour of a V_2O_5-surface confirmed this experimental observation. A significant reduction of the fragmentation due to the surrounding helium droplet was measured. Additionally, the formation of larger $(V_2O_5)_2$ clusters inside the helium droplet was observed.
For bigger droplets and higher residual pressures of the V_2O_5, clusters in the size regime of several nanometers could be synthesized. The chemical composition of the deposited

clusters was also possible by using the STEM images and the UV-vis spectrometry. Due to the combination of these measurement techniques the material of the clusters could be determined as V_2O_5.
As an additional task a chamber to measure catalytic activity of the synthesized clusters was built using a template which was previously designed. Unfortunately no catalytic activity of synthesized clusters was detectable. As a future improvement, the usage of a different QMS should be proposed.

9 Acknowledgement

Am Schluss meiner Arbeit möchte ich mich bei allen Menschen bedanken die mich beim Schreiben dieser Arbeit untersützt haben.
Meinem Betreuer Prof. Wolfgang E. Ernst danke ich für die Narrenfreiheit die ich doch sehr genossen habe um die Arbeit in viele Richtungen zu erweitern. Ich glaube ohne das Verständiss wäre in dieser Arbeit nicht halb so viel zu Beschreiben.
Meinem Zweitbetreuer Prof. Andreas Hauser, der die Hoffnung in experimentelle Messungen immer aufrecht gehalten hat und immer mit neuen Ideen aufwartete.
Meinen Kollegen Roman Messner, Alexander Schiffmann, Thomas Jauk und Florian Lackner möchte ich für die tolle Zusammenarbeit und die entspannenden Kaffeepausen danken.
Auch vielen Dank an Daniel Knez, ohne seine Fähigkeiten am Elektronenmikroskop wäre alles schwerer gewesen.
Meinen nun schon seit knapp achtzehn Jahren langen Freund Martin Schnedlitz, mit dem ich nun seit der ersten Klasse des Gymnasiums zusammen für Prüfungen gelernt habe und die ganze Zeit des Studiums. Wir durften uns nun auch zusammen ein Büro teilen.
Vielen Dank Sonya für das Verständis, dass die Arbeit leider sicher 1000 mal länger gedauert hat als wir ausgemacht hatten.

Am meisten will ich mich bei meinem Vater bedanken. Mein ganzes Studium wäre nicht möglich gewesen hättest du nicht seit meinem Kindersalter davon geredet und mich immer und überall unterstützt. Besonders in den letzten Jahren hast du mich dazu motiviert nach dem Diplom das Doktorat zu machen. Es erfüllt mich mit Trauer, dass du das Ende meines Studiums nicht mehr erleben durftest.

10 Appendix

Wihtin this chapter the Supporting Informations of the articles in the main text are displayed as they are accessible in the respectively journals.

Thermally induced alloying processes in a bimetallic system at the nanoscale: AgAu sub-5 nm core-shell particles studied at atomic resolution

Maximilian Lasserus,[†] Martin Schnedlitz,[†] Daniel Knez,[‡] Roman Messner,[†] Alexander Schiffmann,[†] Florian Lackner,[†] Andreas W. Hauser,[*,†] Ferdinand Hofer,[‡] and Wolfgang E. Ernst[*,†]

†*Institute of Experimental Physics, Graz University of Technology, Petersgasse 16, A-8010 Graz, Austria. Fax: +43 (316) 873-108140; Tel: +43 (316) 873-8157; +43 (316) 873-8140;*

‡*Institute for Electron Microscopy and Nanoanalysis & Graz Centre for Electron Microscopy, Graz University of Technology, Steyrergasse 17, A-8010 Graz, Austria.*

E-mail: andreas.w.hauser@gmail.com; wolfgang.ernst@tugraz.at

In the first section of this Supporting Information we present a schematic of our experimental setup. In Section 2 additional TEM images of bimetallic core@shell clusters is provided. The application of the CALPHAD method to the AgAu system is demonstrated in Section 3. This section contains all formulas and parameters needed to generate phase diagrams for bimetallic AgAu particles of any radius and composition.

1 Details of the Experimental Apparatus

In order to provide a more detailed description of the actual experimental setup we present a schematic of the whole apparatus in Figure 1. The setup consists of three vacuum chambers, one for the helium droplet production (Source Chamber SC), one for the dotation of the droplets with metal species (Pickup Chamber PC) and one for cluster analysis and deposition on TEM grids (Main Chamber MC).

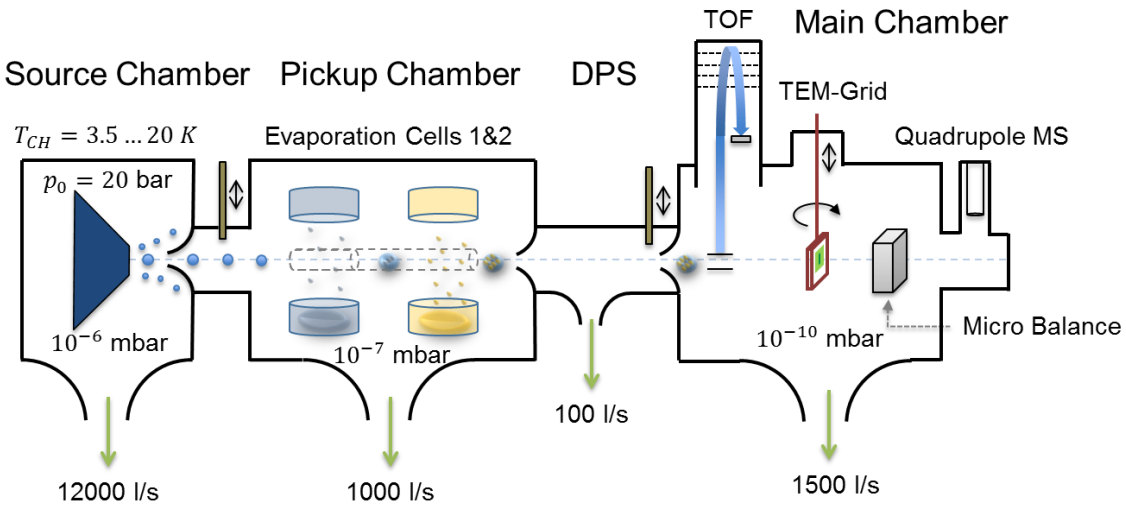

Figure 1: Schematic of the experimental setup used for the synthesis of metal clusters inside liquid He droplets; see text for details.

In the SC, a beam of liquid He droplets is produced by the expansion of He at 20 bar into vacuum through a nozzle cooled by a cold head with temperatures between 3.5 and 20 K. The droplets are then doped inside the PC with up to two metal species. The metal atoms stick to the droplets and form clusters inside during their time of flight from the PC through a differential pumping stage (DPS) to the MC. Inside the MC, a TOF-MS is used for the *in situ* analysis of the cluster size either by electron impact ionisation or via laser-induced photoionisation. A quartz crystal microbalance is used for the determination of the total amount of deposited metal. A quadrupole mass spectrometer is used to analyse the remaining residual gas. It allows us to determine the total amount of helium flow as well as the actual size of He droplets. The MC also contains a manipulator for the insertion and

the adjustment of TEM grids or other supports.

The size of the metal clusters can be adjusted via the size of the helium droplets which is manipulated via the stagnation temperature, the pressure, and the temperature of each evaporation cell in the PC. Before depositing clusters on heatable TEM grids, their size distribution is analysed via a time-of-flight mass spectrometer, the micro-balance, and the monitoring of the evaporated helium via a quadrupole mass spectrometer.

2 Additional TEM imagery

In this section additional HAADF TEM studies of core@shell clusters are provided. The experimental studies have been performed with a FEI Titan^3 G2 60-300 at 300 kV. In Figure 2, the images of nine different core@shell clusters at room temperature are presented. Pictures 1-5 show Ag@Au configurations, pictures 6-9 depict Au@Ag configurations. As mentioned in the main article, the difference in the intensity is caused by the different Z-contrast of gold and silver, allowing for a visual discrimination of core and shell areas with this technique.

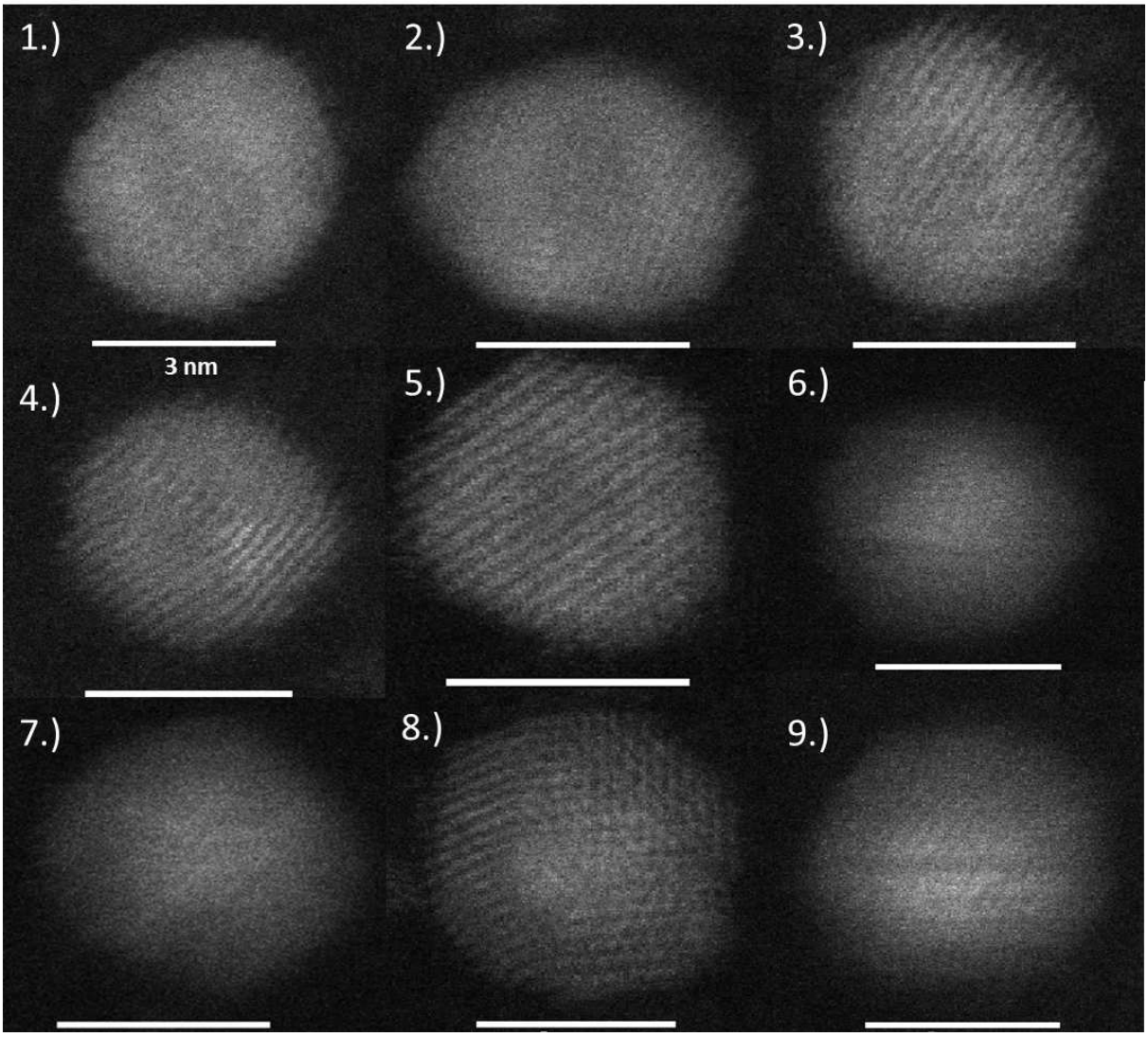

Figure 2: TEM images of five Ag@Au clusters (1-5) to four Au@Ag clusters (6-9), taken at room temperature. The inverted structure is obvious from the difference in contrast, although the core-shell feature is optically more pronounced if silver is the core element encapsulated in a shell of gold.

3 Application of the CALPHAD method to the AgAu system

In this section we list the reassessed Gibbs energies which are used to calculate the phase diagrams for the AuAg alloy as a function of the particle size and temperature for the liquid (L) and the solid (S) phase. The numerical values are taken from Ref. 1.

$$
\begin{aligned}
G^L_{Ag}(T<1234,r) &= \left(3815.93+\frac{2.462\cdot10^{-5}}{r}\right)+\left(109.302897-\frac{1.91\cdot10^{-9}}{r}\right)T \\
&- 23.8463316T\log(T)-\left(0.001790585+\frac{5.18\cdot10^{-13}}{r}\right)T^2 \\
&- 3.98587\cdot10^{-7}T^3-12011T^{-1}-1.04452328\cdot10^{-20}T^7 \\
G^L_{Ag}(T>1234,r) &= \left(-3583.962+\frac{2.46\cdot10^{-5}}{r}\right)+\left(180.95395-\frac{1.91\cdot10^{-9}}{r}\right)T \\
&- 33.472T\log(T)+\frac{-5.18\cdot10^{-13}}{r}T^2 \\
G^L_{Au}(T<1336.15,r) &= \left(-3352+\frac{2.73\cdot10^{-5}}{r}\right)+\left(215.885-\frac{7.98\cdot10^{-10}}{r}\right)T \\
&- 40.73T\log(T)+\left(0.0128756-\frac{2.18\cdot10^{-13}}{r}\right)T^2-2.535266\cdot10^{-6}T^3 \\
&+ 846536T^{-1}-7.069217\cdot10^{9}T^{-3}-3.5899325\cdot10^{-21}T^7 \\
G^L_{Au}(T>1336.15,r) &= \left(23570+\frac{2.73\cdot10^{-5}}{r}\right)+\left(89.502-\frac{7.98\cdot10^{-10}}{r}\right)T \\
&- 23.454T\log(T)-\left(2.18\cdot\frac{10^{-13}}{r}\right)T^2-8892561.16T^{-1} \\
G^S_{Ag}(T<1234,r) &= \left(-7209.512+\frac{4.75\cdot10^{-5}}{r}\right)+\left(118.200734-\frac{1.33\cdot10^{-8}}{r}\right)T \\
&- 23.8463316T\log(T)-0.001790585T^2-3.98587\cdot10^{-7}T^3-12011T^{-1} \\
G^S_{Ag}(T>1234,r) &= \left(-15094.864+\frac{4.75\cdot10^{-5}}{r}\right)+\left(190.26484-\frac{1.33\cdot10^{-8}}{r}\right)T \\
&- 33.472\log(T)-1.40918321\cdot10^{29}T^{-9}
\end{aligned}
$$

$$
\begin{aligned}
G^S_{Au}(T<1336.15,r) &= \left(-15745+\frac{4.380\cdot10^{-5}}{r}\right)+\left(225.142-\frac{9.67\cdot10^{-9}}{r}\right)T \\
&- 40.73T\log(T)+0.0128756T^2-2.535266\cdot10^{-6}T^3+846536T^{-1} \\
&- 7.069217\cdot10^{9}T^{-3} \\
G^S_{Au}(T>1336.15,r) &= \left(10886+\frac{4.380\cdot10^{-5}}{r}\right)+\left(98.987-\frac{9.67\cdot10^{-9}}{r}\right)T \\
&- 23.454T\log(T)-8892561.1T^{-1}+1.72894275\cdot10^{29}T^{-9} \\
G^L_{Ex}\left(X_{Au},X_{Ag},T,r\right) &= X_{Au}X_{Ag}\left(\left(-16402\frac{3.22\cdot10^{-7}}{r}\right)+\left(1.14-\frac{6.834\cdot10^{-10}}{r}\right)T\right) \\
&+ \left(\frac{-7.987\cdot10^{-7}}{r}+\frac{3.349\cdot10^{-10}}{r}T\right)\left(X_{Ag}-X_{Au}\right) \\
&+ \left(\frac{-1.04\cdot10^{-8}}{r}+\frac{2.373\cdot10^{-10}}{r}T\right)\left(X_{Ag}-X_{Au}\right)^2 \\
G^S_{Ex}\left(X_{Au},X_{Ag},T,r\right) &= X_{Au}X_{Ag}\left(\left(-15599-\frac{1.6484\cdot10^{-6}}{r}\right)+\frac{-5.7866\cdot10^{-10}}{r}T\right) \\
&+ \left(\frac{-1.9979\cdot10^{-9}}{r}+\frac{-2.8715\cdot10^{-10}}{r}T\right)\left(X_{Ag}-X_{Au}\right) \\
&+ \left(\frac{-1.30421\cdot10^{-7}}{r}+\frac{-6.755\cdot10^{-11}}{r}T\right)\left(X_{Ag}-X_{Au}\right)^2
\end{aligned}
$$

With these expressions, a total Gibbs free energy for both the liquid and the solid phase can be calculated,

$$
\begin{aligned}
G^L_{tot}\left(X_{Au},X_{Ag},T,r\right) &= G^L_{Ex}\left(X_{Au},X_{Ag},T,r\right)+X_{Au}G^L_{Au}(T,r)+X_{Ag}G^L_{Ag}(T,r) \\
&+ RT\left(X_{Au}\log\left(X_{Au}\right)+X_{Au}\log\left(X_{Au}\right)\right), \\
G^S_{tot}\left(X_{Au},X_{Ag},T,r\right) &= G^S_{Ex}\left(X_{Au},X_{Ag},T,r\right)+X_{Au}G^S_{Au}(T,r)+X_{Ag}G^S_{Ag}(T,r) \\
&+ RT\left(X_{Au}\log\left(X_{Au}\right)+X_{Au}\log\left(X_{Au}\right)\right),
\end{aligned}
$$

(1)

which determines the phase (liquid, solid, coexistence) of the system for any metal ratio, particle radius and temperature.

References

(1) Lee, J.; Sim, K. J. General equations of CALPHAD-type thermodynamic description for metallic nanoparticle systems. *Calphad* **2014**, *44*, 129 – 132sol, Special Issue: TOFA 2012 Discussion Meeting on Thermodynamics of Alloys.

Electronic Supplementary Information: On the passivation of iron particles on the nanoscale

Maximilian Lasserus,[†] Daniel Knez,[†] Martin Schnedlitz,[†] Andreas W. Hauser,[*,†] Ferdinand Hofer,[†] and Wolfgang E. Ernst[*,†]

†*Institute of Experimental Physics, Graz University of Technology, Petersgasse 16, A-8010 Graz, Austria. Fax: +43 (316) 873-108140; Tel: +43 (316) 873-8157; +43 (316) 873-8140;*

‡*Institute for Electron Microscopy and Nanoanalysis & Graz Centre for Electron Microscopy, Graz University of Technology, Steyrergasse 17, A-8010 Graz, Austria.*

E-mail: andreas.w.hauser@gmail.com; wolfgang.ernst@tugraz.at

In the first section of this Supporting Information we present a simplified graphical overview of our experimental setup. Section 2 contains a statistical evaluation of the species deposited on the TEM substrate. Section 3 discusses a model in which the core/shell ratio of ideal icosahedral clusters is analyzed, and uses this information to correlate doping rates to actual compositions for the various particle sizes. Section 4 lists the geometries of all intermediate states after atomic swapping as obtained from DFT optimizations.

Contents

1 Experimental setup

A schematic of the He-droplet apparatus is presented in Figure 1. Our setup consists of three vacuum chambers, one for the helium droplet production (Source Chamber SC), one for the doping of the droplets (Pickup Chamber PC), containing the two evaporation cells filled with Fe and Au, and one for mass spectra analysis and the deposition on TEM grids (Main Chamber MC).

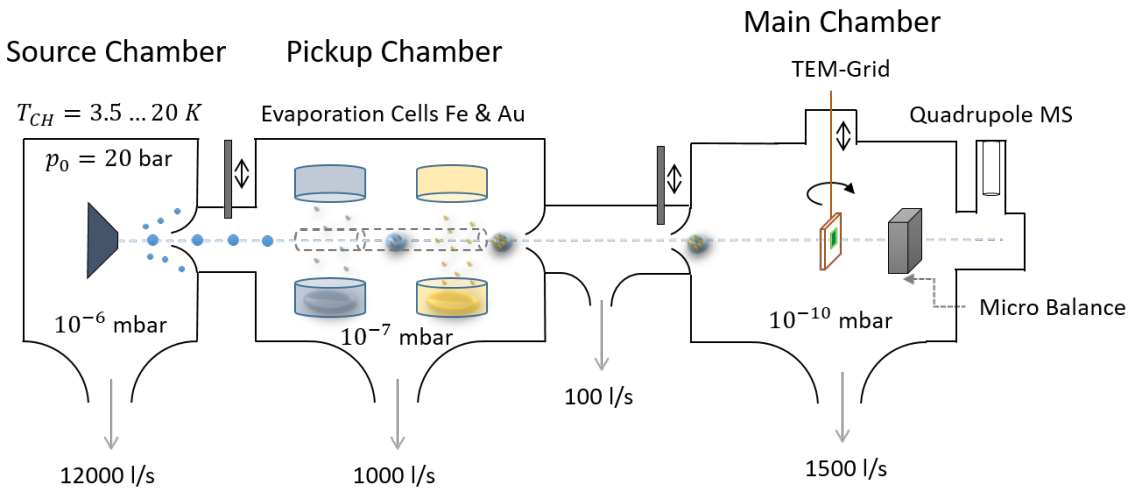

Figure 1: Schematic of the experimental setup used for the synthesis of Fe/Au nano structures inside liquid He droplets; see text for details.

2 Types of metallic particles and their distribution

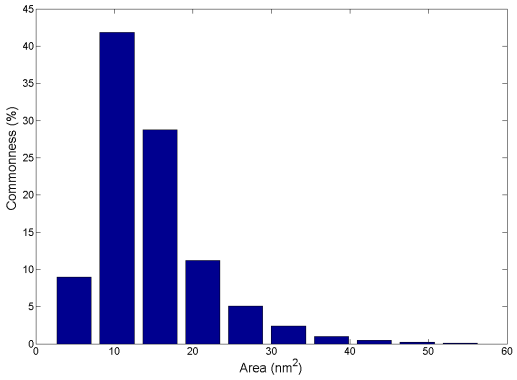

Figure 2: Histogram of sizes (area) of metallic particles synthesized and deposited in the current setup.

Figure 2 shows the size distribution of metallic structures deposited on the TEM grid in the course of He-mediated synthesis. The histogram is based on a classification of ≈ 1000 metal clusters (mixed and pure metal clusters).

A pie chart of the types of mixed-metallic nanoparticles (i.e. excluding pure Fe ad Au clusters) is presented in Figure 3. It is based on a data set comprising ≈ 530 clusters whose structure could be clearly identified. In total, only 8 % of these mixed structures correspond to successfully passivated Fe cores, the rest is formed by the particularly interesting 3-layered, partially oxidized structures (32 %) and the fully oxidized particles (60 %). The latter can be further divided into core@shell and janus structures, showing a slight preference for the janus-type (36 %).

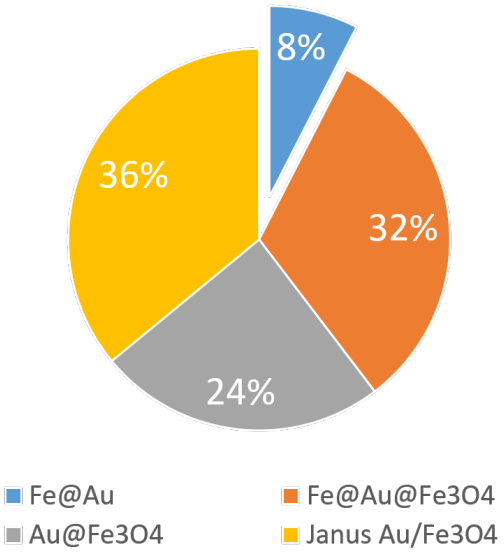

Figure 3: Distribution of nanostructures obtained via a two-step doping of helium droplets.

3 Closed shell model

The main manuscript mentions the variation of the doping rate as a convenient handle to control the distribution of Fe and Au the nano structures. Table 1 correlates the doping ratio with the number of of atoms in a cluster of certain size and its estimated number of Au layers. This estimation is based on a simple model assuming magic numbers of icosahedral core@shell geometries which are reasonably close to the desired ratio. It spans different cluster sizes from 1000 to 5000 atoms; the ratio is varied from 25 to 50 and 75 % Fe. Note that three additional shells as required for the effective passivation of the Fe core can be realized only in mixtures containing 25 % of Fe or less.

Table 1: Correlations between doping ratio, number of atoms, and estimated layers of shell material.

clusters atoms	**≈25% Fe**			**≈50% Fe**			**≈75% Fe**		
	N_{Fe}	N_{Au}	Sum	N_{Fe}	N_{Au}	Sum	N_{Fe}	N_{Au}	Sum
1000	147	776	923	561	854	1415	561	362	923
	3	*6*	*3 shells*	*5*	*7*	*2 shells*	*5*	*6*	*1 shell*
2000	561	1496	2057	923	1134	2057	1415	642	2057
	5	*8*	*3 shells*	*6*	*8*	*2 shells*	*7*	*8*	*1 shell*
3000	923	1946	2869	1415	1454	2869	2057	812	2869
	6	*9*	*3 shells*	*7*		*2 shells*	*8*	*9*	*1 shell*
4000	1415	2456	3871	2057	1814	3871	2869	1002	3871
	7	10	3 shells	8	10	2 shells	9	10	1 shell
5000	1415	3668	5083	2869	2214	5083	3871	1212	5083
	7	11	3 shells	9	11	2 shells	10	11	1 shell

4 DFT geometries

This section provides all bulk structures as obtained from partially constrained DFT optimizations with the PBE functional (Fe atoms are kept frozen); see main manuscript for details. We present all unperturbed geometries as well as all intermediate states, obtained by atomic swapping, i.e. exchanging a Fe atom from the interface layer with an Au atom of the upper layers. All geometries are given in Cartesian format in units of Ångstrom. Supercell dimensions x, y and z were set to 8.60 Å, 8.60 Å, and 20.00 Å, respectively. The formatting supports direct copy and paste from the pdf document.

4.1 Geometries before O_2 adsorption

4.1.1 One layer

```
36


Fe 0.000000000 0.000000000 0.000000000
Fe -0.209619780 0.101432951 2.361919896
Fe 0.000000000 2.866500000 0.000000000
Fe -0.105844327 2.974581928 2.277108325
Fe 0.000000000 5.733000000 0.000000000
Fe -0.030519771 5.545744462 2.314461000
Fe 2.866500000 0.000000000 0.000000000
Fe 3.073919673 -0.196329685 2.394530491
Fe 2.866500000 2.866500000 0.000000000
Fe 2.774344217 3.082720259 2.359460247
Fe 2.866500000 5.733000000 0.000000000
Fe 2.701097942 5.654822556 2.352494753
Fe 5.733000000 0.000000000 0.000000000
Fe 5.822752013 0.169838762 2.354752559
```

```
Fe 5.733000000 2.866500000 0.000000000
Fe 5.923519407 2.901441793 2.315029530
Fe 5.733000000 5.733000000 0.000000000
Fe 6.072987286 5.410251878 2.615357976
Fe 1.559467641 1.309371747 1.245748410
Fe 1.463620532 4.305106663 0.814899541
Fe 1.386210279 7.378023501 1.276193367
Fe 4.091789161 1.484223524 1.267997204
Fe 4.377445366 4.527618265 1.283609998
Fe 4.516330933 6.957180873 1.369631302
Fe 7.162960348 1.406445056 0.813213339
Fe 7.145597723 4.322040051 0.798472199
Fe 6.947610965 7.096762938 1.272334748
Au 4.295327840 1.468850823 4.045688588
Au 7.269660189 4.210437418 4.448993639
Au 4.418441012 7.061070770 4.086585108
Au 1.447826000 1.428956970 3.983614200
Au 4.316041976 4.262905222 4.132432196
Au 1.408986960 7.179907679 4.043121653
Au -1.418700529 1.450026172 4.218735341
Au 1.430264939 4.292346244 4.215005448
Au -1.383742936 7.162664516 4.136567735
```

4.1.2 Two layers

```
45


Fe 0.000000000 0.000000000 0.000000000
Fe -0.008512726 0.011923532 2.226893151
Fe 0.000000000 2.866500000 0.000000000
```

```
Fe -0.215166069 2.629546343 2.449489936
Fe 0.000000000 5.733000000 0.000000000
Fe 0.201282796 5.942237336 2.405106411
Fe 2.866500000 0.000000000 0.000000000
Fe 2.655054423 -0.182108666 2.404845094
Fe 2.866500000 2.866500000 0.000000000
Fe 3.121981954 3.000717603 2.402209267
Fe 2.866500000 5.733000000 0.000000000
Fe 2.821596870 5.782619803 2.240022913
Fe 5.733000000 0.000000000 0.000000000
Fe 5.984813032 0.205584128 2.449850667
Fe 5.733000000 2.866500000 0.000000000
Fe 5.726448332 2.874974640 2.230155562
Fe 5.733000000 5.733000000 0.000000000
Fe 5.580783813 5.483565252 2.404679104
Fe 1.524268249 1.630404007 1.270119516
Fe 1.304343029 4.140185880 1.273937151
Fe 1.425475446 7.178759460 0.809690630
Fe 4.228476171 1.226372352 1.271124105
Fe 4.251448129 4.342775343 0.838917480
Fe 4.456986948 7.303888986 1.276850936
Fe 7.141673125 1.456253485 0.817555241
Fe 7.362191974 4.391416670 1.271405359
Fe 6.982419079 7.061100658 1.270045970
Au 4.314729878 1.404266652 4.138873768
Au 7.193923135 4.292896665 4.139095640
Au 4.329005752 7.154011982 4.101295312
Au 1.454982221 1.428306998 4.136467246
Au 4.313290393 4.282503562 4.285939520
```

```
Au 1.449878399 7.154932682 4.296964930
Au -1.414016166 1.421157132 4.348125722
Au 1.444921088 4.274761335 4.101506572
Au -1.420022135 7.145137574 4.137231203
Au 0.038004390 2.881868958 6.270742327
Au 5.739043093 2.862835075 6.318863730
Au 2.860580677 2.831404568 6.257365796
Au 2.881732825 5.707482936 6.295753229
Au 8.600949408 5.704428343 6.263541202
Au 5.759733760 5.734722567 6.257410511
Au 0.034809852 8.576796172 6.323479643
Au 2.912092117 8.592327691 6.256880040
Au 5.735489924 8.557742730 6.272877239
```

4.1.3 Three layers

```
54


Fe 0.000000000 0.000000000 0.000000000
Fe 0.041880121 -0.046382325 2.279165911
Fe 0.000000000 2.866500000 0.000000000
Fe -0.297237884 2.575290914 2.449367195
Fe 0.000000000 5.733000000 0.000000000
Fe 0.073888899 5.941865461 2.345364950
Fe 2.866500000 0.000000000 0.000000000
Fe 2.870813752 -0.036902419 2.278509739
Fe 2.866500000 2.866500000 0.000000000
Fe 3.128788627 2.793216058 2.375510836
Fe 2.866500000 5.733000000 0.000000000
Fe 2.607545077 5.880792824 2.349030592
```

```
Fe 5.733000000 0.000000000 0.000000000
Fe 5.621268344 0.334827666 2.370754161
Fe 5.733000000 2.866500000 0.000000000
Fe 5.737633407 2.886870426 2.228768703
Fe 5.733000000 5.733000000 0.000000000
Fe 5.934491749 5.468962753 2.432429062
Fe 1.441282045 1.675446696 1.292861259
Fe 1.307154202 4.139425246 1.362105360
Fe 1.445446875 7.209594995 0.833862516
Fe 4.256536664 1.439477755 0.845952125
Fe 4.219018248 4.548119950 1.294301395
Fe 4.456370800 7.045033801 1.318565585
Fe 7.144467483 1.362532667 0.883108472
Fe 7.450793520 4.300372124 1.224004829
Fe 6.902898077 7.202659348 1.339688059
Au 4.272919886 1.440416697 4.293840282
Au 7.218971708 4.224940944 4.276617851
Au 4.311270405 7.161549657 4.110342657
Au 1.429977859 1.454086896 4.151980256
Au 4.312994922 4.320129195 4.198544139
Au 1.424694041 7.218717416 4.271736466
Au -1.479478089 1.354724558 4.322373059
Au 1.443323797 4.293349061 4.126362220
Au -1.460763535 7.143963504 4.167074173
Au 0.021947589 2.843273956 6.351035741
Au 5.726109397 2.852163196 6.385632039
Au 2.849457523 2.884747369 6.331285613
Au 2.884402771 5.737343678 6.309236526
Au 8.612894048 5.714534647 6.334772902
```

```
Au 5.745344076 5.720235062 6.319870281
Au -0.002705799 8.583977219 6.364397898
Au 2.864036529 8.604241077 6.347433295
Au 5.715573364 8.549715459 6.362997362
Au -1.437937138 1.400015941 8.406958656
Au 4.274762500 1.429312644 8.392987023
Au 1.426348947 1.442503365 8.429223851
Au -1.419051707 4.280435683 8.389521494
Au 4.299049301 4.311923097 8.382935310
Au 1.448113661 4.296640462 8.407083497
Au -1.429846915 7.131019467 8.411296278
Au 1.454067452 7.156531740 8.360690938
Au 4.312673226 7.158364202 8.419753735
```

4.2 Geometries after O_2 adsorption

4.2.1 One layer

```
38


Fe 0.000000000 0.000000000 0.000000000
Fe -0.109908134 -0.281251175 2.399569282
Fe 0.000000000 2.866500000 0.000000000
Fe 0.219368053 3.113815165 2.463819847
Fe 0.000000000 5.733000000 0.000000000
Fe -0.002036562 5.721454011 2.226057140
Fe 2.866500000 0.000000000 0.000000000
Fe 2.979787020 0.162902268 2.351755556
Fe 2.866500000 2.866500000 0.000000000
Fe 2.909520866 2.783019646 2.281065196
```

```
Fe 2.866500000 5.733000000 0.000000000
Fe 2.516737423 5.660967993 2.412876654
Fe 5.733000000 0.000000000 0.000000000
Fe 5.640298701 0.119482915 2.283623208
Fe 5.733000000 2.866500000 0.000000000
Fe 5.530003325 2.701884591 2.385887960
Fe 5.733000000 5.733000000 0.000000000
Fe 6.021679781 5.781802898 2.385308890
Fe 1.191724855 1.390462212 1.290611263
Fe 1.485960307 4.264257727 0.869620678
Fe 1.535295685 7.279487424 1.059874068
Fe 4.295851757 1.428805021 0.808657036
Fe 4.293209852 4.523355753 1.334512796
Fe 4.265067398 6.960857314 1.330559580
Fe 7.348795611 1.527336403 1.286748619
Fe 7.103192272 4.061050174 1.239586424
Fe 7.094421615 7.207734547 0.882494445
Au 4.281840929 1.422977709 4.261395319
Au 7.148435513 4.237972213 4.116634052
Au 4.290028617 7.150165675 4.008116215
Au 1.416837584 1.427000266 4.088435928
Au 4.276357855 4.313201184 4.029486331
Au 1.421528473 7.211520172 4.150079429
Au -1.407907265 1.420592060 4.039898921
Au 1.416332924 4.318235760 4.324970727
Au -1.442980318 7.158236247 4.231523764
O 4.240776928 5.091229150 6.105844727
O 4.276844338 6.414763895 6.100345150
```

4.2.2 Two layers

```
47


Fe 0.000000000 0.000000000 0.000000000
Fe -0.144168923 0.237304005 2.379623187
Fe 0.000000000 2.866500000 0.000000000
Fe -0.016075003 2.856405799 2.238855783
Fe 0.000000000 5.733000000 0.000000000
Fe 0.239136119 5.480101031 2.466886674
Fe 2.866500000 0.000000000 0.000000000
Fe 2.962881816 -0.240925681 2.385375175
Fe 2.866500000 2.866500000 0.000000000
Fe 2.620841180 3.122803218 2.470675653
Fe 2.866500000 5.733000000 0.000000000
Fe 2.864040464 5.727987604 2.233982594
Fe 5.733000000 0.000000000 0.000000000
Fe 5.781142966 0.041840752 2.249098173
Fe 5.733000000 2.866500000 0.000000000
Fe 5.973354664 2.736722726 2.388946206
Fe 5.733000000 5.733000000 0.000000000
Fe 5.482264425 5.851209996 2.393595551
Fe 1.653053002 1.394750864 1.266613641
Fe 1.433722953 4.304037062 0.823369158
Fe 1.207306042 7.217469481 1.278925930
Fe 4.148230162 1.569344855 1.298988923
Fe 4.356739406 4.080279615 1.266302758
Fe 4.332927739 7.205422386 0.847534313
Fe 7.140068709 1.408228943 0.825498181
```

```
Fe 7.103887820 4.519462336 1.272813942
Fe 7.300561918 7.013489056 1.291336449
Au 4.290168569 1.433903774 4.079412449
Au 7.162764174 4.311848081 4.164221230
Au 4.287317614 7.146682494 4.256998516
Au 1.442361015 1.429927642 4.141904613
Au 4.298156983 4.283841641 4.159479220
Au 1.412989404 7.158370556 4.159551511
Au -1.430793964 1.438614040 4.274789174
Au 1.429754906 4.312044826 4.389671253
Au -1.428679252 7.149537505 4.091127830
Au -0.026546481 2.854183814 6.324704778
Au 5.704813916 2.858640879 6.261486770
Au 2.880522924 2.808298268 6.275943706
Au 2.777669106 5.719874731 6.407754360
Au 8.564245311 5.752597845 6.377875855
Au 5.795095914 5.714654703 6.251485523
Au 0.010081105 8.579756536 6.242878258
Au 2.858053694 8.607187027 6.225243370
Au 5.734666615 8.602984482 6.250062146
O 4.237996541 5.951376432 8.145668387
O 4.245447643 5.060538658 9.063678655
```

4.2.3 Three layers

```
56


Fe 0.000000000 0.000000000 0.000000000
Fe 0.047649559 -0.061893452 2.285675345
Fe 0.000000000 2.866500000 0.000000000
```

```
Fe -0.301497639 2.574123197 2.457099527
Fe 0.000000000 5.733000000 0.000000000
Fe 0.076883351 5.940760070 2.353759375
Fe 2.866500000 0.000000000 0.000000000
Fe 2.899933691 -0.005838338 2.273688751
Fe 2.866500000 2.866500000 0.000000000
Fe 3.115007049 2.806133613 2.378230084
Fe 2.866500000 5.733000000 0.000000000
Fe 2.610159100 5.886494522 2.352715213
Fe 5.733000000 0.000000000 0.000000000
Fe 5.610251843 0.333389739 2.379466442
Fe 5.733000000 2.866500000 0.000000000
Fe 5.730104325 2.877191672 2.230912528
Fe 5.733000000 5.733000000 0.000000000
Fe 5.934405750 5.492991730 2.436059383
Fe 1.437547410 1.673537789 1.286335272
Fe 1.306893365 4.133436437 1.355723920
Fe 1.445102841 7.207703101 0.836127375
Fe 4.268288887 1.443641969 0.826209477
Fe 4.226554151 4.546585592 1.291027951
Fe 4.449487526 7.044485872 1.305460297
Fe 7.158789978 1.361754985 0.886544914
Fe 7.444661947 4.302175257 1.231693080
Fe 6.907084489 7.213641879 1.337072854
Au 4.280324120 1.463391147 4.291570474
Au 7.224214797 4.236417562 4.270536896
Au 4.314763930 7.178048679 4.109447027
Au 1.429993640 1.455635755 4.142221712
Au 4.327372847 4.334857952 4.189143767
```

```
Au 1.424480532 7.230876156 4.265191740
Au -1.480865771 1.370775910 4.337408479
Au 1.447526743 4.294912800 4.124326793
Au -1.457741918 7.163532444 4.167319624
Au 0.012517666 2.876358307 6.377242026
Au 5.726024135 2.892391794 6.418312437
Au 2.842867646 2.924466750 6.307924148
Au 2.871638041 5.780333298 6.320941416
Au 8.611612937 5.756191613 6.325876453
Au 5.729638136 5.758100316 6.309097111
Au -0.005475112 8.620141237 6.393654284
Au 2.855165218 8.648822705 6.330956363
Au 5.715259644 8.593786364 6.392696451
Au -1.417187922 1.443691195 8.418468693
Au 4.286768576 1.484883702 8.479323874
Au 1.446830278 1.504673675 8.502867032
Au -1.455596014 4.355309205 8.457671093
Au 4.320681084 4.267968873 8.393720862
Au 1.353460855 4.266905162 8.401769283
Au -1.439446183 7.153184439 8.453135466
Au 1.383100945 7.331073581 8.429589494
Au 4.338505029 7.319576354 8.431723403
O 3.553049047 5.777528280 9.929085556
O 2.164948477 5.811974077 9.932412828
```

4.3 Swapped geometries, before O2 adsorption

4.3.1 One layer

```
36
```

```
Fe 0.000000000 0.000000000 0.000000000
Fe 0.270910130 -0.246821697 2.563455821
Fe 0.000000000 2.866500000 0.000000000
Fe -0.006615561 3.118352458 2.392829997
Fe 0.000000000 5.733000000 0.000000000
Fe 0.075818877 5.703477137 2.309496868
Fe 2.866500000 0.000000000 0.000000000
Fe 2.814993411 -0.103319275 2.314162065
Fe 2.866500000 2.866500000 0.000000000
Au 2.894614367 2.820242326 2.661925042
Fe 2.866500000 5.733000000 0.000000000
Fe 2.721869146 5.654807487 2.514458192
Fe 5.733000000 0.000000000 0.000000000
Fe 5.541142411 0.132090795 2.389256485
Fe 5.733000000 2.866500000 0.000000000
Fe 5.596719339 2.715760581 2.356172519
Fe 5.733000000 5.733000000 0.000000000
Fe 5.972917935 5.728330369 2.415777400
Fe 1.181832189 1.400100324 1.253821610
Fe 1.454793968 4.302402228 0.930423999
Fe 1.432070080 7.171178472 0.864692673
Fe 4.268326451 1.400969857 0.879207140
Fe 4.358542100 4.440998844 1.206612987
Fe 4.327534391 6.913232445 1.320146295
Fe 7.331478482 1.291665683 1.300279394
Fe 7.047211555 4.218720936 1.023001149
Fe 7.182186066 7.429145777 1.261086549
Au 4.389455535 1.326942867 4.402890902
```

```
Au 7.110748280 4.278360634 4.208434040
Au 4.333239950 7.124187840 4.121160176
Au 1.408394856 1.298606040 4.323365633
Fe 4.509029490 4.561646672 3.594245758
Au 1.499203128 7.059894351 4.362411969
Au -1.379171885 1.415931122 4.037934963
Au 1.316758478 4.292191469 4.391402167
Au -1.408315081 7.181710875 4.169399063
```

4.3.2 Two layers, swap in 1st layer

```
45


Fe 0.000000000 0.000000000 0.000000000
Fe 0.007534236 0.003968563 2.235219101
Fe 0.000000000 2.866500000 0.000000000
Fe -0.057542771 2.611757793 2.406677447
Fe 0.000000000 5.733000000 0.000000000
Fe 0.202506261 6.008992442 2.453772272
Fe 2.866500000 0.000000000 0.000000000
Fe 2.613700187 -0.061095968 2.406898589
Fe 2.866500000 2.866500000 0.000000000
Au 2.966991779 2.966088989 2.615205681
Fe 2.866500000 5.733000000 0.000000000
Fe 2.881459932 5.764473267 2.327322814
Fe 5.733000000 0.000000000 0.000000000
Fe 6.014625524 0.193874954 2.455512227
Fe 5.733000000 2.866500000 0.000000000
Fe 5.757088652 2.889118965 2.330373160
Fe 5.733000000 5.733000000 0.000000000
```

```
Fe 5.417909188 5.415439144 2.518339264
Fe 1.466990047 1.470074786 0.940856430
Fe 1.191101109 4.322447045 1.246356308
Fe 1.468220250 7.166793243 0.865655369
Fe 4.325392475 1.191785814 1.248037601
Fe 4.301849137 4.305652802 0.845369280
Fe 4.450522022 7.293950026 1.314061701
Fe 7.158878525 1.473652241 0.871775239
Fe 7.295777454 4.449008582 1.314090844
Fe 6.993860740 6.991354878 1.314501725
Au 4.395329721 1.388050517 4.245625678
Au 7.183254298 4.328969318 4.091365935
Au 4.334680927 7.173147390 4.093942240
Au 1.406896556 1.404731499 4.301993216
Fe 4.403997941 4.396631208 4.188805073
Au 1.466561909 7.211215121 4.326117220
Au -1.385641061 1.458706103 4.325418580
Au 1.398710344 4.397018687 4.250985946
Au -1.403166571 7.189827529 4.174380012
Au 0.004418966 2.942445158 6.301734037
Au 5.699618483 2.990878737 6.183816563
Au 2.908184792 2.906300300 6.204627244
Au 3.003559779 5.700842363 6.191201250
Au 8.609944813 5.768375358 6.340503247
Au 5.784693213 5.771444602 6.212671107
Au 0.010807318 8.605769686 6.379338801
Au 2.942919604 8.600533670 6.308857176
Au 5.770336289 8.593368829 6.336202540
```

4.3.3 Two layers, swap in 2nd layer

```
45


Fe 0.000000000 0.000000000 0.000000000
Fe 0.164226852 0.177301545 2.365617540
Fe 0.000000000 2.866500000 0.000000000
Fe 0.081920088 2.595917792 2.421747841
Fe 0.000000000 5.733000000 0.000000000
Fe -0.239752984 5.973471243 2.352755016
Fe 2.866500000 0.000000000 0.000000000
Fe 2.766430511 0.057366352 2.340363785
Fe 2.866500000 2.866500000 0.000000000
Au 2.941438217 2.696668926 2.671594257
Fe 2.866500000 5.733000000 0.000000000
Fe 3.135920135 5.710985424 2.349697226
Fe 5.733000000 0.000000000 0.000000000
Fe 5.449646566 0.478753935 2.815521604
Fe 5.733000000 2.866500000 0.000000000
Fe 5.685140696 2.919716986 2.347248686
Fe 5.733000000 5.733000000 0.000000000
Fe 5.644999188 5.610019089 2.336372662
Fe 1.445959887 1.445119221 0.840226189
Fe 1.320073054 4.408928951 1.162576280
Fe 1.468226020 6.962482794 1.240726106
Fe 4.405840665 1.341140057 0.998629771
Fe 4.302027151 4.298249180 0.853305375
Fe 4.510456469 7.386474934 1.351810560
Fe 7.019312236 1.267950199 1.271771489
```

```
Fe 7.406173378 4.241955082 1.289842575
Fe 6.911218002 7.476077470 1.446195583
Au 4.284565492 1.530856373 4.929569295
Au 7.162430666 4.383047495 4.116490623
Au 4.246309943 7.241532442 4.213653099
Au 1.368375588 1.432794237 4.608294252
Au 4.351510361 4.430705132 4.317140323
Au 1.397447207 7.185068404 4.083869429
Au -1.458800358 1.555351647 4.492483458
Au 1.348694704 4.446453513 4.034050735
Au -1.527140799 7.296904773 4.147222655
Au 0.021911895 3.372245650 6.354372818
Au 5.777806135 3.393723314 6.526164611
Au 2.772749922 3.514238355 6.447250898
Fe 1.401066058 5.835401343 6.310719557
Au 7.286635559 5.797921827 6.770389886
Au 4.290568793 5.833833811 6.873171033
Au 0.006028108 8.219485046 6.412988752
Au 2.774677831 8.133704603 6.474551941
Au 5.754267804 8.252779643 6.466406702
```

4.3.4 Three layers, swap in 1st layer

```
54


Fe 0.000000000 0.000000000 0.000000000
Fe -0.016664012 -0.012936039 2.240889637
Fe 0.000000000 2.866500000 0.000000000
Fe -0.058430084 2.571785321 2.385205267
Fe 0.000000000 5.733000000 0.000000000
```

```
Fe 0.229452024 6.004031171 2.447522619
Fe 2.866500000 0.000000000 0.000000000
Fe 2.572741279 -0.055113275 2.383952575
Fe 2.866500000 2.866500000 0.000000000
Au 2.996221218 2.995568719 2.618400878
Fe 2.866500000 5.733000000 0.000000000
Fe 2.857257900 5.792481842 2.320236476
Fe 5.733000000 0.000000000 0.000000000
Fe 6.001535885 0.230834442 2.450905101
Fe 5.733000000 2.866500000 0.000000000
Fe 5.795050795 2.849199176 2.319562837
Fe 5.733000000 5.733000000 0.000000000
Fe 5.413648401 5.411851640 2.539906668
Fe 1.474328095 1.476011842 0.954351979
Fe 1.184624134 4.322654112 1.255505389
Fe 1.478216073 7.158598050 0.870858810
Fe 4.321643739 1.182998212 1.257059712
Fe 4.313805472 4.312110920 0.858868534
Fe 4.467645912 7.284100708 1.348612706
Fe 7.160321117 1.474311339 0.866669048
Fe 7.289456476 4.462129308 1.346859535
Fe 6.984406231 6.987039799 1.372523893
Au 4.401693524 1.405539803 4.293171303
Au 7.181534982 4.314698096 4.125496305
Au 4.317891166 7.179679259 4.127407471
Au 1.428476118 1.428537034 4.312620586
Fe 4.431239855 4.430259237 4.219912333
Au 1.456673914 7.226794732 4.355721059
Au -1.373908450 1.455098623 4.357926181
```

```
Au 1.405208256 4.406619977 4.294599467
Au -1.423601359 7.174156048 4.193861136
Au 0.041027508 2.926452530 6.385945377
Au 5.750201698 2.951259997 6.311430725
Au 2.925851925 2.927931366 6.289883847
Au 2.955313103 5.754176581 6.315497339
Au 8.608191962 5.767511850 6.384804373
Au 5.763039658 5.758142365 6.281670382
Au 0.025598355 8.628774163 6.446154293
Au 2.923005713 8.639508805 6.389225889
Au 5.762650364 8.603324493 6.382832297
Au -1.429459057 1.495646420 8.384015393
Au 4.316189603 1.492289212 8.403662251
Au 1.475323793 1.490400269 8.443677398
Au -1.392899885 4.337943471 8.428591241
Au 4.352023689 4.347240654 8.380179463
Au 1.495617676 4.331262703 8.401534791
Au -1.418059361 7.175493442 8.435507963
Au 1.501556804 7.186628902 8.391951309
Au 4.345211430 7.202064809 8.435956433
```

4.3.5 Three layers, swap in 2nd layer

```
54


Fe 0.000000000 0.000000000 0.000000000
Fe 0.017788561 -0.018919922 2.239379267
Fe 0.000000000 2.866500000 0.000000000
Fe -0.011300299 2.584072292 2.385512204
Fe 0.000000000 5.733000000 0.000000000
```

```
Fe 0.293418560 5.980669802 2.518733571
Fe 2.866500000 0.000000000 0.000000000
Fe 2.544604487 -0.042102259 2.426781223
Fe 2.866500000 2.866500000 0.000000000
Au 2.897013658 2.939437752 2.592377018
Fe 2.866500000 5.733000000 0.000000000
Fe 2.849131367 5.816470764 2.297069928
Fe 5.733000000 0.000000000 0.000000000
Fe 6.047087058 0.123973893 2.409234539
Fe 5.733000000 2.866500000 0.000000000
Fe 5.798854196 2.882986002 2.284005527
Fe 5.733000000 5.733000000 0.000000000
Fe 5.475541838 5.585614519 2.389846286
Fe 1.461696769 1.449306479 0.917560297
Fe 1.185380526 4.334091339 1.237719533
Fe 1.467353232 7.153825934 0.879352658
Fe 4.322913187 1.195031240 1.273066256
Fe 4.314744876 4.301525767 0.863839466
Fe 4.351900188 7.382691036 1.340675025
Fe 7.135577091 1.486361997 0.875812653
Fe 7.305035271 4.466908517 1.359671982
Fe 7.122200831 6.921677483 1.345978196
Au 4.400170933 1.355542087 4.249617229
Au 7.182309855 4.341698004 4.137834777
Au 4.326018415 7.170120377 4.194525830
Au 1.411084912 1.384062000 4.366095968
Au 4.303010240 4.381911785 4.436104136
Au 1.521512070 7.161023316 4.444970975
Au -1.388482235 1.463917204 4.305081877
```

```
Au 1.408356897 4.388864103 4.391536762
Au -1.385754551 7.178471567 4.230238726
Au 0.011385323 2.897546952 6.415132050
Au 5.782908322 2.881933259 6.389299535
Au 2.896005221 2.883845147 6.360424032
Fe 2.868870285 5.758073206 6.541628719
Au 8.622695790 5.764700002 6.412254091
Au 5.736517384 5.788550652 6.347961175
Au 0.022550431 8.630534361 6.466326040
Au 2.952117901 8.559553298 6.389737341
Au 5.792466661 8.619696527 6.399404496
Au -1.401073625 1.486405344 8.452253538
Au 4.322499478 1.451464660 8.443969491
Au 1.516510241 1.453895039 8.458306576
Au -1.425133793 4.357674894 8.449984403
Au 4.290913540 4.350630907 8.330312228
Au 1.485451658 4.330024458 8.390148338
Au -1.409669514 7.174995335 8.462919165
Au 1.518870969 7.148690302 8.398032229
Au 4.325974329 7.153940577 8.410104704
```

4.3.6 Three layers, swap in 3rd layer

```
54


Fe 0.000000000 0.000000000 0.000000000
Fe -0.014822356 0.025475329 2.251291483
Fe 0.000000000 2.866500000 0.000000000
Fe -0.033653906 2.500106693 2.466055619
Fe 0.000000000 5.733000000 0.000000000
```

```
Fe 0.137740861 6.025823281 2.403860087
Fe 2.866500000 0.000000000 0.000000000
Fe 2.601516707 -0.044948455 2.392919709
Fe 2.866500000 2.866500000 0.000000000
Au 2.915720243 2.790626459 2.630708227
Fe 2.866500000 5.733000000 0.000000000
Fe 2.822827279 5.824911881 2.284328652
Fe 5.733000000 0.000000000 0.000000000
Fe 5.971163860 0.301778241 2.524417019
Fe 5.733000000 2.866500000 0.000000000
Fe 5.801576962 2.846233738 2.288290142
Fe 5.733000000 5.733000000 0.000000000
Fe 5.622773997 5.475616100 2.346377060
Fe 1.452320489 1.468685076 0.920949839
Fe 1.213048669 4.293083586 1.281939799
Fe 1.465823574 7.147498586 0.863275088
Fe 4.339486323 1.184849888 1.216069988
Fe 4.270570781 4.310308528 0.886774245
Fe 4.462769532 7.297495638 1.339343913
Fe 7.147705007 1.477593976 0.886030301
Fe 7.403363258 4.323439711 1.339072316
Fe 6.932433403 7.137733789 1.337597964
Au 4.375865524 1.312441046 4.462109699
Au 7.180857570 4.312773517 4.140368847
Au 4.333473368 7.194312307 4.089487586
Au 1.390128214 1.352951936 4.479353797
Au 4.352745688 4.357617413 4.304265319
Au 1.440760742 7.240341859 4.323784142
Au -1.403861843 1.409044290 4.489180292
```

```
Au 1.357614926 4.407448256 4.203454043
Au -1.431631234 7.206677402 4.194385941
Au 0.012685303 3.036106743 6.362371925
Au 5.776467176 3.037822765 6.372805859
Au 2.879193351 2.988874637 6.292108891
Au 2.902122692 5.839992671 6.269631691
Au 8.585682677 5.867026777 6.320450428
Au 5.769308608 5.897537750 6.280629446
Au 0.034002290 8.729882153 6.926015831
Au 2.895775681 8.704312368 6.750368659
Au 5.783156394 8.725589210 6.813551911
Au -1.417591308 2.001336576 8.606666051
Au 4.295008536 2.020030038 8.567679549
Au 1.511354962 2.093264743 8.600914948
Au 0.050706240 4.443618917 8.952455202
Au 5.641372000 4.464272048 8.912753273
Fe 2.883357600 4.446220455 8.474087774
Au -1.423743989 6.877456209 8.575925603
Au 1.507224329 6.788066227 8.548468514
Au 4.298892380 6.879208090 8.532005983
```

4.4 Swapped geometries, after O2 adsorption

4.4.1 One layer

```
38


Fe 0.000000000 0.000000000 0.000000000
Fe 0.180072115 0.014303273 2.329401694
Fe 0.000000000 2.866500000 0.000000000
```

```
Fe 0.200357082 2.478333678 2.585237419
Fe 0.000000000 5.733000000 0.000000000
Fe 0.070554499 5.859389114 2.368470929
Fe 2.866500000 0.000000000 0.000000000
Fe 2.788138402 -0.033696513 2.278027377
Fe 2.866500000 2.866500000 0.000000000
Au 2.913454338 2.759519788 2.674883255
Fe 2.866500000 5.733000000 0.000000000
Fe 2.752238232 5.664886227 2.410688458
Fe 5.733000000 0.000000000 0.000000000
Fe 5.505237275 0.267996972 2.393497230
Fe 5.733000000 2.866500000 0.000000000
Fe 5.547344483 2.778008160 2.389245435
Fe 5.733000000 5.733000000 0.000000000
Fe 5.966749907 5.481783413 2.373945317
Fe 1.433418617 1.475579445 0.865218905
Fe 1.249457730 4.254142747 1.204132729
Fe 1.428296446 7.129982315 0.846780929
Fe 4.298380222 1.409484132 0.815193421
Fe 4.312586974 4.444009952 1.096520853
Fe 4.447244011 7.028281526 1.299034496
Fe 7.198870397 1.585406906 1.210091058
Fe 7.406359245 4.105149962 1.347094426
Fe 6.971623544 7.282593688 1.334178311
Au 4.371343423 1.326161611 4.471344821
Au 7.206225291 4.099363403 4.106424701
Au 4.330835385 7.150659787 4.013838862
Au 1.432801843 1.270284643 4.496140250
Fe 4.442843305 4.542002988 3.752856577
```

```
Au 1.437217760 7.136005274 4.200108499
Au -1.442417946 1.295505039 4.165922634
Au 1.321255734 4.342074242 4.240513054
Au -1.432535577 7.135747080 4.067391810
O 4.430002190 4.761503913 5.504418030
O 4.416820537 6.042980314 5.931659976
```

4.4.2 Two layers, swap in 1st layer

```
47


Fe 0.000000000 0.000000000 0.000000000
Fe -0.250436504 0.270268721 2.456339110
Fe 0.000000000 2.866500000 0.000000000
Fe -0.096051646 2.830052305 2.268756514
Fe 0.000000000 5.733000000 0.000000000
Fe 0.243725486 5.488582651 2.405922350
Fe 2.866500000 0.000000000 0.000000000
Fe 3.107921425 -0.080508555 2.382134171
Fe 2.866500000 2.866500000 0.000000000
Au 2.811643198 2.927787100 2.615618448
Fe 2.866500000 5.733000000 0.000000000
Fe 2.928795165 5.766765439 2.319808356
Fe 5.733000000 0.000000000 0.000000000
Fe 5.714036245 0.037180029 2.272691752
Fe 5.733000000 2.866500000 0.000000000
Fe 5.772518058 2.722053753 2.476980694
Fe 5.733000000 5.733000000 0.000000000
Fe 5.552391366 5.997419599 2.474771919
Fe 1.429609270 1.210750765 1.227208969
```

```
Fe 1.429547602 4.293453485 0.851879617
Fe 1.278241305 7.306010702 1.285949509
Fe 4.290556104 1.465628528 0.958632873
Fe 4.532532781 4.315991012 1.292444690
Fe 4.276296323 7.140133968 0.864921078
Fe 7.152125032 1.449385273 0.842176773
Fe 6.996143033 4.465468969 1.325516006
Fe 7.362509452 7.078477018 1.309563239
Au 4.334401974 1.385499282 4.300420132
Au 7.211859144 4.340079068 4.134559571
Au 4.215280972 7.138298717 4.309892106
Au 1.343847272 1.412481531 4.288355980
Fe 4.555012531 4.406434676 3.790137635
Au 1.389962104 7.212806510 4.120491493
Au -1.456696703 1.476031867 4.345461116
Au 1.495563124 4.433414379 4.409698883
Au -1.434508987 7.200934260 4.171917561
Au 0.025227237 2.934029560 6.337202563
Au 5.744494609 2.892794593 6.269664610
Au 2.960897666 2.937514676 6.221463732
Au 2.749356845 5.760250670 6.484890306
Au 8.506768145 5.801484762 6.374254319
Au 5.671497751 5.634818610 6.120530695
Au -0.027061482 8.598877935 6.369105394
Au 2.810393944 8.638279420 6.287023412
Au 5.743787964 8.559845982 6.343786103
O 4.193967544 6.326491757 8.146816139
O 4.177316976 5.706110224 9.256117359
```

4.4.3 Two layers, swap in 2nd layer

```
47


Fe 0.000000000 0.000000000 0.000000000
Fe -0.275582106 0.227257244 2.452178880
Fe 0.000000000 2.866500000 0.000000000
Fe -0.085793841 2.818160058 2.270821355
Fe 0.000000000 5.733000000 0.000000000
Fe 0.268151336 5.516606044 2.428317662
Fe 2.866500000 0.000000000 0.000000000
Fe 3.155567237 -0.103137679 2.424776065
Fe 2.866500000 2.866500000 0.000000000
Au 2.813463275 2.932148849 2.622341668
Fe 2.866500000 5.733000000 0.000000000
Fe 2.882924107 5.793355907 2.288089226
Fe 5.733000000 0.000000000 0.000000000
Fe 5.726386942 0.023075326 2.239694304
Fe 5.733000000 2.866500000 0.000000000
Fe 5.797185756 2.602634847 2.412247722
Fe 5.733000000 5.733000000 0.000000000
Fe 5.519918317 6.006759143 2.482076303
Fe 1.434718894 1.196772095 1.263425676
Fe 1.433982392 4.291909734 0.852794318
Fe 1.304266548 7.330074140 1.304835840
Fe 4.264889372 1.452149704 0.936566832
Fe 4.551265791 4.316994525 1.265932543
Fe 4.266250176 7.133142558 0.848566925
Fe 7.178875936 1.471613463 0.836216639
```

```
Fe 7.036923596 4.456550347 1.325458885
Fe 7.307272674 6.999481283 1.326731841
Au 4.313808189 1.365789019 4.341252225
Au 7.182850397 4.348673244 4.119997617
Au 4.258606282 7.156150892 4.400506880
Au 1.320569429 1.397577167 4.287776553
Au 4.382962425 4.381277729 4.320727377
Au 1.408967351 7.216200718 4.116632284
Au -1.489787611 1.472035918 4.366376012
Au 1.478308245 4.425317053 4.457780139
Au -1.446684089 7.203865991 4.186312568
Au -0.079897410 3.007626131 6.351489664
Au 5.690046768 2.923346935 6.369296848
Au 2.814616696 2.837063065 6.313799581
Fe 3.157641301 5.616361143 6.513128597
Au 8.650995911 5.923145048 6.284800893
Au 5.839065812 5.790508775 6.367247262
Au -0.102747258 8.702762236 6.434886304
Au 2.715560388 8.482256331 6.315110829
Au 5.679545269 8.616680036 6.452704410
O 3.133267368 5.625911765 8.143238075
O 3.525984998 5.543177591 9.333845033
```

4.4.4 Three layers, swap in 1st layer

```
56


Fe 0.000000000 0.000000000 0.000000000
Fe 0.017195106 -0.017330069 2.235142292
Fe 0.000000000 2.866500000 0.000000000
```

```
Fe -0.027695702 2.587469430 2.386212094
Fe 0.000000000 5.733000000 0.000000000
Fe 0.255109624 6.000901814 2.463055201
Fe 2.866500000 0.000000000 0.000000000
Fe 2.599724215 -0.018472837 2.390257434
Fe 2.866500000 2.866500000 0.000000000
Au 2.959018261 2.970280748 2.602959007
Fe 2.866500000 5.733000000 0.000000000
Fe 2.869877534 5.778979964 2.320277288
Fe 5.733000000 0.000000000 0.000000000
Fe 6.048393838 0.186913392 2.450965937
Fe 5.733000000 2.866500000 0.000000000
Fe 5.735813640 2.934018207 2.346859361
Fe 5.733000000 5.733000000 0.000000000
Fe 5.432502358 5.437780894 2.535269129
Fe 1.450929631 1.465084696 0.917164242
Fe 1.184946762 4.323505438 1.243380719
Fe 1.491373149 7.158653448 0.873701564
Fe 4.350644480 1.191848297 1.246353276
Fe 4.312639456 4.322158655 0.860501304
Fe 4.453940916 7.313790851 1.355172667
Fe 7.134160600 1.492057642 0.902633792
Fe 7.303296668 4.458964767 1.348139523
Fe 7.011662122 6.965880278 1.350034981
Au 4.438583531 1.406850236 4.254619264
Au 7.206155101 4.303531972 4.118714755
Au 4.326990977 7.172926176 4.131164537
Au 1.433509692 1.426134998 4.328389419
Fe 4.469468246 4.385607987 4.188729920
```

```
Au 1.470656661 7.230633336 4.354553204
Au -1.350498058 1.446842143 4.349143468
Au 1.423848197 4.408927150 4.305158938
Au -1.401056734 7.160358446 4.192063753
Au 0.074324585 2.911227182 6.417676722
Au 5.793254732 2.924331059 6.337862932
Au 2.975842795 2.915656663 6.260318839
Au 2.989649842 5.739367017 6.315982726
Au 8.650639412 5.754245558 6.395606154
Au 5.781610050 5.730612457 6.255149505
Au 0.072731378 8.619742689 6.478293850
Au 2.977268833 8.637774411 6.359429602
Au 5.816362526 8.597659582 6.392820439
Au -1.381342804 1.485145230 8.402917984
Au 4.373439660 1.451776420 8.486347321
Au 1.546265560 1.457514542 8.512681253
Au -1.352700289 4.347435853 8.485109620
Au 4.450709436 4.215519739 8.404336264
Au 1.485898806 4.209308479 8.420191547
Au -1.345125963 7.136503485 8.476170160
Au 1.502089905 7.281087210 8.446830028
Au 4.462618689 7.275915861 8.417095744
O 3.680426417 5.716905766 9.914222515
O 2.277612232 5.745044322 9.905728622
```

4.4.5 Three layers, swap in 2nd layer

```
56


Fe 0.000000000 0.000000000 0.000000000
```

```
Fe 0.038008684 -0.008872816 2.263327700
Fe 0.000000000 2.866500000 0.000000000
Fe 0.027076775 2.612828840 2.387676698
Fe 0.000000000 5.733000000 0.000000000
Fe 0.347467098 5.998132480 2.554996685
Fe 2.866500000 0.000000000 0.000000000
Fe 2.586771896 0.038734339 2.410435874
Fe 2.866500000 2.866500000 0.000000000
Au 2.887784822 2.930988802 2.585182525
Fe 2.866500000 5.733000000 0.000000000
Fe 2.845486220 5.826842054 2.288449333
Fe 5.733000000 0.000000000 0.000000000
Fe 6.059002228 -0.115062281 2.448326230
Fe 5.733000000 2.866500000 0.000000000
Fe 5.717835207 3.085179877 2.356910531
Fe 5.733000000 5.733000000 0.000000000
Fe 5.527127973 5.660476405 2.370179059
Fe 1.426043164 1.454469002 0.894217479
Fe 1.191644713 4.338026185 1.218859654
Fe 1.449109883 7.190436035 0.860395789
Fe 4.438908568 1.262066788 1.255328547
Fe 4.303504233 4.334630067 0.866867011
Fe 4.326125171 7.435739820 1.338783116
Fe 6.981062817 1.500108576 1.131099473
Fe 7.333849853 4.457941097 1.366571205
Fe 7.214839260 6.886191490 1.301431261
Au 4.421247409 1.365477068 4.239699167
Au 7.244426096 4.338802726 4.148405560
Au 4.343463097 7.190141573 4.208652020
```

```
Au 1.415589303 1.415665487 4.386190360
Au 4.340641180 4.414366652 4.414902617
Au 1.563977583 7.211046928 4.433491571
Au -1.391094222 1.451370159 4.255876276
Au 1.471695088 4.430451053 4.412010170
Au -1.318947148 7.163619111 4.311833574
Au 0.044319381 2.910031347 6.407739554
Au 5.805454305 2.888732904 6.362337869
Au 2.936070718 2.879713329 6.361852466
Fe 2.909374282 5.829672824 6.462150063
Au 8.673169591 5.772431313 6.452956074
Au 5.779577183 5.791471130 6.375888602
Au 0.053440061 8.643191296 6.497644965
Au 2.985723022 8.566290397 6.412652076
Au 5.822302285 8.627696778 6.424265803
Au -1.351499156 1.504614896 8.524137135
Au 4.444212117 1.343036186 8.476665429
Au 1.481254456 1.350468482 8.487861072
Au -1.381640035 4.322339643 8.472589355
Au 4.337589014 4.394211585 8.302337629
Au 1.542344832 4.394343861 8.370112361
Au -1.380973539 7.177131430 8.469244044
Au 1.543356297 7.151535340 8.500351506
Au 4.348660368 7.145819038 8.478729708
O 3.648435077 2.749136397 10.037728021
O 2.274856006 2.733111268 10.034982738
```

4.4.6 Three layers, swap in 3rd layer

```
56
```

```
Fe 0.000000000 0.000000000 0.000000000
Fe 0.016354463 0.007024135 2.234328622
Fe 0.000000000 2.866500000 0.000000000
Fe -0.048077286 2.562296913 2.413114136
Fe 0.000000000 5.733000000 0.000000000
Fe 0.255829115 6.040245129 2.482723142
Fe 2.866500000 0.000000000 0.000000000
Fe 2.559808968 -0.006124697 2.418210925
Fe 2.866500000 2.866500000 0.000000000
Au 2.887866524 2.853835336 2.599633400
Fe 2.866500000 5.733000000 0.000000000
Fe 2.846129659 5.783042349 2.278415060
Fe 5.733000000 0.000000000 0.000000000
Fe 6.034921967 0.165420598 2.422574169
Fe 5.733000000 2.866500000 0.000000000
Fe 5.806783977 2.850957102 2.288598640
Fe 5.733000000 5.733000000 0.000000000
Fe 5.470936119 5.557267413 2.371311940
Fe 1.439754900 1.451654901 0.905425343
Fe 1.171552359 4.318941222 1.295758373
Fe 1.486314365 7.157939952 0.875697967
Fe 4.328547883 1.187190432 1.257279586
Fe 4.289529723 4.291790967 0.860445998
Fe 4.368812035 7.366573832 1.325054928
Fe 7.135533374 1.496116520 0.880602534
Fe 7.301665008 4.465911451 1.346601357
Fe 7.082012187 6.956598530 1.326941706
Au 4.380400182 1.322202681 4.315822722
```

```
Au 7.164101371 4.340960188 4.109191523
Au 4.324872790 7.180543548 4.135655008
Au 1.388155026 1.395313302 4.435631365
Au 4.323925833 4.337082038 4.356929110
Au 1.476283208 7.252655054 4.406278234
Au -1.399940930 1.432650604 4.373680743
Au 1.374100732 4.407995431 4.274103228
Au -1.414925107 7.204319639 4.214301398
Au 0.006611298 2.969823742 6.337073160
Au 5.768112751 2.937927569 6.358109484
Au 2.907481195 2.951847231 6.398510236
Au 2.915427889 5.733958219 6.428689972
Au 8.578818803 5.816581152 6.316595935
Au 5.759687423 5.788599559 6.323798615
Au 0.025906284 8.678774090 6.875350280
Au 2.844406676 8.650608429 6.539654967
Au 5.813362085 8.630698035 6.530529075
Au -1.477048004 1.885822350 8.553188940
Au 4.286639176 1.584733977 8.458816484
Au 1.448964862 1.987128415 8.590115677
Au -0.175340827 4.377577271 8.840865088
Au 5.338104663 4.368859304 8.731226590
Fe 2.552553194 4.370570407 8.793544100
Au -1.503200671 6.855238484 8.539196713
Au 1.419903521 6.766225948 8.558774617
Au 4.270199851 7.148861423 8.457434688
O 4.349226150 4.400415672 10.731617680
O 3.056505607 4.430231073 10.411410671
```

Supporting Information: Vanadium(V) oxide clusters synthesized by sublimation from bulk at fully inert conditions

Maximilian Lasserus, Martin Schnedlitz, Roman Messner, Florian Lackner, Wolfgang E. Ernst,* and Andreas W. Hauser*

Institute of Experimental Physics, Graz University of Technology, Petersgasse 16, A-8010 Graz, Austria. Fax: +43 (316) 873-108140; Tel: +43 (316) 873-8157; +43 (316) 873-8140;

E-mail: wolfgang.ernst@tugraz.at; andreas.w.hauser@gmail.com

In the first section of this Supporting Information we present details of the mass spectrum shown in the main article, ranging from 320 amu to 400 amu. Section S2 discusses the change in the He droplet distribution due to different nozzle temperatures. Mass spectra with all peaks assigned to molecular structures are provided in Section S3. In Section S4, additional DFT results are presented for the charged $(V_2O_5)_n^+$ structures. Section S5 compares the ionization energies of the neutral clusters. The remaining sections S6 and S7 contain the minimum energy geometries in cartesian coordinates as obtained at the ωB97X-V (gas phase) or PBE (bulk) level of theory.

Contents

S1 Details of the mass spectra

In Figure S1 we show a detail of the mass spectra presented in Figure 2 of the main article, zooming into the area between 320 amu and 400 amu. Several peaks appear in close proximity to the signals assigned to the $(V_2O_5)_n$ clusters, which can be attributed to the adsorption of water molecules. For the $(V_2O_5)_2$ signal, an additional peak is visible which corresponds to a fragment lacking a single O atom. The regular sequence of unlabeled peaks with a spacing of 4 amu represents the He_N cluster distribution.

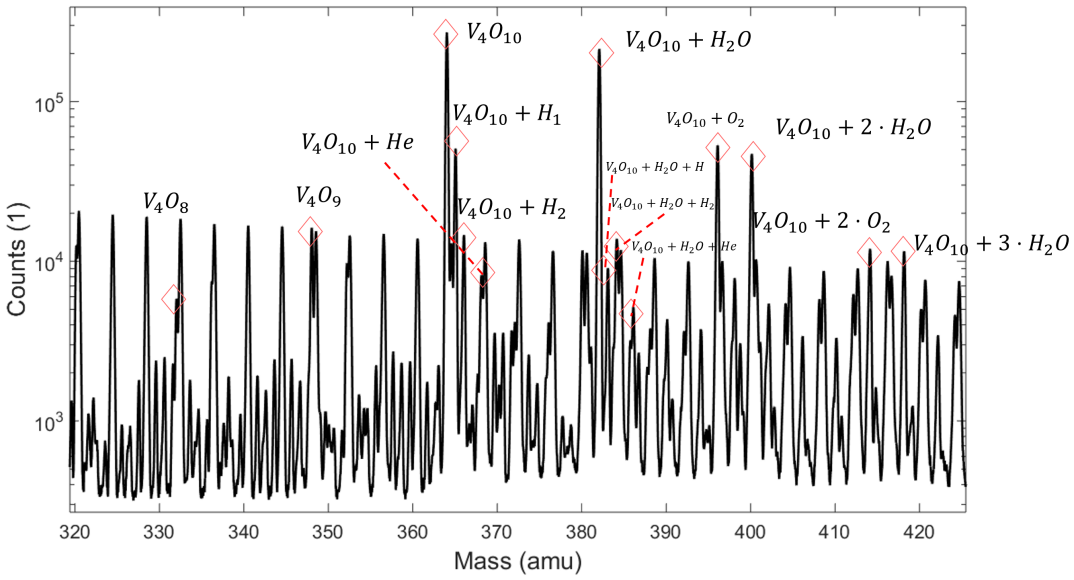

Figure S1: Magnified section of the mass spectra in Figure 2 of the main article. All peaks in direct neighborhood of the $(V_2O_5)_2$ signal have been assigned to various contaminants.

S2 Droplet size distribution

In the main manuscript the variation of the nozzle temperature was mentioned as a handle to control the He droplet size distribution. Figure S2 shows mass spectra as a function of the nozzle temperature. At lower nozzle temperatures the He droplets increase in size and are able to collect larger amounts of $(V_2O_5)_2$ units. This in turn enables the synthesis of larger vanadium oxide structures inside the droplets, and the characteristic pattern of $(V_2O_5)_n$ peaks in the mass spectra is continued towards higher masses. At 14 K only dimers are present, while larger oligomers start to appear at lower temperatures due to the increasing pickup cross section for the larger He droplets.

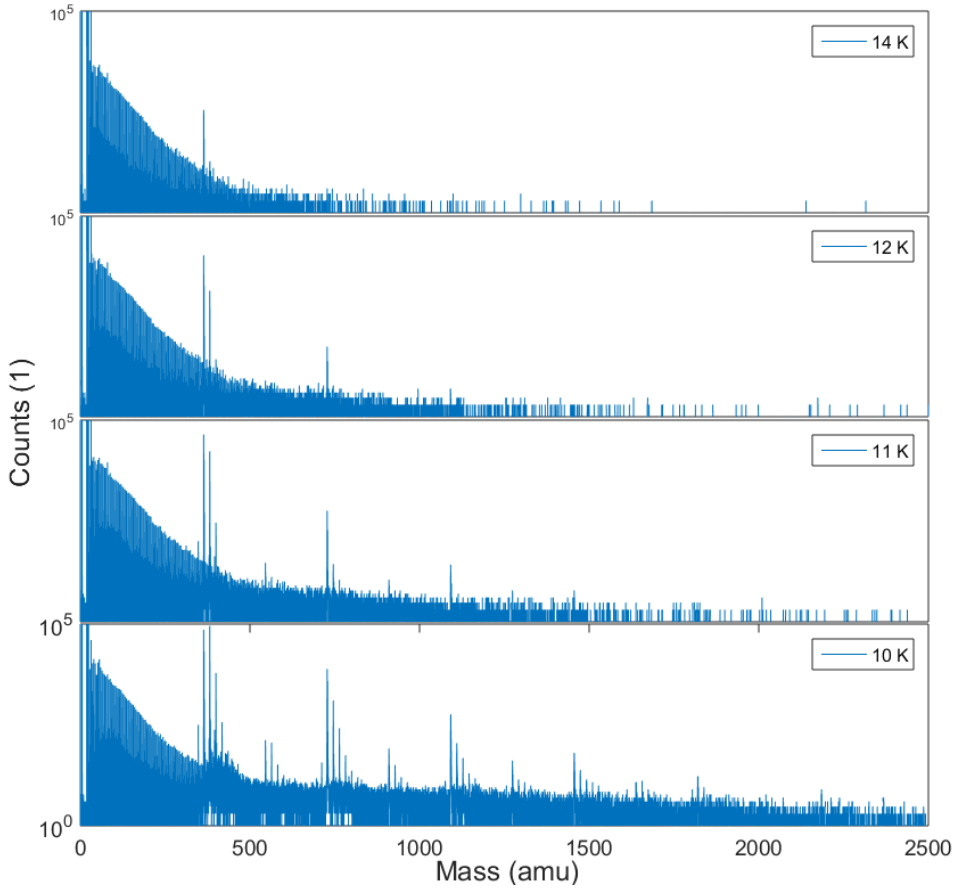

Figure S2: Mass spectra obtained for different nozzle temperatures. The temperature of the V_2O_5 crucible was kept constant during measurements.

S3 Fully assigned mass spectra

In Figure 1b of the main article several smaller peaks remained unassigned to avoid cluttering. A full assignment of the corresponding region is provided in Figure S3, where all peaks related to vanadium oxide structures are labelled and marked by red diamonds.

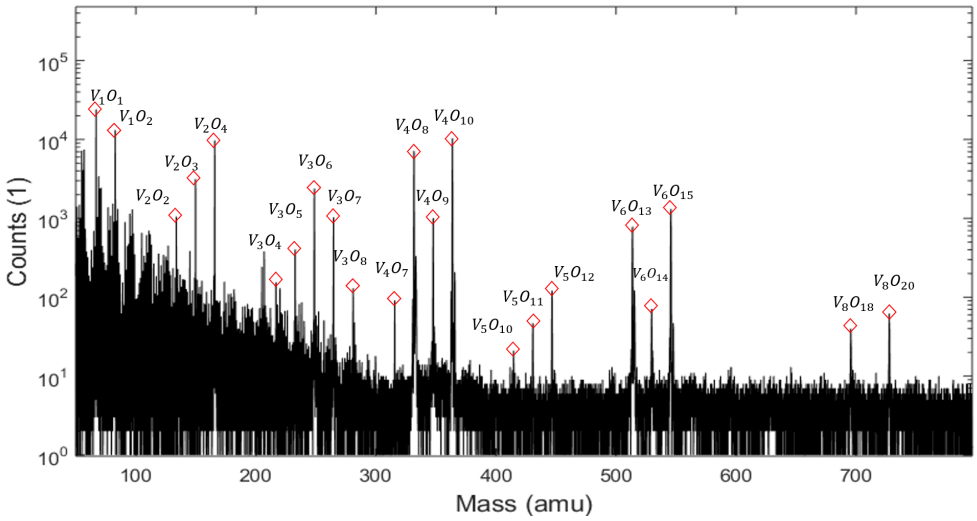

Figure S3: Same mass spectra as shown in Figure 1b of the main text for 89 eV, but with all peaks related to vanadium oxide marked by red diamonds.

S4 Minimum energy comparison of the cationic species

The same DFT procedure as described in the main article has been applied to the $(V_2O_5)_n^+$ cationic cluster species. In Figure S4 a monotonic increase of binding energy per unit can be observed, without any hint of oscillation with the number n of building units.

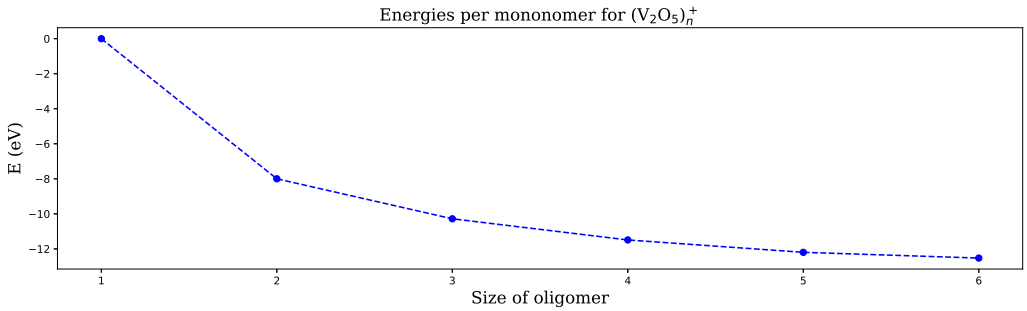

Figure S4: Electronic energy of cationic $(V_2O_5)_n^+$ clusters per building unit, plotted as a function of oligomer size n.

S5 Ionization energies

The ionization energies of the neutral clusters, obtained with the ωB97X-V functional, are plotted in Figure S5. Energies are calculated by taking the difference between electronic states containing $N-1$ and N electrons, evaluated at the minimum energy geometries of the neutral species. The stabilization of the electronic structure when going from the monomer to the dimer is significant. It is related to bond saturation and explains the large drop of binding energy per unit as shown in Figure 3 of the main manuscript.

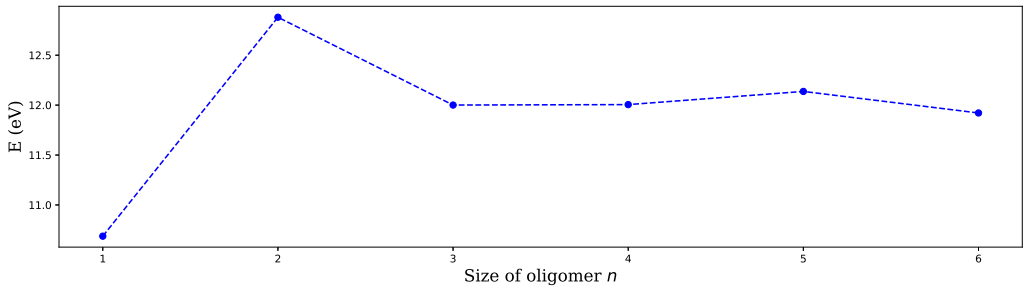

Figure S5: Ionization energies of the neutral $(V_2O_5)_n$ clusters, plotted as a function of oligomer size n.

S6 Geometries of the gas-phase species $(V_2O_5)_n$

This section provides the geometries of all neutral oligomeres up to $n = 6$ as obtained from fully unconstrained DFT optimizations with the ωB97X-V functional. The structures are given in Cartesian coordinates in units of Ångstrom. The formatting supports direct copy and paste from the pdf document.

S6.1 Monomer

```
7
1.out
V -1.98355 0.78849 0.65549
O -0.63894 0.87368 -0.16184
O -2.42118 2.19665 1.20104
O -3.37213 -0.33740 -0.17273
O -4.51815 -1.95738 1.69715
O -2.08721 -0.73773 1.89695
V -3.19712 -1.56570 0.95346
```

S6.2 Dimer

```
14
2.out
V -2.05392 0.72991 0.68844
V 0.27960 -0.59813 -1.01994
O -0.53989 0.77564 -0.24302
O -2.51168 2.10673 1.23949
O -3.33547 -0.19256 -0.13569
O 1.59105 -0.22800 -1.76283
O 0.42230 -2.00806 0.05929
```

```
O -2.37345 -2.97604 0.16796
O -4.50534 -1.97209 1.68623
O -0.40260 -4.30683 -1.31606
O -2.07857 -0.58489 1.88999
O -0.83597 -1.61496 -1.96539
V -3.19342 -1.60212 0.94409
V -0.85990 -2.93015 -0.76427
```

S6.3 Trimer

```
21
3.out
V 0.21497 -0.23427 -1.47505
O -1.02193 0.58878 -0.50763
O 0.52144 0.55729 -2.76928
O 0.42392 -3.81520 0.10489
O -2.25032 -2.87359 0.04351
O -1.24667 -4.42516 -1.97688
O -0.34534 -1.86126 -1.87739
V -0.87146 -3.29519 -0.98804
O 1.65462 -0.34721 -0.44626
V 0.72895 -3.41957 1.80600
V 1.81546 -0.35639 1.31920
V -2.31019 -2.35173 1.73694
V -1.22387 0.71004 1.24956
O 1.34984 -4.62580 2.55100
O 1.81282 -2.02678 1.89687
O -3.57832 -2.89530 2.43822
O 3.11717 0.35590 1.75928
O -2.28954 -0.58584 1.80473
```

```
O -1.81097 2.08656 1.64449
O -0.84247 -2.98598 2.50311
O 0.38859 0.48492 1.95149
```

S6.4 Tetramer

```
28
4.out
V -2.16635 0.99394 0.32600
V 0.39620 -0.12201 -1.46611
O -1.14154 0.66318 -1.07520
O -2.60731 2.47773 0.34987
O -3.58328 -0.06548 0.41300
O 0.96086 0.47799 -2.77510
O 0.04925 -4.22792 0.07977
O -2.05903 -2.38260 0.01033
O -4.76681 -2.51969 0.42461
O -1.51087 -3.99238 -2.14156
O -1.20075 0.57806 1.74114
O 0.13549 -1.86011 -1.67996
V -3.48016 -1.77671 0.85944
V -0.85324 -3.16347 -1.01154
O -3.16047 -2.02450 2.57971
O 1.55033 0.14742 -0.15078
V 0.54688 -3.73532 1.70690
V 1.98069 -0.54610 1.41682
V -1.82331 -2.46824 3.65195
V -0.31362 0.46240 3.26006
O 1.67041 -4.66523 2.22610
O 1.10751 -2.07382 1.52442
```

```
O -2.39126 -3.06750 4.95984
O 3.51098 -0.75236 1.52744
O -0.86488 -1.02890 4.03185
O -0.57741 1.68551 4.17160
O -0.79688 -3.66916 2.85271
O 1.39291 0.41047 2.78712
```

S6.5 Pentamer

```
35
5.out
V 0.85129 -0.44827 -2.07493
O 2.03293 -0.14461 -3.02634
O -0.12971 -3.92028 0.27099
O -0.37366 -4.67934 -2.32893
O 0.66050 -2.19985 -1.92994
V -0.46403 -3.44880 -1.39380
O 1.20114 0.21329 -0.47231
V 0.12084 -3.22620 1.87845
V 0.79307 -0.01503 1.22680
V -2.97571 -2.08120 2.81642
V -2.15678 0.96934 2.56969
O 0.96540 -4.20041 2.73362
O 0.99846 -1.70172 1.70110
O -3.93230 -2.86578 3.74571
O 1.67094 0.89721 2.11796
O -2.75461 -0.44734 3.45176
O -1.56162 1.98880 3.57070
O -1.42900 -2.91750 2.65853
O -0.92028 0.35487 1.46861
```

```
O -2.76101 1.72552 -3.58135
O -4.82826 2.65620 -0.55484
V -2.38484 0.50096 -2.71343
O -0.63781 0.24733 -2.71090
V -4.18510 1.37679 0.03252
O -2.94779 0.72846 -1.05028
O -3.42647 1.71682 1.59416
O -3.23463 -0.92553 -3.31687
O -5.41511 0.11352 0.18047
V -3.52505 -2.44632 -2.45355
V -5.16915 -1.63693 0.25963
O -4.89944 -2.31991 -1.34992
O -2.07662 -2.72620 -1.48308
O -3.70149 -1.88063 1.21391
O -3.74552 -3.58716 -3.47592
O -6.39342 -2.29876 0.93673
```

S6.6 Hexamer

```
42
6.out
V 0.90449 -0.48967 -2.00621
O -2.14110 2.05098 2.86309
O 1.74778 -0.02344 -3.21768
O -0.00077 -4.08431 0.08290
O -3.80106 -2.07983 3.45222
O -0.14084 -4.75020 -2.54796
O 0.77121 -2.25127 -2.01673
V -0.32604 -3.56260 -1.57256
O 1.65801 0.04885 -0.50273
```

```
V 0.28008 -3.34541 1.66200
V 1.51858 -0.27483 1.22768
V -2.05838 -2.11199 3.73552
V -0.82392 0.96046 3.30367
O 0.82945 -4.40187 2.65112
O 1.43440 -2.01697 1.50833
O -1.73179 -3.05117 4.92187
O 2.73785 0.31536 1.97681
O -1.47442 -0.48242 4.08839
O 0.15867 1.67673 4.26163
O -1.22441 -2.64804 2.27267
O 0.01505 0.41632 1.84696
O -1.49837 1.09007 -4.55826
O -4.50756 3.27493 2.32815
O -5.19069 3.03590 -1.29141
V -2.05698 0.52483 -3.22985
V -3.73126 1.95505 2.10137
O -0.73994 0.14834 -2.11353
V -4.35435 1.73686 -1.19546
O -3.15306 1.69444 -2.48905
O -3.54897 1.63158 0.37377
O -2.91221 -0.98943 -3.54082
O -4.64417 0.60400 2.78123
O -5.41989 0.33307 -1.31705
V -3.29012 -2.54631 -2.79631
V -4.96501 -1.11618 2.53830
V -5.58625 -1.33474 -0.75869
O -4.80837 -2.43344 -1.90148
O -1.96681 -2.91649 -1.68554
```

```
O -4.77844 -1.43207 0.80989
O -3.40061 -3.63433 -3.89186
O -6.40507 -1.44777 2.99922
O -7.08644 -1.69009 -0.61996
```

S7 Bulk structures

This section provides the bulk structures as obtained from fully unconstrained DFT optimizations with the PBE functional; see main manuscript for details. We present the undisturbed structure, the structure with one unit removed, and the structure with two units removed. All geometries are given in Cartesian format in units of Ångstrom. Supercell dimensions x, y and z were set to 22.741 Å, 10 Å, and 10.710 Å, respectively. The formatting supports direct copy and paste from the pdf document.

S7.1 Unperturbed plane

```
84


V 0.236201593 2.983430440 2.064976999
V 0.236083242 2.981816470 5.634878377
V 0.236395637 2.981891099 9.204135055
V 2.413247001 1.626961493 0.280567361
V 2.413385231 1.626306315 3.849796577
V 2.413362822 1.625146837 7.419837347
V 5.895491534 1.591168989 0.280257560
V 5.895450629 1.590298672 3.849648302
V 5.895364431 1.589304583 7.419742232
V 8.073364076 2.936400426 2.064915898
V 8.073508938 2.934748366 5.634828035
V 8.073227632 2.935180518 9.204028853
O 9.820918958 2.537922370 2.065758908
O 9.821032425 2.536403058 5.634142654
O 9.820952403 2.537282380 9.203364317
O 4.158773569 2.038586132 0.281133483
```

```
O 4.158851396 2.037884239 3.850428068
O 4.158769084 2.037155127 7.418542400
O 0.354565999 4.558781200 2.065081364
O 0.354330888 4.557178119 5.635952557
O 0.355133510 4.557198784 9.202172527
O 2.296907674 0.051339222 0.282202758
O 2.297007644 0.050716190 3.848523244
O 2.297289182 0.049519705 7.420031125
O 5.986759061 0.013660518 0.281302083
O 5.986471857 0.012703977 3.848150114
O 5.986214044 0.011766184 7.419973758
O 7.946913560 4.511244157 2.065012078
O 7.947020504 4.509620538 5.635656478
O 7.946395056 4.509945293 9.201865020
O 0.548512236 2.434353211 0.279883504
O 0.549102347 2.434103485 3.849858699
O 0.548729288 2.431680043 7.419615881
O 2.098736108 2.177780763 2.065176247
O 2.098259424 2.174969755 5.634860680
O 2.098988837 2.175442666 9.204889591
O 6.216165436 2.131067939 2.065082310
O 6.216576190 2.128345771 5.634798908
O 6.215701970 2.129414727 9.204752635
O 7.765984743 2.381229926 0.279771289
O 7.765570002 2.380563213 3.849835497
O 7.765875028 2.378311436 7.419631857
V 17.236471013 1.896116277 0.279183625
V 13.786334237 1.859726664 0.279326092
O 19.138329001 2.600545632 0.278744756
```

```
O 17.286916353 0.316976199 0.280444597
O 15.505815714 2.372763915 0.279849748
O 13.764721022 0.280015730 0.280527068
O 11.876847087 2.542337871 0.278732165
V 19.489133472 3.119891955 2.063768693
V 11.532336429 3.069907347 2.063623809
O 21.199207119 2.580165660 2.065693239
O 19.488667640 4.699699007 2.063845001
O 17.574515184 2.436820034 2.063903144
O 13.442395362 2.391757846 2.064009172
O 11.541235654 4.649857571 2.063264499
V 17.236240386 1.895691438 3.848548396
V 13.786570385 1.859395311 3.848741988
O 19.137616103 2.600353845 3.848771044
O 17.286226557 0.316520675 3.847234792
O 15.505817471 2.372932639 3.849065297
O 13.765474405 0.279658696 3.847573841
O 11.877481625 2.542293174 3.848793631
V 19.489253019 3.118394553 5.633664308
V 11.532340224 3.068585179 5.633595977
O 21.199179938 2.578414744 5.633738129
O 19.489098922 4.698257133 5.634576794
O 17.574799193 2.434316282 5.633697690
O 13.442204003 2.389499440 5.633813729
O 11.541066190 4.648544845 5.634186358
V 17.236386659 1.894412301 7.418608689
V 13.786522518 1.858156574 7.418786593
O 19.137951215 2.598193050 7.418544725
O 17.286633254 0.315261868 7.418756362
```

```
O 15.505873904 2.371443232 7.417231303
O 13.765113293 0.278434854 7.418970606
O 11.877270667 2.540143861 7.418606652
V 19.489087530 3.118486045 9.202993883
V 11.532585131 3.068694054 9.202905123
O 21.199268839 2.579024302 9.203077071
O 19.488540990 4.698313783 9.201107071
O 17.574136333 2.434901574 9.203671803
O 13.442962710 2.390087921 9.203775207
O 11.541922060 4.648692577 9.200844706
```

S7.2 One unit removed

```
77


V 0.237822914 2.979406333 2.067065634
V 0.254063309 2.983074603 5.637867285
V 0.254280773 2.981287096 9.202296357
V 2.390477013 1.628414302 0.283980673
V 2.380562304 1.622866063 3.851456798
V 2.393454452 1.623761537 7.420496731
V 5.887348998 1.601523206 0.272628445
V 5.873895486 1.605355188 3.864545959
V 5.884939016 1.599488892 7.419862749
V 8.043200286 2.914663647 2.061118389
V 8.116396691 2.885419605 5.659362263
V 8.155933196 2.956732310 9.196339942
O 9.843439449 2.546324954 2.017099683
O 9.905734239 2.486288760 5.762603855
O 9.735375822 2.610902583 9.152611632
```

```
O 4.092179334 2.034039911 0.303114644
O 4.086429316 2.020790136 3.851152447
O 4.092566340 2.028816308 7.398638350
O 0.308593990 4.553046892 2.073496842
O 0.314609244 4.556708822 5.634616763
O 0.316201377 4.555202043 9.196164528
O 2.239623259 0.050758291 0.289469153
O 2.236699045 0.045283745 3.853834986
O 2.241227288 0.046638781 7.414677183
O 5.960566202 0.025635016 0.294982162
O 5.948211849 0.028756726 3.855001897
O 5.957784635 0.023840217 7.405279226
O 7.933183122 4.489847409 2.067123574
O 7.969435212 4.456022727 5.639638252
O 8.026145779 4.560997599 9.193058524
O 0.492892028 2.469600734 0.282923385
O 0.489730220 2.455410663 3.851210066
O 0.501659136 2.454891276 7.420439757
O 2.039788234 2.206878902 2.067232524
O 2.048439735 2.209491668 5.633762479
O 2.049371549 2.198136885 9.206503813
O 6.139011137 2.179383980 2.097314984
O 6.146740963 2.178352705 5.612349930
O 6.106094836 2.073152997 9.203464313
O 7.724911709 2.355847481 0.322647080
O 7.781285950 2.341682088 3.864854958
O 7.716686642 2.340075049 7.378008954
V 17.161773328 1.942691478 0.274483219
V 13.774978077 1.889439813 0.567442645
```

```
O 19.076790057 2.611757532 0.241347034
O 17.280760402 0.365147583 0.280536981
O 15.464339441 2.439270607 0.112517469
O 13.700097020 0.320953289 0.309322423
O 12.195564751 2.585463119 0.164078739
V 19.516703586 3.085055079 2.049886104
V 11.534907303 3.045680956 1.846863761
O 21.164442047 2.500951234 2.061401468
O 19.576694845 4.664412891 2.066188456
O 17.573585215 2.442467881 2.046758374
O 13.599630510 2.404342542 2.245364565
O 11.565659890 4.625138103 1.961174367
V 17.220779126 1.906895080 3.831604909
V 13.771880179 1.888231000 4.099471489
O 19.098155038 2.599733000 3.872839842
O 17.318810714 0.324642534 3.853859659
O 15.538654901 2.390402830 3.903520818
O 13.771758240 0.306933646 3.993288023
O 11.863431458 2.537891651 3.711131192
V 19.552571170 3.096886028 5.598024826
V 11.558265569 3.043917452 5.399755660
O 21.195068139 2.524819331 5.626502061
O 19.588609667 4.676682284 5.636801003
O 17.440738343 2.526951064 5.737637913
O 13.213659467 2.323966686 5.774723096
O 11.635568644 4.617913055 5.613986499
V 17.592148049 1.879230459 7.412496394
O 19.353023874 2.407150478 7.418514686
O 17.355517445 0.319546463 7.409796464
```

```
V 19.552313139 3.093422405 9.233108839
O 21.195713766 2.519261440 9.210590289
O 19.584838076 4.672890864 9.187049804
O 17.435906443 2.522152010 9.091983760
```

S7.3 Two units removed

```
70


V 0.212492288 2.988605214 2.060326026
V 0.225827489 2.989019229 5.652658786
V 0.224714143 2.983281684 9.190162706
V 2.411883683 1.635030560 0.271802155
V 2.352740438 1.619412839 3.854507679
V 2.459342115 1.598559597 7.425372642
V 5.892595301 1.641949175 0.496029386
V 5.835375459 1.621656943 4.025577405
V 8.040075813 2.914478302 1.893122592
V 8.012332165 2.880679322 5.427964738
O 9.828623640 2.538510570 2.060730716
O 9.861168473 2.494630141 5.807055370
O 4.182845843 2.056597500 0.219816843
O 4.122512274 2.027475259 3.851765789
O 4.028403359 1.978034440 7.444323600
O 0.291077928 4.561170212 2.077903526
O 0.299343322 4.560016083 5.633924365
O 0.300695022 4.554291925 9.192026354
O 2.222219183 0.058171758 0.294426573
O 2.220615442 0.036168036 3.857805884
O 2.269799194 0.001220827 7.412462024
```

```
O 5.981790324 0.076368641 0.280237858
O 5.948622783 0.048921274 3.887182195
O 7.921155041 4.485161600 2.034678438
O 7.885036845 4.446344143 5.645965992
O 0.462002646 2.428729484 0.289704994
O 0.460559129 2.420094634 3.836747986
O 0.433483347 2.482770291 7.419767257
O 2.069691520 2.205708297 2.061480150
O 2.048170259 2.226828474 5.586620491
O 2.051238194 2.215118219 9.260042608
O 6.126214988 2.141283170 2.196234016
O 6.377513632 2.180870557 5.717402933
O 7.559169295 2.381169006 0.220668974
O 7.812283867 2.395803881 3.736220554
V 17.200072872 1.918440699 0.293493618
V 13.750469959 1.910372380 0.523607496
O 19.138736353 2.568067202 0.250904540
O 17.341219462 0.345228330 0.292505437
O 15.508200828 2.405284667 0.182863846
O 13.761019049 0.344796299 0.275734622
O 12.094151243 2.527742292 0.194646995
V 19.561880485 3.104897801 2.056745798
V 11.522287478 3.045359782 1.910207136
O 21.204093662 2.505613173 2.067975651
O 19.581454905 4.688220372 2.073947549
O 17.607991507 2.440287273 2.055064802
O 13.544911844 2.402744941 2.201442237
O 11.553472600 4.622388374 2.037050492
V 17.264531281 1.898020664 3.828970304
```

```
V 13.818722214 1.900397347 4.047513542
O 19.144114528 2.562507664 3.865363823
O 17.342243223 0.322095613 3.850861838
O 15.572029969 2.385500372 3.859920563
O 13.799169451 0.325814154 3.892281881
O 11.850629599 2.540426211 3.730126818
V 19.577046573 3.109745959 5.589155834
V 11.534927387 3.014995607 5.439251539
O 21.209825844 2.509536098 5.631379690
O 19.586277263 4.691806997 5.634196280
O 17.483157551 2.475703696 5.687125313
O 13.304773384 2.401764810 5.706123405
O 11.587435039 4.586856851 5.643505725
V 17.550474415 1.899280061 7.418526751
O 19.264529867 2.479981689 7.412917334
O 17.322955030 0.340388863 7.407144516
V 19.576601089 3.104266785 9.244371520
O 21.208213840 2.509844213 9.193832650
O 19.584333871 4.686172608 9.184590476
O 17.480251888 2.466028869 9.143780376
```

Electronic Supplementary Material (ESI) for Physical Chemistry Chemical Physics.

Supporting Information: Synthesis of nanosized vanadium(V) oxide clusters below 10 nm

Maximilian Lasserus, Daniel Knez, Florian Lackner, Martin Schnedlitz, Roman Messner, Daniel Schennach, Gerald Kothleitner, Ferdinand Hofer, Andreas W. Hauser, and Wolfgang E. Ernst

E-mail:

In the Supporting Information we present a detailed analysis of the EEL spectra presented in the main article.

Contents

1 EELS Analysis

Figure 1 shows a comparison between an EEL spectrum (black, normalized to the L2/L3 peak maximum) of the deposited nanoparticles and literature spectra taken from Ref. 1. The EEL spectrum represents the mean over 5 selected nanoparticles, a background obtained from an area that does not contain a nanoparticle has been subtracted. The background corresponds to an oxygen feature originating, presumably, from a contamination of the carbon TEM grid. Note that the same measured EEL spectrum is plotted for all four cases. The shown spectrum features the region containing both the V L-edge at 513 eV (L_3 $2p_{3/2}$) and 521 eV (L_2 $2p_{1/2}$) as well as the O K-edge at 532 eV (K 1s). As described above, the resolution in our experiment is lower than in previous bulk experiments where typical reported values are around 0.5 - 1 eV.[2] In order to account for this difference we convoluted the literature spectra with a Gaussian function such that the gap between the L2 and L3 peak matches our experimental spectrum. The employed FWHM of the Gaussian varies and lies between 1.4 and 2.4 eV. In addition to the convolution the literature spectra have been red-shifted by 0.75 eV.

To determine the oxidation state of vanadium oxides from EEL spectra, two characteristic O 1s pre-edge peaks located around round 530 eV serve as fingerprint features. They are associated with transitions into unoccupied t_{2g} and e_g energy levels, which emerge from a hybridization of V 3d and O 2p orbitals. However, from the modified literature spectra in Figure 1 it becomes obvious that the oxidation state can not be identified in the case of our nanoparticles because the characteristic features are blurred and appear only as a high-energy shoulder due to the relatively low energy resolution. Furthermore, even though the L2/L3 peak ratio is approximately 1 in the recorded EEL spectrum, suggesting a higher oxidation state such as V_2O_5,[1,3] the limited resolution demands care and we refrain from taking this as a definite evidence for a V_2O_5 stoichiometry.

Based on the above discussion we conclude that EELS as the standard method in transmission electron microscopy for the identification of oxidation states is not sufficiently sensitive

in the case of our deposited nanoparticles. However, the results would agree with V_2O_5 as possible stoichiometry but for a confirmation additional methods have to be employed, which are presented in the main manuscript.

.

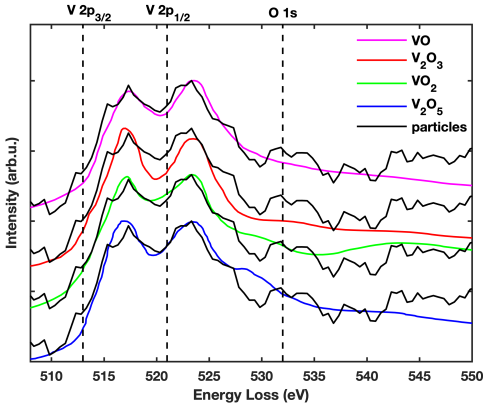

Figure 1: EEL spectrum normalized to the L2/L3 peak maximum obtained by averaging over 5 different nanoparticles (black) and compared to literature reference spectra for V_2O_5 (blue), VO_2 (green), V_2O_3 (red) and VO (purple) taken from Ref. 1. The literature spectra have been convoluted by a Gaussian function in order to match the energy resolution.

References

(1) Li, J.; Gauntt, B.; Kulik, J.; Dickey, E. Stoichiometry of nanocrystalline VOx thin films determined by electron energy loss spectroscopy. *Microscopy and Microanalysis* **2009**, *15*, 1004–1005.

(2) Hébert, C.; Willinger, M.; Su, D. S.; Pongratz, P.; Schattschneider, P.; Schlögl, R. Oxygen K-edge in vanadium oxides: simulations and experiments. *The European Physical Journal B-Condensed Matter and Complex Systems* **2002**, *28*, 407–414.

(3) Lin, X.; Wang, Y.; Dravid, V. P.; Michalakos, P.; Kung, M. Valence states and hybridization in vanadium oxide systems investigated by transmission electron-energy-loss spectroscopy. *Physical Review B* **1993**, *47*, 3477.

11 Bibliography

[1] Jiang, Q., Zhang, S. & Li, J. Grain size-dependent diffusion activation energy in nanomaterials. *Solid State Communications* **130**, 581–584 (2004).

[2] Lee, J. & Sim, K. J. General equations of calphad-type thermodynamic description for metallic nanoparticle systems. *Calphad* **44**, 129 – 132sol (2014). URL `http://www.sciencedirect.com/science/article/pii/S0364591613000643`. Special Issue: TOFA 2012 a Discussion Meeting on Thermodynamics of Alloys.

[3] Chen, S.-Y. *et al.* Electron energy loss spectroscopy and ab initio investigation of iron oxide nanomaterials grown by a hydrothermal process. *Physical Review B* **79**, 104103 (2009).

[4] Ewels, P., Sikora, T., Serin, V., Ewels, C. P. & Lajaunie, L. A complete overhaul of the electron energy-loss spectroscopy and x-ray absorption spectroscopy database: eelsdb.eu. *Microscopy and Microanalysis* **22**, 1–8 (2016). URL `http://journals.cambridge.org/article_S1431927616000179`.

[5] Pinna, N., Willinger, M., Weiss, K., Urban, J. & Schlögl, R. Local structure of nanoscopic materials: V_2O_5 nanorods and nanowires. *Nano Letters* **3**, 1131–1134 (2003).

[6] Zachariasen, W. Untersuchungen über die Kristallstrukturen von Sesquioxiden und Verbindungen ABO3. *Geologiska Föreningen i Stockholm Förhandlingar* **51**, 123–123 (1929).

[7] Dernier, P. Structural investigation of the metal-insulator transition in V_6O_{13}. *Materials Research Bulletin* **9**, 955–963 (1974).

[8] Schoenberg, N. X-ray studies on vanadium and chromium oxides with low oxygen content. *Acta Chemica Scandinavica* **8**, 221–225 (1954).

[9] Wyckoff, R. Structures of complex binary compounds R_nX_m. *Crystal Structures; J. Wiley and Sons: New York, NY, USA* **2** (1964).

[10] Ketelaar, J. Crystal structure and shape of colloidal particles of vanadium pentoxide. *Nature* **137**, 316 (1936).

[11] Choi, N. H., Kwon, S.-k. & Kim, H. Analysis of the oxidation of the V (ii) by dissolved oxygen using UV-visible spectrophotometry in a vanadium redox flow battery. *Journal of The Electrochemical Society* **160**, A973–A979 (2013).

[12] *PrismaPlus(TM) Compact Mass Spectrometer System QMG 220.*

[13] Horikoshi, S. & Serpone, N. *Introduction to Nanoparticles*, chap. 1, 1–24 (John Wiley & Sons, Ltd, 2013).

[14] Gu, Z.-Z. *et al.* Structural color and the lotus effect. *Angewandte Chemie International Edition* **42**, 894–897 (2003).

[15] Mozhayskiy, V., Slipchenko, M. N., Adamchuk, V. K. & Vilesov, A. F. Use of helium nanodroplets for assembly, transport, and surface deposition of large molecular and atomic clusters. *The Journal of Chemical Physics* **127**, 094701 (2007).

[16] Aldrich, L. & Nier, A. O. The abundance of He^3 in atmospheric and well helium. *Physical Review* **70**, 983 (1946).

[17] Ancilotto, F., Lerner, P. B. & Cole, M. W. Physics of solvation. *Journal of Low Temperature Physics* **101**, 1123–1146 (1995).

[18] Lackner, F., Krois, G., Theisen, M., Koch, M. & Ernst, W. Spectroscopy of n S, n P, and n D Rydberg series of Cs atoms on helium nanodroplets. *Physical Chemistry Chemical Physics* **13**, 18781–18788 (2011).

[19] Anantram, M., Lundstrom, M. S. & Nikonov, D. E. Modeling of nanoscale devices. *Proceedings of the IEEE* **96**, 1511–1550 (2008).

[20] Strasser, P. *et al.* Lattice-strain control of the activity in dealloyed core–shell fuel cell catalysts. *Nature Chemistry* **2**, 454–460 (2010).

[21] Zhu, J. Surface plasmon resonance from bimetallic interface in Au–Ag core–shell structure nanowires. *Nanoscale Research Letters* **4**, 977 (2009).

[22] Wanjala, B. N. *et al.* Nanoscale alloying, phase-segregation, and core- shell evolution of gold- platinum nanoparticles and their electrocatalytic effect on oxygen reduction reaction. *Chemistry of Materials* **22**, 4282–4294 (2010).

[23] Pan, Y.-T. & Yang, H. Design of bimetallic catalysts and electrocatalysts through the control of reactive environments. *Nano Today* 100832 (2020). URL `http://www.sciencedirect.com/science/article/pii/S1748013219304748`.

[24] Lopez, N. & Nørskov, J. K. Catalytic CO oxidation by a gold nanoparticle: A density functional study. *Journal of the American Chemical Society* **124**, 11262–11263 (2002).

[25] Schnedlitz, M. *A study of thermally induced surface diffusion processes of monometallic nanowires.* Master's thesis, Graz University of Technology (2017).

[26] Tamogl, A. *Surface Dynamics and Structure of Bi(111) from Helium Atom Scattering.* Ph.D. thesis, Graz University of Technology (2015).

[27] Schnedlitz, M. *et al.* Thermally induced breakup of metallic nanowires: experiment and theory. *Physical Chemistry Chemical Physics* **19**, 9402–9408 (2017). URL http://dx.doi.org/10.1039/C7CP00463J.

[28] Hartmann, M., Miller, R., Toennies, J. & Vilesov, A. Rotationally resolved spectroscopy of SF_6 in liquid helium clusters: A molecular probe of cluster temperature. *Physical Review Letters* **75**, 1566 (1995).

[29] Steurer, J. *Helium Droplet Mediated Fabrication and Analysis of Noble Metal Nanoparticles.* Master's thesis, Graz University of Technology (2014).

[30] Ellis, A. M. & Yang, S. Model for the charge-transfer probability in helium nanodroplets following electron-impact ionization. *Physical Review A* **76**, 032714 (2007).

[31] Denifl, S. Formation of cations and anions upon electron interaction with (doped) helium droplets. *The European Physical Journal Special Topics* **222**, 2017–2033 (2013).

[32] Schöbel, H. *et al.* Sequential penning ionization: harvesting energy with ions. *Physical Review Letters* **105**, 243402 (2010).

[33] Wiza, J. L. Microchannel plate detectors. *Nuclear Instruments and Methods* **162**, 587–601 (1979).

[34] Bartelt, A., Close, J. D., Federmann, F., Quaas, N. & Toennies, J. P. Cold metal clusters: helium droplets as a nanoscale cryostat. *Physical Review Letters* **77**, 3525–3528 (1996).

[35] Haynes, W. M. *CRC Handbook of Chemistry and Physics* (CRC press, 2014).

[36] Sauerbrey, G. Verwendung von Schwingquarzen zur Wägung dünner Schichten und zur Mikrowägung. *Zeitschrift für Physik* **155**, 206–222 (1959).

[37] Williams, D. B. & Carter, C. B. The transmission electron microscope. In *Transmission Electron Microscopy*, 3–17 (Springer, 1996).

[38] Spreadborough, J. & Christian, J. High-temperature x-ray diffractometer. *Journal of Scientific Instruments* **36**, 116 (1959).

[39] *Instruction Manual Operation Guide UV-1800 Shimadzu Spectrophotometer.*

[40] *Corning® HPFS® 7979, 7980, 8655 Fused Silica Optical Materials Product Information Specialty Materials Division.*

[41] Lackner, F. *et al.* Helium nanodroplet assisted synthesis of bimetallic Ag@Au nanoparticles with tunable localized surface plasmon resonance. *The European Physical Journal D* **73**, 104 (2019).

[42] Haruta, M. & Daté, M. Advances in the catalysis of au nanoparticles. *Applied Catalysis A: General* **222**, 427–437 (2001).

[43] Guisbiers, G. *et al.* Electrum, the gold–silver alloy, from the bulk scale to the nanoscale: synthesis, properties, and segregation rules. *ACS Nano* **10**, 188–198 (2015).

[44] Calvo, F., Combe, N., Morillo, J. & Benoit, M. Modeling iron–gold nanoparticles using a dedicated semi-empirical potential: Application to the stability of core–shell structures. *The Journal of Physical Chemistry C* **121**, 4680–4691 (2017).

[45] Zhou, S. *et al.* In situ phase separation of NiAu alloy nanoparticles for preparing highly active Au/NiO CO oxidation catalysts. *ChemPhysChem* **9**, 2475–2479 (2008).

[46] Hammer, B. & Norskov, J. Why gold is the noblest of all the metals. *Nature* **376**, 238–240 (1995).

[47] Roduner, E. Size matters: why nanomaterials are different. *Chemical Society Reviews* **35**, 583–592 (2006).

[48] Boccuzzi, F. *et al.* Gold, silver and copper catalysts supported on TiO_2 for pure hydrogen production. *Catalysis Today* **75**, 169–175 (2002).

[49] Conde, J., Doria, G. & Baptista, P. Noble metal nanoparticles applications in cancer. *Journal of Drug Delivery* **2012**, 1–12 (2011).

[50] Lee, J. & Sim, K. J. General equations of calphad-type thermodynamic description for metallic nanoparticle systems. *Calphad* **44**, 129–132 (2014).

[51] Sopoušek, J. *et al.* $Au - Ni$ nanoparticles: Phase diagram prediction, synthesis, characterization, and thermal stability. *Calphad* **58**, 25–33 (2017).

[52] Park, J. & Lee, J. Phase diagram reassessment of Ag–Au system including size effect. *Calphad* **32**, 135–141 (2008).

[53] Hodak, J. H., Henglein, A., Giersig, M. & Hartland, G. V. Laser-induced interdiffusion in AuAg core- shell nanoparticles. *The Journal of Physical Chemistry B* **104**, 11708–11718 (2000).

[54] Shibata, T. *et al.* Size-dependent spontaneous alloying of Au-Ag nanoparticles. *Journal of the American Chemical Society* **124**, 11989–11996 (2002).

[55] Toennies, J. P. & Vilesov, A. F. Superfluid helium droplets: A uniquely cold nanomatrix for molecules and molecular complexes. *Angewandte Chemie International Edition* **43**, 2622–2648 (2004).

[56] Callegari, C. & Ernst, W. E. *Handbook of High-Resolution Spectroscopy,* eds. M. Quack and F. Merkt, vol. 3, 1551–1594 (John Wiley & Sons, Chichester, 2011).

[57] Tiggesbäumker, J. & Stienkemeier, F. Formation and properties of metal clusters isolated in helium droplets. *Physical Chemistry Chemical Physics* **9**, 4748–4770 (2007).

[58] Mozhayskiy, V., Slipchenko, M. N., Adamchuk, V. K. & Vilesov, A. F. Use of helium nanodroplets for assembly, transport, and surface deposition of large molecular and atomic clusters. *Journal of Chemical Physics* **127**, 094701 (2007).

[59] Loginov, E., Gomez, L. F. & Vilesov, A. F. Surface deposition and imaging of large Ag clusters formed in He droplets. *Journal of Physical Chemistry A* **115**, 7199–7204 (2011).

[60] Volk, A. *et al.* High resolution electron microscopy of Ag-clusters in crystalline and non-crystalline morphologies grown inside superfluid helium nanodroplets. *Journal of Chemical Physics* **138**, 214312 (2013).

[61] Thaler, P., Volk, A., Ratschek, M., Koch, M. & Ernst, W. E. Molecular dynamics simulation of the deposition process of cold Ag-clusters under different landing conditions. *Journal of Chemical Physics* **140**, 044326 (2014).

[62] Thaler, P. *et al.* Formation of bimetallic core-shell nanowires along vortices in superfluid He nanodroplets. *Physical Review B* **90**, 155442 (2014).

[63] Latimer, E. *et al.* Preparation of ultrathin nanowires using superfluid helium droplets. *Nano Letters* **14**, 2902–2906 (2014).

[64] Volk, A. *et al.* Thermal instabilities and Rayleigh breakup of ultrathin silver nanowires grown in helium nanodroplets. *Physical Chemistry Chemical Physics* **17**, 24570–24575 (2015). URL `http://pubs.rsc.org/en/content/articlehtml/2015/cp/c5cp04696c`.

[65] de Lara-Castells, M. P. *et al.* Communication: Unraveling the ^{4}He droplet-mediated soft-landing from *ab initio*-assisted and time-resolved density functional simulations: Au@$^4He_{300}$/TiO_2(110). *Journal of Chemical Physics* **142**, 131101 (2015).

[66] Haberfehlner, G. *et al.* Formation of bimetallic clusters in superfluid helium nanodroplets analysed by atomic resolution electron tomography. *Nature Communications* **6**, 8779 (2015). URL http://www.nature.com/doifinder/10.1038/ncomms9779.

[67] Zhou, S., Jackson, G. & Eichhorn, B. AuPt alloy nanoparticles for CO-tolerant hydrogen activation: Architectural effects in Au-Pt bimetallic nanocatalysts. *Advanced Functional Materials* **17**, 3099–3104 (2007). URL http://dx.doi.org/10.1002/adfm.200700216.

[68] Zhou, S. *et al.* In Situ Phase Separation of NiAu Alloy Nanoparticles for Preparing Highly Active Au/NiO CO Oxidation Catalysts. *ChemPhysChem* **9**, 2475–2479 (2008). URL http://onlinelibrary.wiley.com/doi/10.1002/cphc.200800587/full.

[69] Feynman, R. P. Application of quantum mechanics to liquid helium. In Gorter, C. J. (ed.) *Progress in Low Temperature Physics*, 17–53 (North-Holland, Amsterdam, 1955).

[70] Onsager, L. Introductory talk. In *Proc. Int. Conf. Theor. Phys.*, 877–880 (Science Council of Japan, Tokyo, 1953).

[71] Aguirre, N. F., Mateo, D., Mitrushchenkov, A. O., Pi, M. & de Lara-Castells, M. P. Helium mediated deposition: Modeling the He−TiO_2(110)-(1×1) interaction potential and application to the collision of a helium droplet from density functional calculations. *The Journal of Chemical Physics* **136**, 124703 (2012). URL http://aip.scitation.org/doi/10.1063/1.3698173.

[72] Thaler, P. *et al.* Synthesis of nanoparticles in helium droplets-a characterization comparing mass-spectra and electron microscopy data. *The Journal of Chemical Physics* **143**, 134201 (2015).

[73] Volk, A. *et al.* Correction: The impact of doping rates on the morphologies of silver and gold nanowires grown in helium nanodroplets. *Physical Chemistry Chemical Physics* **18**, 1451–1459 and 3359 (2016). URL http://dx.doi.org/10.1039/C5CP90229K.

[74] Bewley, G. P., Lathrop, D. P. & Sreenivasan, K. R. Superfluid helium: Visualization of quantized vortices. *Nature* **441**, 588 (2006).

[75] Yarmchuk, E. J., Gordon, M. J. V. & Packard, R. E. Observation of stationary vortex arrays in rotating superfluid helium. *Physical Review Letters* **43**, 214–217 (1979).

[76] Williams, G. A. & Packard, R. E. Photographs of quantized vortex lines in rotating He II. *Physical Review Letters* **33**, 280–283 (1974).

[77] Donelly, R. J. *Quantized Vortices in Helium II* (Cambridge University Press, Cambridge, 1991).

[78] Sergeev, Y. A. & Barenghi, C. F. Particles-vortex interactions and flow visualization in ^{4}He. *Journal of Low Temperature Physics* **157**, 429–475 (2009).

[79] Gordon, E. B. *et al.* Structure and properties of platinum, gold and mercury nanowires grown in superfluid helium. *The Journal of Physical Chemistry Letters* **5**, 1072–1076 (2014).

[80] Gordon, E., Karabulin, A., Matyushenko, V., Sizov, V. & Khodos, I. Stability and structure of nanowires grown from silver, copper and their alloys by laser ablation into superfluid helium. *Physical Chemistry Chemical Physics* **16**, 25229–25233 (2014).

[81] Moroshkin, P. *et al.* Nanowire formation by gold nano-fragment coalescence on quantized vortices in He II. *EPL* **90**, 34002 (2010).

[82] Walther, T. & Humphreys, C. A quantitative study of compositional profiles of chemical vapour-deposited strained silicone germanium/silicon layers by transmission electron microscopy. *Journal of Crystal Growth* **197**, 113 – 128 (1999). URL `http://www.sciencedirect.com/science/article/pii/S0022024898009300`.

[83] Einstein, A. *Investigations on the Theory of the Brownian Movement* (Courier Corporation, 1956).

[84] Mallard, W., Gardner, A., Bass, R. F. & Slifkin, L. Self-diffusion in silver-gold solid solutions. *Physical Review* **129**, 617 (1963).

[85] Guisbiers, G. & Buchaillot, L. Size and shape effects on creep and diffusion at the nanoscale. *Nanotechnology* **19**, 435701 (2008).

[86] Mishra, S., Gupta, S. K., Jha, P. K. & Pratap, A. Study of dimension dependent diffusion coefficient of titanium dioxide nanoparticles. *Materials Chemistry and Physics* **123**, 791–794 (2010).

[87] Ouyang, G., Tan, X., Wang, C. & Yang, G. Physical and chemical origin of size-dependent spontaneous interfacial alloying of core–shell nanostructures. *Chemical Physics Letters* **420**, 65–70 (2006).

[88] Lindemann, F. A. *Physikalische Zeitschrift* **11**, 609 (1910).

[89] Qi, Y., Çağin, T., Johnson, W. L. & Goddard III, W. A. Melting and crystallization in Ni nanoclusters: The mesoscale regime. *The Journal of Chemical Physics* **115**, 385–394 (2001).

[90] Liang, L.-H., Shen, C.-M., Chen, X.-P., Liu, W.-M. & Gao, H.-J. The size-dependent phonon frequency of semiconductor nanocrystals. *Journal of Physics: Condensed Matter* **16**, 267 (2004).

[91] Hauser, A. W., Schnedlitz, M. & Ernst, W. E. A coarse-grained Monte Carlo approach to diffusion processes in metallic nanoparticles. *The European Physical Journal D* **71**, 150 (2017). URL `https://link.springer.com/article/10.1140/epjd/e2017-80084-y`.

[92] Wang, Z. L., Petroski, J. M., Green, T. C. & El-Sayed, M. A. Shape transformation and surface melting of cubic and tetrahedral platinum nanocrystals. *The Journal of Physical Chemistry B* **102**, 6145–6151 (1998).

[93] Jia, X., Li, J., Zhang, X. & Wang, E. Controlling the synthesis and assembly of fluorescent Au/Ag alloy nanoclusters. *Chemical Communications* **51**, 17417–17419 (2015).

[94] He, R. *et al.* Core/shell fluorescent magnetic silica-coated composite nanoparticles for bioconjugation. *Nanotechnology* **18**, 315601 (2007).

[95] Gupta, A. K. & Gupta, M. Synthesis and surface engineering of iron oxide nanoparticles for biomedical applications. *Biomaterials* **26**, 3995–4021 (2005).

[96] Sun, C., Lee, J. S. & Zhang, M. Magnetic nanoparticles in MR imaging and drug delivery. *Advanced Drug Delivery Reviews* **60**, 1252–1265 (2008).

[97] Gao, J., Gu, H. & Xu, B. Multifunctional magnetic nanoparticles: design, synthesis, and biomedical applications. *Accounts of Chemical Research* **42**, 1097–1107 (2009).

[98] Jiang, X., Du, B., Huang, Y. & Zheng, J. Ultrasmall noble metal nanoparticles: Breakthroughs and biomedical implications. *Nano Today* (2018).

[99] Liu, J., Chen, Q., Feng, L. & Liu, Z. Nanomedicine for tumor microenvironment modulation and cancer treatment enhancement. *Nano Today* (2018).

[100] Prilepskii, A. Y. *et al.* Urokinase-conjugated magnetite nanoparticles as a promising drug delivery system for targeted thrombolysis: Synthesis and preclinical evaluation. *ACS Applied Materials & Interfaces* **10**, 36764–36775 (2018). URL `https://doi.org/10.1021/acsami.8b14790`. PMID: 30299938, `https://doi.org/10.1021/acsami.8b14790`.

[101] Portet, D., Denizot, B., Rump, E., Lejeune, J.-J. & Jallet, P. Nonpolymeric coatings of iron oxide colloids for biological use as magnetic resonance imaging contrast agents. *Journal of Colloid and Interface Science* **238**, 37–42 (2001).

[102] Lee, J.-H. *et al.* Artificially engineered magnetic nanoparticles for ultra-sensitive molecular imaging. *Nature Medicine* **13**, 95 (2007).

[103] Teja, A. S. & Koh, P.-Y. Synthesis, properties, and applications of magnetic iron oxide nanoparticles. *Progress in Crystal Growth and Characterization of Materials* **55**, 22–45 (2009).

[104] Qiang, Y. *et al.* Iron/iron oxide core-shell nanoclusters for biomedical applications. *Journal of Nanoparticle Research* **8**, 489–496 (2006).

[105] Koo, B. *et al.* Hollow iron oxide nanoparticles for application in lithium ion batteries. *Nano Letters* **12**, 2429–2435 (2012).

[106] Knez, D. *et al.* Transformation dynamics of Ni clusters into NiO rings under electron beam irradiation. *Ultramicroscopy* (2017).

[107] Shukla, R. *et al.* Biocompatibility of gold nanoparticles and their endocytotic fate inside the cellular compartment: a microscopic overview. *Langmuir* **21**, 10644–10654 (2005).

[108] Huang, X. & El-Sayed, M. A. Gold nanoparticles: optical properties and implementations in cancer diagnosis and photothermal therapy. *Journal of Advanced Research* **1**, 13–28 (2010).

[109] Eustis, S. & El-Sayed, M. A. Why gold nanoparticles are more precious than pretty gold: noble metal surface plasmon resonance and its enhancement of the radiative and nonradiative properties of nanocrystals of different shapes. *Chemical Society Reviews* **35**, 209–217 (2006).

[110] Sperling, R. A., Gil, P. R., Zhang, F., Zanella, M. & Parak, W. J. Biological applications of gold nanoparticles. *Chemical Society Reviews* **37**, 1896–1908 (2008).

[111] Hayashi, K. *et al.* Gold nanoparticle cluster–plasmon-enhanced fluorescent silica core–shell nanoparticles for x-ray computed tomography–fluorescence dual-mode imaging of tumors. *Chemical Communications* **49**, 5334–5336 (2013).

[112] Moskovits, M., Srnová-Šloufová, I. & Vlčková, B. Bimetallic Ag–Au nanoparticles: extracting meaningful optical constants from the surface-plasmon extinction spectrum. *The Journal of Chemical Physics* **116**, 10435–10446 (2002).

[113] Jain, P. K., Huang, X., El-Sayed, I. H. & El-Sayed, M. A. Noble metals on the nanoscale: optical and photothermal properties and some applications in imaging, sensing, biology, and medicine. *Accounts of Chemical Research* **41**, 1578–1586 (2008).

[114] Cho, S.-J., Jarrett, B. R., Louie, A. Y. & Kauzlarich, S. M. Gold-coated iron nanoparticles: a novel magnetic resonance agent for T1 and T2 weighted imaging. *Nanotechnology* **17**, 640 (2006).

[115] Yu, H. *et al.* Dumbbell-like bifunctional Au- Fe_3O_4 nanoparticles. *Nano Letters* **5**, 379–382 (2005).

[116] Cho, S.-J. *et al.* Characterization and magnetic properties of core/shell structured Fe/Au nanoparticles. *Journal of Applied physics* **95**, 6804–6806 (2004).

[117] Shevchenko, E. V. *et al.* Gold/iron oxide core/hollow-shell nanoparticles. *Advanced Materials* **20**, 4323–4329 (2008).

[118] Schnedlitz, M. *et al.* Stability of core–shell nanoparticles for catalysis at elevated temperatures: Structural inversion in the Ni–Au system observed at atomic resolution. *Chemistry of Materials* **30**, 1113–1120 (2018).

[119] Callegari, C. & Ernst, W. E. Helium droplets as nanocryostats for molecular spectroscopy - from the vacuum ultraviolet to the microwave regime. In Merkt, F. & Quack, M. (eds.) *Handbook of High Resolution Spectroscopy*, vol. 3, 1551–1594 (John Wiley & Sons, Chichester, 2011).

[120] Haberfehlner, G. *et al.* Formation of bimetallic clusters in superfluid helium nanodroplets analysed by atomic resolution electron tomography. *Nature Communications* **6**, 8779 (2015).

[121] Cabot, A. *et al.* Vacancy coalescence during oxidation of iron nanoparticles. *Journal of the American Chemical Society* **129**, 10358–10360 (2007).

[122] Lasserus, M. *et al.* Thermally induced alloying processes in a bimetallic system at the nanoscale: AgAu sub-5 nm core–shell particles studied at atomic resolution. *Nanoscale* **10**, 2017–2024 (2018).

[123] Xu, C. *et al.* Au- Fe_3O_4 dumbbell nanoparticles as dual-functional probes. *Angewandte Chemie International Edition* **47**, 173–176 (2008).

[124] Lee, Y., Garcia, M. A., Frey Huls, N. A. & Sun, S. Synthetic tuning of the catalytic properties of Au- Fe_3O_4 nanoparticles. *Angewandte Chemie* **122**, 1293–1296 (2010).

[125] Miller, J. *et al.* The effect of gold particle size on AuAu bond length and reactivity toward oxygen in supported catalysts. *Journal of Catalysis* **240**, 222–234 (2006).

[126] Wang, C. *et al.* Morphology and electronic structure of the oxide shell on the surface of iron nanoparticles. *Journal of the American Chemical Society* **131**, 8824–8832 (2009).

[127] Colliex, C., Manoubi, T. & Ortiz, C. Electron-energy-loss-spectroscopy near-edge fine structures in the iron-oxygen system. *Physical Review B* **44**, 11402 (1991).

[128] Peng, S., Wang, C., Xie, J. & Sun, S. Synthesis and stabilization of monodisperse Fe nanoparticles. *Journal of the American Chemical Society* **128**, 10676–10677 (2006).

[129] Signorini, L. *et al.* Size-dependent oxidation in iron/iron oxide core-shell nanoparticles. *Physical Review B* **68**, 195423 (2003).

[130] Knez, D. *et al.* Modelling electron beam induced dynamics in metallic nanoclusters. *Ultramicroscopy* (2018).

[131] Wang, C. M. *et al.* Electron beam-induced thickening of the protective oxide layer around Fe nanoparticles. *Ultramicroscopy* **108**, 43–51 (2007).

[132] Perdew, J. P., Burke, K. & Ernzerhof, M. Generalized gradient approximation made simple. *Physical Review Letters* **77**, 3865–3868 (1996). URL `https://link.aps.org/doi/10.1103/PhysRevLett.77.3865`.

[133] Blöchl, P. E. Projector augmented-wave method. *Physical Review B* **50**, 17953–17979 (1994). URL `https://link.aps.org/doi/10.1103/PhysRevB.50.17953`.

[134] Kresse, G. & Joubert, D. From ultrasoft pseudopotentials to the projector augmented-wave method. *Physical Review B* **59**, 1758–1775 (1999). URL `https://link.aps.org/doi/10.1103/PhysRevB.59.1758`.

[135] Giannozzi, P. *et al.* Quantum espresso: a modular and open-source software project for quantum simulations of materials. *Journal of Physics: Condensed Matter* **21**, 395502 (19pp) (2009). URL `http://www.quantum-espresso.org`.

[136] Forzatti, P. Present status and perspectives in de-NO_x SCR catalysis. *Applied Catalysis A: General* **222**, 221 – 236 (2001). URL `http://www.sciencedirect.com/science/article/pii/S0926860X01008328`. Celebration Issue.

[137] Mamedov, E. & Corberán, V. C. Oxidative dehydrogenation of lower alkanes on vanadium oxide-based catalysts. the present state of the art and outlooks. *Applied Catalysis A: General* **127**, 1 – 40 (1995). URL http://www.sciencedirect.com/science/article/pii/0926860X95000569.

[138] Haber, J., Witko, M. & Tokarz, R. Vanadium pentoxide I. structures and properties. *Applied Catalysis A: General* **157**, 3 – 22 (1997). URL http://www.sciencedirect.com/science/article/pii/S0926860X97000173. Vanadia catalysts for selective oxidation of hydrocarbons and their derivatives.

[139] Chain, E. E. Optical properties of vanadium dioxide and vanadium pentoxide thin films. *Applied Optics* **30**, 2782–2787 (1991). URL http://ao.osa.org/abstract.cfm?URI=ao-30-19-2782.

[140] Winter, M., Besenhard, J. O., Spahr, M. E. & Novák, P. Insertion electrode materials for rechargeable lithium batteries. *Advanced Materials* **10**, 725–763 (1998).

[141] Spahr, M. E. *et al.* Redox-active nanotubes of vanadium oxide. *Angewandte Chemie International Edition* **37**, 1263–1265 (1998).

[142] Nesper, R. & Muhr, H.-J. Nanotubes an outstanding set of nano particles? *CHIMIA International Journal for Chemistry* **52**, 571–578 (1998). URL https://www.ingentaconnect.com/content/scs/chimia/1998/00000052/00000010/art00011.

[143] Schoiswohl, J., Surnev, S., Netzer, F. P. & Kresse, G. Vanadium oxide nanostructures: from zero- to three-dimensional. *Journal of Physics: Condensed Matter* **18**, R1 (2006). URL http://stacks.iop.org/0953-8984/18/i=4/a=R01.

[144] Livage, J. Hydrothermal synthesis of nanostructured vanadium oxides. *Materials* **3**, 4175–4195 (2010).

[145] Wang, D., Xie, T. & Li, Y. Nanocrystals: Solution-based synthesis and applications as nanocatalysts. *Nano Research* **2**, 30–46 (2009). URL https://doi.org/10.1007/s12274-009-9007-x.

[146] Gvishi, R. Fast sol–gel technology: from fabrication to applications. *Journal of Sol-Gel Science and Technology* **50**, 241 (2009). URL https://doi.org/10.1007/s10971-008-1885-y.

[147] Kwon, S. G. & Hyeon, T. Colloidal chemical synthesis and formation kinetics of uniformly sized nanocrystals of metals, oxides, and chalcogenides. *Accounts of Chemical Research* **41**, 1696–1709 (2008). URL https://doi.org/10.1021/ar8000537. PMID: 18681462, https://doi.org/10.1021/ar8000537.

[148] Rao, C., Vivekchand, S., Biswas, K. & Govindaraj, A. Synthesis of inorganic nanomaterials. *Dalton Transactions* 3728–3749 (2007).

[149] Chaudret, B. & Philippot, K. Organometallic nanoparticles of metals or metal oxides. *Oil & Gas Science and Technology-Revue de l'IFP* **62**, 799–817 (2007).

[150] Lim, J. K., Majetich, S. A. & Tilton, R. D. Stabilization of superparamagnetic iron oxide core- gold shell nanoparticles in high ionic strength media. *Langmuir* **25**, 13384–13393 (2009).

[151] Tang, J. *et al.* An organometallic synthesis of TiO_2 nanoparticles. *Nano Letters* **5**, 543–548 (2005).

[152] Cushing, B. L., Kolesnichenko, V. L. & O'Connor, C. J. Recent advances in the liquid-phase syntheses of inorganic nanoparticles. *Chemical Reviews* **104**, 3893–3946 (2004).

[153] Rockenberger, J., Scher, E. C. & Alivisatos, A. P. A new nonhydrolytic single-precursor approach to surfactant-capped nanocrystals of transition metal oxides. *Journal of the American Chemical Society* **121**, 11595–11596 (1999).

[154] Dietz, T. G., Duncan, M. A., Powers, D. E. & Smalley, R. E. Laser production of supersonic metal cluster beams. *The Journal of Chemical Physics* **74**, 6511–6512 (1981).

[155] Ard, S., Dibble, C., Akin, S. & Duncan, M. Ligand-coated vanadium oxide clusters: capturing gas-phase magic numbers in solution. *The Journal of Physical Chemistry C* **115**, 6438–6447 (2011).

[156] Bergeron, D. E., Castleman, A. W., Jones, N. O. & Khanna, S. N. Stable cluster motifs for nanoscale chromium oxide materials. *Nano Letters* **4**, 261–265 (2004).

[157] Moore, N. A., Mitrić, R., Justes, D. R., Bonačić-Kouteckỳ, V. & Castleman, A. Kinetic analysis of the reaction between (V_2O_5) n= 1, 2+ and ethylene. *The Journal of Physical Chemistry B* **110**, 3015–3022 (2006).

[158] Feyel, S., Schröder, D., Rozanska, X., Sauer, J. & Schwarz, H. Gas-phase oxidation of propane and 1-butene with $[V_3O_7]$+: Experiment and theory in concert. *Angewandte Chemie International Edition* **45**, 4677–4681 (2006).

[159] Molek, K., Reed, Z., Ricks, A. & Duncan, M. Photodissociation of chromium oxide cluster cations. *The Journal of Physical Chemistry A* **111**, 8080–8089 (2007).

[160] Fielicke, A. & Rademann, K. Stability and reactivity patterns of medium-sized vanadium oxide cluster cations $V_xO_y+(4 \leq x \leq 14)$. *Physical Chemistry Chemical Physics* **4**, 2621–2628 (2002).

[161] Wang, L.-S., Wu, H., Desai, S. R. & Lou, L. Electronic structure of small copper oxide clusters: From Cu_2O to Cu_2O_4. *Physical Review B* **53**, 8028 (1996).

[162] Dong, F., Heinbuch, S., Xie, Y., Rocca, J. J. & Bernstein, E. R. Reactions of neutral vanadium oxide clusters with methanol. *The Journal of Physical Chemistry A* **113**, 3029–3040 (2009).

[163] Green, S. M. *et al.* Negative ion photoelectron spectroscopy of the group 5 metal trimer monoxides V_3O, Nb_3O, and Ta_3O. *The Journal of Chemical Physics* **114**, 2653–2668 (2001).

[164] Pramann, A., Koyasu, K., Nakajima, A. & Kaya, K. Photoelectron spectroscopy of cobalt oxide cluster anions. *The Journal of Physical Chemistry A* **106**, 4891–4896 (2002).

[165] Yoder, B. L., Maze, J. T., Raghavachari, K. & Jarrold, C. C. Structures of Mo_2O_y- and Mo_2O_y (y= 2, 3, and 4) studied by anion photoelectron spectroscopy and density functional theory calculations. *The Journal of Chemical Physics* **122**, 094313 (2005).

[166] Fielicke, A., Meijer, G. & Von Helden, G. Infrared multiple photon dissociation spectroscopy of transition metal oxide cluster cations. *The European Physical Journal D-Atomic, Molecular, Optical and Plasma Physics* **24**, 69–72 (2003).

[167] Asmis, K. R. *et al.* Gas phase infrared spectroscopy of mono-and divanadium oxide cluster cations. *The Journal of Chemical Physics* **120**, 6461–6470 (2004).

[168] Koh, A. L. *et al.* Electron energy-loss spectroscopy (EELS) of surface plasmons in single silver nanoparticles and dimers: influence of beam damage and mapping of dark modes. *ACS Nano* **3**, 3015–3022 (2009).

[169] Melzer, M. *et al.* Preparation of vanadium and vanadium oxide clusters by means of inert gas aggregation. *Catalysis Letters* **81**, 219–221 (2002).

[170] Slater, T. J. *et al.* Stem-edx tomography of bimetallic nanoparticles: A methodological investigation. *Ultramicroscopy* **162**, 61–73 (2016).

[171] Schiffmann, K. I. *et al.* Sizes and distances of metal clusters in Au-, Pt-, W-and Fe-containing diamond-like carbon hard coatings: a comparative study by small angle x-ray scattering, wide angle x-ray diffraction, transmission electron microscopy and scanning tunnelling microscopy. *Thin Solid Films* **347**, 60–71 (1999).

[172] Lewis, W. K. *et al.* Electron impact ionization in helium nanodroplets: Controlling fragmentation by active cooling of molecular ions. *Journal of the American Chemical Society* **126**, 11283–11292 (2004). URL https://doi.org/10.1021/ja030653q. https://doi.org/10.1021/ja030653q.

[173] Bartl, P. *et al.* Electron ionization of different large perfluoroethers embedded in ultracold helium droplets: effective freezing of short-lived decomposition intermediates. *Rapid Communications in Mass Spectrometry* **27**, 298–304 (2013). URL https://onlinelibrary.wiley.com/doi/abs/10.1002/rcm.6459. https://onlinelibrary.wiley.com/doi/pdf/10.1002/rcm.6459.

[174] Lindebner, F., Kautsch, A., Koch, M. & Ernst, W. E. Laser ionization and spectroscopy of Cu in superfluid helium nanodroplets. *International Journal of Mass Spectrometry* **365-366**, 255–259 (2014). URL https://linkinghub.elsevier.com/retrieve/pii/S1387380613004582.

[175] Milan, E. F. The dissociation pressure of vanadium pentoxide. *The Journal of Physical Chemistry* **33**, 498–508 (1928). URL https://doi.org/10.1021/j150298a002. https://doi.org/10.1021/j150298a002.

[176] Beattie, I. R., Ogden, J. S. & Price, D. D. The characterization of molecular vanadium oxide (V_4O_{10}), an analog of phosphorus oxide (P_4O_{10}). *Inorganic Chemistry* **17**, 3296–3297 (1978).

[177] Vyboishchikov, S. F. & Sauer, J. (V_2O_5)n Gas-Phase Clusters (n = 1-12) Compared to V_2O_5 Crystal: DFT Calculations. *The Journal of Physical Chemistry A* **105**, 8588–8598 (2001). URL http://pubs.acs.org/doi/abs/10.1021/jp012294w.

[178] Bell, R. C., Zemski, K. A., Justes, D. R. & Castleman, A. W. Formation, structure and bond dissociation thresholds of gas-phase vanadium oxide cluster ions. *The Journal of Chemical Physics* **114**, 798–811 (2001). URL https://aip.scitation.org/doi/abs/10.1063/1.1329643.

[179] Feyel, S. *et al.* Gas-phase infrared photodissociation spectroscopy of tetravanadiumoxo and oxo-methoxo cluster anions. *ChemPhysChem* **8**, 1640–1647 (2007). URL https://onlinelibrary.wiley.com/doi/abs/10.1002/cphc.200700255. https://onlinelibrary.wiley.com/doi/pdf/10.1002/cphc.200700255.

[180] Santambrogio, G. *et al.* Gas phase vibrational spectroscopy of mass-selected vanadium oxide anions. *Physical Chemistry Chemical Physics* **10**, 3992–4005 (2008). URL http://dx.doi.org/10.1039/B803492C.

[181] Wu, J. W. J., Moriyama, R., Tahara, H., Ohshimo, K. & Misaizu, F. Compositions and structures of vanadium oxide cluster ions V_mO_n (m = 2-20) investigated by ion mobility mass spectrometry. *The Journal of Physical Chemistry A* **120**, 3788–3796 (2016). PMID: 27172006.

[182] Asmis, K. R. & Sauer, J. Mass-selective vibrational spectroscopy of vanadium oxide cluster ions. *Mass Spectrometry Reviews* **26**, 542–562. URL https://onlinelibrary.wiley.com/doi/abs/10.1002/mas.20136. https://onlinelibrary.wiley.com/doi/pdf/10.1002/mas.20136.

[183] Guimond, S. *et al.* Vanadium oxide surfaces and supported vanadium oxide nanoparticles. *Topics in Catalysis* **38**, 117–125 (2006). URL https://doi.org/10.1007/s11244-006-0076-8.

[184] Mardirossian, N. & Head-Gordon, M. ωB97X-V: A 10-parameter, range-separated hybrid, generalized gradient approximation density functional with nonlocal correlation, designed by a survival-of-the-fittest strategy. *Physical Chemistry Chemical Physics* **16**, 9904–9924 (2014). URL http://xlink.rsc.org/?DOI=c3cp54374a.

[185] Grimme, S. Supramolecular Binding Thermodynamics by Dispersion-Corrected Density Functional Theory. *Chemistry - A European Journal* **18**, 9955–9964 (2012). URL http://doi.wiley.com/10.1002/chem.201200497.

[186] Hauser, A. W., Volk, A., Thaler, P. & Ernst, W. E. Atomic collisions in suprafluid helium-nanodroplets: timescales for metal-cluster formation derived from He-density functional theory. *Physical Chemistry Chemical Physics* **17**, 10805–10812 (2015). URL http://pubs.rsc.org/en/content/articlehtml/2015/cp/c5cp01110h.

[187] Gomez, L. F., Loginov, E., Sliter, R. & Vilesov, A. F. Sizes of large He droplets. *Journal of Chemical Physics* **135**, 154201 (2011).

[188] Farber, M., Manuel Uy, O. & Srivastava, R. Effusion-mass spectrometric determination of the heats of formation of the gaseous molecules V_4O_{10}, V_4O_8, VO_2, and VO. *The Journal of Chemical Physics* **56**, 5312–5315 (1972).

[189] Fursa, D. V. & Bray, I. Calculation of electron-helium scattering. *Physical Review A* **52**, 1279 (1995).

[190] Grimme, S., Bannwarth, C. & Shushkov, P. A Robust and Accurate Tight-Binding Quantum Chemical Method for Structures, Vibrational Frequencies, and Noncovalent Interactions of Large Molecular Systems Parametrized for All spd-Block Elements (Z= 1–86). *Journal of Chemical Theory and Computation* **13**, 1989–2009 (2017). URL http://pubs.acs.org/doi/10.1021/acs.jctc.7b00118.

[191] Mardirossian, N. & Head-Gordon, M. Exploring the limit of accuracy for density functionals based on the generalized gradient approximation: Local, global hybrid, and range-separated hybrid functionals with and without dispersion corrections. *The Journal of Chemical Physics* **140**, 18A527 (2014). URL `http://scitation.aip.org/content/aip/journal/jcp/140/18/10.1063/1.4868117`.

[192] Shao et al., Y. Advances in molecular quantum chemistry contained in the Q-Chem 4 program package. *Molecular Physics* **113**, 184–215 (2015). URL `http://www.tandfonline.com/doi/abs/10.1080/00268976.2014.952696`.

[193] Weigend, F. & Ahlrichs, R. Balanced basis sets of split valence, triple zeta valence and quadruple zeta valence quality for h to rn: Design and assessment of accuracy. *Physical Chemistry Chemical Physics* **7**, 3297–3305 (2005). URL `http://dx.doi.org/10.1039/B508541A`.

[194] Roy, L. E., Hay, P. J. & Martin, R. L. Revised basis sets for the lanl effective core potentials. *Journal of Chemical Theory and Computation* **4**, 1029–1031 (2008). URL `https://doi.org/10.1021/ct8000409`. PMID: 26636355.

[195] Giannozzi, P. *et al.* Quantum espresso: A modular and open-source software project for quantum simulations of materials. *Journal of Physics: Condensed Matter* **21**, 395502 (2009). URL `http://www.quantum-espresso.org`.

[196] Ketelaar, J. A. A. Crystal Structure and Shape of Colloidal Particles of Vanadium Pentoxide. *Nature* **137**, 316–316 (1936).

[197] Fierro, J. L. G. *Metal Oxides: Chemistry and Applications* (CRC press, 2005).

[198] Asmis, K. R. & Sauer, J. Mass-selective vibrational spectroscopy of vanadium oxide cluster ions. *Mass Spectrometry Reviews* **26**, 542–562 (2007).

[199] Asmis, K. R., Santambrogio, G., Brümmer, M. & Sauer, J. Polyhedral vanadium oxide cages: Infrared spectra of cluster anions and size-induced d electron localization. *Angewandte Chemie International Edition* **44**, 3122–3125 (2005).

[200] Guimond, S. *et al.* Vanadium oxide surfaces and supported vanadium oxide nanoparticles. *Topics in Catalysis* **38**, 117–125 (2006).

[201] Herwig, C. & Limberg, C. V4o10: Spectroscopic fingerprint of a well-defined, molecular metaloxo aggregate. *Inorganic Chemistry* **47**, 2937–2939 (2008).

[202] Busca, G., Lietti, L., Ramis, G. & Berti, F. Chemical and mechanistic aspects of the selective catalytic reduction of NO_x by ammonia over oxide catalysts: a review. *Applied Catalysis B: Environmental* **18**, 1–36 (1998).

[203] Centi, G. Nature of active layer in vanadium oxide supported on titanium oxide and control of its reactivity in the selective oxidation and ammoxidation of alkylaromatics. *Applied Catalysis A: General* **147**, 267–298 (1996).

[204] Deo, G. & Wachs, I. E. Reactivity of supported vanadium oxide catalysts: The partial oxidation of methanol. *Journal of Catalysis* **146**, 323–334 (1994).

[205] Sun, Q. *et al.* In situ Raman spectroscopy during the partial oxidation of methane to formaldehyde over supported vanadium oxide catalysts. *Journal of Catalysis* **165**, 91–101 (1997).

[206] Resini, C., Montanari, T., Busca, G., Jehng, J.-M. & Wachs, I. E. Comparison of alcohol and alkane oxidative dehydrogenation reactions over supported vanadium oxide catalysts: in situ infrared, Raman and UV–vis spectroscopic studies of surface alkoxide intermediates and of their surface chemistry. *Catalysis Today* **99**, 105–114 (2005).

[207] Barker, J., Saidi, M. & Swoyer, J. Performance evaluation of the electroactive material, γ LiV_2O_5, made by a carbothermal reduction method. *Journal of The Electrochemical Society* **150**, A1267–A1272 (2003).

[208] Molek, K., Reed, Z., Ricks, A. & Duncan, M. Photodissociation of chromium oxide cluster cations. *The Journal of Physical Chemistry A* **111**, 8080–8089 (2007).

[209] Lasserus, M. *et al.* Vanadium (v) oxide clusters synthesized by sublimation from bulk at fully inert conditions. *Chemical Science* (2019).

[210] Boatwright, A. *et al.* Helium droplets: a new route to nanoparticles. *Faraday Discussions* **162**, 113–124 (2013).

[211] Gomez, L. F., Loginov, E., Sliter, R. & Vilesov, A. F. Sizes of large he droplets. *The Journal of Chemical Physics* **135**, 154201 (2011).

[212] Bartelt, A., Close, J., Federmann, F., Quaas, N. & Toennies, J. Cold metal clusters: Helium droplets as a nanoscale cryostat. *Physical Review Letters* **77**, 3525 (1996).

[213] Su, D. S., Hävecker, M., Willinger, M. G. & Schlögl, R. Chemical and electron beam reduction of vanadium oxides monitored by EELS and NEXAFS. In *Microscopy & Microanalysis 2001* (2001).

[214] Volk, A. *et al.* Thermal instabilities and Rayleigh breakup of ultrathin silver nanowires grown in helium nanodroplets. *Physical Chemistry Chemical Physics* **17**, 24570–24575 (2015).

[215] Hébert, C. *et al.* Oxygen k-edge in vanadium oxides: simulations and experiments. *The European Physical Journal B-Condensed Matter and Complex Systems* **28**, 407–414 (2002).

[216] Li, J., Gauntt, B., Kulik, J. & Dickey, E. Stoichiometry of nanocrystalline VO_x thin films determined by electron energy loss spectroscopy. *Microscopy and Microanalysis* **15**, 1004–1005 (2009).

[217] Lin, X., Wang, Y., Dravid, V. P., Michalakos, P. & Kung, M. Valence states and hybridization in vanadium oxide systems investigated by transmission electron-energy-loss spectroscopy. *Physical Review B* **47**, 3477 (1993).

[218] Li, Y., Kuang, J.-L., Lu, Y. & Cao, W.-B. Facile synthesis, characterization of flower-like vanadium pentoxide powders and their photocatalytic behavior. *Acta Metallurgica Sinica (English Letters)* **30**, 1017–1026 (2017).

[219] Momma, K. & Izumi, F. Vesta 3 for three-dimensional visualization of crystal, volumetric and morphology data. *Journal of Applied Crystallography* **44**, 1272–1276 (2011).

[220] Ramana, C., Hussain, O., Naidu, B. S. & Reddy, P. Spectroscopic characterization of electron-beam evaporated V_2O_5 thin films. *Thin Solid Films* **305**, 219–226 (1997).

[221] Zhai, H.-J., Döbler, J., Sauer, J. & Wang, L.-S. Probing the electronic structure of early transition-metal oxide clusters: Polyhedral cages of (V_2O_5) n-(n= 2- 4) and (M_2O_5)) 2-(M= Nb, Ta). *Journal of the American Chemical Society* **129**, 13270–13276 (2007).